Nanophotonic Application to Biomedical Devices

Thesis by

Haeri Park Hanania

In Partial Fulfillment of the Requirements for
the Degree of
Doctor of Philosophy in Medical Engineering

CALIFORNIA INSTITUTE OF TECHNOLOGY
Pasadena, California

2022
(Defended February 7, 2022)

Haeri Park Hanania
ORCID: 0000-0002-2206-5732

ACKNOWLEDGEMENTS

I would like to thank my advisors Dr. Hyuck Choo and Dr. Morteza Gharib for their support throughout my PhD years. I remember my first visit to Caltech for an interview with Dr. Choo. Afterwards, he kindly invited me to a dinner for medical engineering students and I got to spend time with my cohorts-to-be (Jinglin, Colin, Di, and Alexandro), even though I would not know until a few weeks later whether I would be able to join them. I probably felt more excited and nervous than I had in years. My PhD years were not always smooth sailing: indeed, they were filled with countless moments of frustration and disappointment that came from the disparity between what I wanted to achieve and what I had accomplished. Dr. Choo understood my struggles and would gladly reserve his time for me whenever I needed help. I will always appreciate having had his support and the opportunity to be a part of exciting research projects.

In the last few years of my PhD, I faced a new challenge as I started a family with my husband, Richard, and brought my son Theodore into the world. I found that becoming a mother was the hardest thing I had ever done. Nevertheless, my family has given me a new meaning in life, one that cannot be compared to anything else. Theodore taught us what it is like to be immensely loved as parents. Watching him grow, learn, and play with his daddy has been the greatest gift. Now that we are welcoming our daughter, Elodie, in March, we look forward to years of much more joy and gratitude. Thank you, Richard, Theodore, and Elodie, for providing me endless happiness.

I would also like to thank Dr. Jeong Oen Lee, Dr. Daejong Yang, Dr. Shailabh Kumar, Dr. Blaise Ndjamen, and Dr. Radwanul Siddique for their support and advice in the lab. I would like to thank my lab mates Hyunjun Cho and Vinayak Narasimhan for their friendship and support through the good and hard times.

Finally, I would like to thank my family in Korea, my mother, father, and brother, for their support throughout my life. My parents have sacrificed everything for their children and provided us with endless love. My mother always could see what I needed every step of the way, and I could not ask for more than what she has provided. I can always depend on her and feel secure, knowing she is always there for me. I would not be here without her guidance and support.

ABSTRACT

Nanophotonics is the study of interactions between nanoscale structures and light. It has greatly expanded the fields of application over the past decades, taking advantage of the advancement in MEMS technology. The most common nanophotonic structures consist of either dielectrics, metals, or both. When a nanophotonic structure contains metals, it is considered as a plasmonic structure. Plasmonics is a field of light-metal interactions. Due to the negative permittivity of metals, the electromagnetic energy of light is focused at the metal-dielectric interface and creates plasmons-a collective motion of electrons in the conduction band of metals. By shaping metals into different structures to achieve a desired performance, plasmonics have been successfully applied to many fields including photovoltaics, spectroscopy, and biomedical devices.

This thesis provides 3 different applications of biomedical devices in which nanophotonics-articularly plasmonics-was applied. Chapter 1 discusses the application of nanophotonics to molecular sensing. In this chapter, an open-top, tapered waveguide that serves as a 3-dimensional plasmon cavity is demonstrated and achieves a near or single molecular detection. Chapter 2 discusses the application of nanophotonics to an implantable intraocular pressure sensor. In this chapter, an array of gold nanodots are introduced on a flexible membrane to optimize the performance of the sensor. Chapter 3 discusses the application of nanophotonics to angle-and-polarization independent pressure or strain sensing, which reduces the need for precise alignment or a trained technician, and therefore can be easily applied to moving subjects in diverse environments. Inspired by the geometry and optical principles of butterfly corneas, an array of gold paraboloids is designed to support a surface plasmon resonance that is angle-and-polarization independent. This array is integrated onto a hermetically sealed cavity with a flexible membrane and enables angle-and-polarization independent pressure/strain sensing.

PUBLISHED CONTENT AND CONTRIBUTIONS

Journal articles:

Kumar, S.†, **Park, H.**†, Cho, H. et al., Overcoming evanescent field decay using 3D-tapered nanocavities for on-chip targeted molecular analysis. Nature Communications 11, 2930 (2020). DOI: 10.1038/s41467-020-16813-5

H.H participated in the numerical and theoretical optimization of the device, prepared the data, and wrote the manuscript.

Lee, J., **Park, H.**, Du, J. et al., A microscale optical implant for continuous in vivo monitoring of intraocular pressure. Microsystems & Nanoengineering 3, 17057 (2017). DOI: 10.1038/micronano.2017.57

H.H participated in the numerical and theoretical optimization of the device and prepared the data.

Han, S. J. †, **Park, H.** †, Lee, J. O., & Choo, H. Effect of optical aberrations on intraocular pressure measurements using a microscale optical implant in ex vivo rabbit eyes. Journal of Biomedical Optics, 23(4), 047002 (2018). DOI: 10.1117/1.JBO.23.4.04700

H.H participated in the conception of the project, building the aberration measurement setup, performing aberration experiments, prepared the data, and wrote the manuscript.

†These authors contributed equally.

Conferences:

Lee, J. O., **Park, H.**, Chen, O., Balakrishna, A., Du, J., Sretavan, D. W., & Choo, H. (2016, January). Achieving clinically viable 12-CM readout distance from micromachined implantable intraocular pressure sensor using a standard clinical slit lamp. In *2016 IEEE 29th International Conference on Micro Electro sMechanical Systems (MEMS)* (pp. 210-213). IEEE.

Lee, J. O., Du, J., **Park, H.**, Sencan, M., Kudisch, M., Sretavan, D., & Choo, H. (2016). In vivo intraocular pressure measurements using a miniaturized nano-photonic sensor implant. *Investigative Ophthalmology & Visual Science*, *57*(12), 6462-6462.

Patents:

H. Choo, A. Balakrishna, O. Chen, K. H. Kim, J. Lee, V. Narasimhan and **H. Park**. "System and method for measuring intraocular pressure." App. No.: US20170164831A1, Filed: November 29, (2016).

TABLE OF CONTENTS

LIST OF ILLUSTRATIONS AND/OR TABLES

Number *Page*

Chapter 1

NANOPHOTONIC APPLICATION TO TARGETED MOLECULAR ANALYSIS

This chapter was adapted from:

Kumar, S.†, Park, H.†, Cho, H. et al. Overcoming evanescent field decay using 3D-tapered nanocavities for on-chip targeted molecular analysis. Nature Communications 11, 2930 (2020). DOI: 10.1038/s41467-020-16813-5

†These authors contributed equally.

1.1 Introduction to plasmonic fluorescence enhancement

A molecule may absorb an incident light source and move to a higher vibrational state, and then may spontaneously move to a lower vibrational energy level while releasing the difference in the energy levels (photons) (Figure 1.1.1) [1]. Fluorophores are organic molecules that are specifically designed to perform absorption and emission of light at a variety of wavelengths. Enhancement of fluorescence can be achieved by coupling the emission of light to a surrounding electromagnetic environment such as resonant cavities [2,3 Halas], photonic crystals [4,5], and plasmonic nanostructures [6,7]. Plasmonic fluorescence enhancement can be achieved by enhancing (1) near field enhancement close to metal-dielectric interface [8], (2) radiative decay rate [9], and (3) the coupling of near field scattering to far field scattering [10,11].

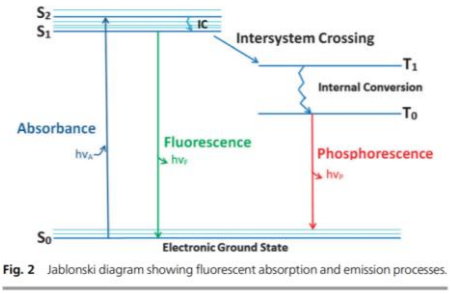

Figure 1.1.1 Diagram of fluorescent absorption and emission processes [1]. Reprinted with permission from the Royal Society of Chemistry.

1.2 Challenges for plasmonic fluorescence enhancement

While enhancement of optical signals such as fluorescence using plasmonic nanostructures promised breakthroughs in areas such as single molecule fluorescence-driven DNA sequencing [12,13], rapid disease detection [14-16], as well as observation of biological reactions [17,18], their widespread application towards bioassays has remained lacking. One major reason for the lack of applicability of plasmonic fluorescence enhancement remains the wide variability in enhancement efficiency for molecular assays. Fluorescence enhancement obtained from plasmonic nanostructures is intrinsically dependent on both the efficiency of electromagnetic (EM) field confinement at the plasmonic hotspot as well as the distance between the optical emitter (fluorophore) and the plasmonic hotspot [10,19–22]. These fluorophores are typically attached to biorecognition elements such as antibodies or nucleic acid aptamers that recognize and specifically bind to other target molecules. Therefore, the position or distance of light-emitting fluorophores with respect to a plasmonic hotspot is dependent on size as well as number of the molecules within the biomolecular complex and can drastically alter the plasmonic enhancement of the emitted signal due to changes in the radiative and non-radiative field components [21-24]. Inconsistent or weak enhancement of signal due to these variations limits both the accuracy and efficiency of molecular binding analysis on chip. While several reports have discussed novel nanoscale geometries that improve the confinement of EM fields leading to strong fluorescence enhancements [8,25–27], engineering a hotspot that resolves the distance challenge between the emitter and the nanostructure surface has remained elusive. Powerful fluorescence enhancement within a nanostructure independent of

variation in molecule size and position can be expected to rely on several important factors: (a) strong confinement of electromagnetic field, (b) powerful coupling of the emitter to the field for enhancement of emission, and (c) a hotspot geometry, which generates uniform electromagnetic field distribution. At the same time, the hotspot geometry needs to be large enough for commonly used protein–protein binding assays (i.e., larger than antibodies, ~15 nm). Metal–insulator–metal (MIM) structures utilizing surface-plasmon-polariton (SPP) propagation have been known to enable efficient confinement of EM energy [28–31]. Specifically, waveguides with a 3D taper that rely on adiabatic compression of the SPP mode inside the MIM gap have been shown to provide extreme volumetric nanoscale confinement of EM fields [32–36]. While extremely promising for energy confinement and transfer, the potential of 3D-tapered designs for coupling with fluorescent emitters and bioassays had remained unrealized primarily due to closed monolithic structures, which prevented molecular integration with these devices. Furthermore, as electromagnetic field intensity on a plasmonic surface is maximum at the metal-dielectric interface, close packing of multiple metal–dielectric interfaces such as in very thin MIM gaps, can result in integration of these multiple field profiles within the gap creating a more homogeneous field distribution.

1.3 Design and principle of 3D tapered nanocavity for plasmonic fluorescence enhancement

The 3D-tapered gap plasmon nanocavities were fabricated in gold- and silica-coated silicon substrates as shown in Figures 1.3.1a, b. (see 1.6.1 Device fabrication). The sidewalls that are ion-milled in the gold layer and the exposed top surface of the SiO2 base, together form a fluidic MIM nanocavity that tapers vertically and laterally into a nanoscale tip (Figure 1.3.1c). The hydrophilic SiO2 base attracts fluid into the 3D-tapered nanocavity channel, promotes efficient molecular delivery, and provides surface site-specific molecular binding. Repeating the fabrication process, we also produced 3D-tapered gap plasmon nanocavity arrays with 20-nm wide and 500-nm long tips integrated onto a larger fluidic channel as shown in the scanning electron microscope images of Figures 1.3.1e–g. The design of the device was optimized for (a) efficient coupling of excitation light into the device body, (b) optimal transversal confinement of EM field- high and uniform $|E|^2$ of the guided mode- through the taper, and (c) efficient longitudinal confinement of EM field at the tip. We chose 750 nm as the target wavelength for fluorophore excitation.

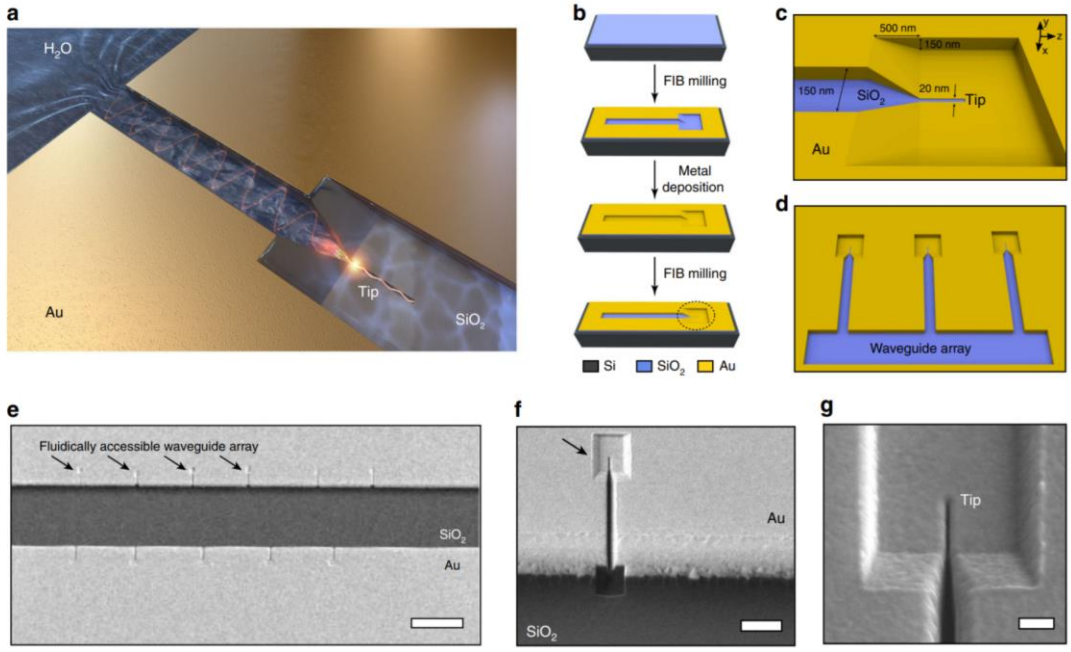

Figure 1.3.1 Fabrication of 3D-tapered gap plasmon nanocavities. (a) Overview image of the device with plasmonic wave propagation and confinement at the end of three-dimensionally tapered tip. Open cavity allows fluidic delivery and surface functionalization enabling molecular capture. (b) Device fabrication using a silicon wafer with 1 μm thick thermally grown silicon dioxide, gold deposition, and FIB milling. (c) Zoomed-in view of the 3D-tapered nanocavity tip. (d) Schematic showing an array of 3D-tapered nanocavities with a hydrophilic silica base. (e) SEM image showing fabricated arrays of 3D-tapered nanocavities with hydrophilic silica base. Scale bar is 25 μm. (f) A single 3D-tapered nanocavity. Scale bar is 2 μm. g Sharp 3D-tapered nanocavity tip. Scale bar is 200 nm. Reprinted with permission from [61].

For design optimization, the device was divided into three parts: the body, the taper, and the tip. Finite-difference time-domain (FDTD) simulations were utilized to accomplish efficient confinement of the fundamental anti-symmetric (AS) SPP mode at the tip of the 3D-tapered gap plasmon nanocavity. In the new design that allows hotspot access to fluids, a pair of Au walls separated horizontally on the SiO2 substrate support the AS mode whose electric field is aligned parallel to the substrate (Figure 1.3.2a, b). First, the body width (w_{body}), height (h_{body}), and length (l_{body}) were optimized for efficient coupling of excitation light to the taper.

Throughout the optimization processes, the tip width (w_{tip}) and height (h_{tip}) were set to 20 nm and 50 nm, respectively. w_{tip}= 20 nm enabled controlled assembly of 1D-array antibodies (~15 nm diameter). h_{tip} was determined by adjusting the thickness of the evaporated Au layer during fabrication, and it was twice the skin depth of Au (~25 nm) or 50 nm.

A higher contrast between the effective refractive index inside the channel (n_{eff}) and the refractive index of the substrate (n_{SiO2} = 1.45) results in a higher tail-end coupling efficiency; the smaller the w_{body} and h_{body} are, the larger the n_{eff} and better the tail-end coupling of excitation light into the body (Figure 1.3.2c). However, the smaller cross-sectional dimensions also reduced the propagation length L_m (Equation 1.3.1) of the guided AS mode (Figure 1.3.2d), which led to inefficient coupling of the tail-end excitation to the taper as the guided mode experienced significant loss throughout propagation inside the body. The body with w_{body} ~ 150 nm and $h_{body} \geq$ 150 nm showed the best coupling efficiency to the taper for a l_{body} = 3 μm device (Figure 1.3.2e). Therefore, both the w_{body} and h_{body} were set to 150 nm, which resulted in n_{eff} = 1.67 (>n_{SiO2} = 1.45), L_m = 3 μm, and the 1.12% tail-end coupling efficiency to the taper. l_{body} was set to 3 μm, which is similar to the propagation length of the guided mode, to efficiently couple the tail-end excitation light into the taper. In addition to tail-end excitation, the open-top channel of this device enables excitation of the guided mode throughout the body, which will be discussed in the following paragraph.

$$L_m = \frac{1}{2Im(\boldsymbol{k}_m)} \qquad \text{Equation 1.3.1}$$

Next, the taper angle of the 3D-tapered nanocavity was optimized for efficient coupling of guided AS SPP mode to the tip as well as uniform and high electric-field ($|\mathbf{E}|^2$) enhancement for optimized emission response from molecules. The coupling efficiency (P_{tip}/P_{body}) was calculated based on the power at the cross-sections right before (P_{body}) and after (P_{tip}) the taper. $|\mathbf{E}|^2$ was calculated at the narrower end of the taper. Figures 1.3.3a, b show the $|\mathbf{E}|^2$ and the coupling efficiency of devices with varying tip lengths (l_{tip} = ∞, 500 nm, 20 nm) for taper angles (α) ranging from 10° to 70° at the 750-nm wavelength. Both the $|\mathbf{E}|^2$ and the coupling efficiency showed the best performance within the range of $20° \leq \alpha \leq 30°$ for the various tip lengths. Experimental results showed the same trend (Figure 1.3.4). For small α, the taper length increases, and this results in greater absorption [32,33,37]. When

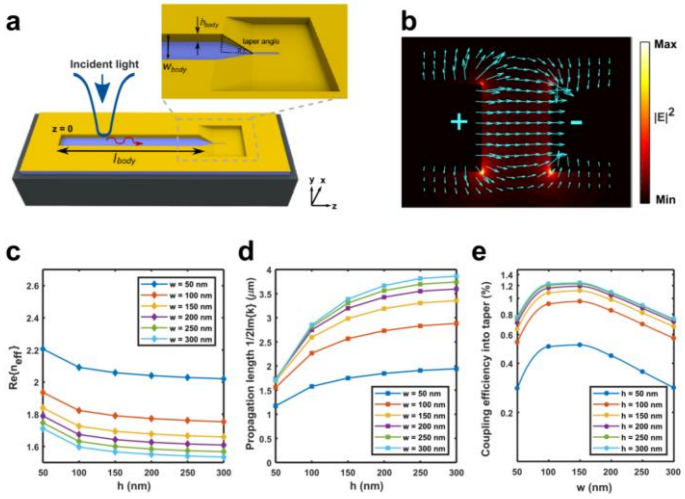

Figure 1.3.2 Optimization of the body width and height. (a) Schematic showing 3D-tapered nanocavity dimensions represented by symbols used in manuscript. Length of the body is l_{body}, height is h_{body}, and the taper angle is represented as α. (b) Electric-field profile of the fundamental anti-symmetric (AS) mode at the cross-section of the body. (c) Effective refractive index n_{eff} of the guided mode inside the body with varied w_{body} and h_{body}. As the w_{body} and h_{body} increase, n_{eff} decreases and the guided mode becomes less confined. (d) Propagation length L_m of the guided mode inside the body with varied w_{body} and h_{body}. As the w_{body} and h_{body} increase, the propagation length increases and provides more efficient coupling of guided modes into the taper. (e) Coupling efficiency to the taper with varied w_{body}, and h_{body} for a l_{body} = 3 μm device. Reprinted with permission from [61].

α becomes large, the abrupt angle in the taper geometry results in the severe scattering of guided modes due to mismatch between the wave vectors inside the taper and the tip [32,33,37]. In addition, small fluctuations in the $|\mathbf{E}|^2$ and coupling efficiency in the range of $10° \leq \alpha \leq 70°$ are observed as impedance matching condition fluctuates with α (Figures 1.3.3c-e); $Z_{body} = Z_{tip}$ at the peak locations observed in Figures 1.3.3a, b, where $Z_{body}(Z_{tip})$ is the impedance of the body (tip). Z_{body} was calculated based on Equation 1.3.2 [38]. Z_{tip} at each α was calculated by iteration of Equation 1.3.3 [39] for 100 segments (Z_n, $1 \leq n \leq 100$) along each taper length, where Z_n is the impedance of n-th segment calculated using Equation 1.3.2, Z(n)in is the input impedance of n segments, k_n is the complex propagation constant of the n-th segment, and l_n is the segment length.

$$Z = R - iX = \frac{V}{I} = \frac{\int E_x dx}{\int H_y dy} \qquad \text{Equation 1.3.2}$$

$$Z_{(n)in} = Z_n \frac{Z_{(n-1)in} - iZ_n \tanh(k_n l_n)}{Z_n - iZ_{(n-1)in} \tanh(k_n l_n)} \qquad \text{Equation 1.3.3}$$

Figure 1.3.3e shows the uniformity of the $|\mathbf{E}|^2$ enhancement in the range of $10° \leq \alpha \leq 70°$. The uniformity of the $|\mathbf{E}|^2$ enhancement was calculated based on a 2-D normalized $|\mathbf{E}|^2$ (setting 1 as the highest) profile at the cross-section of the tip. A smaller α showed better uniformity in the $|\mathbf{E}|^2$ enhancement, as a larger α increases scattering of guided modes [32,33,37]. The total transversal EM energy U_A and average transversal EM energy density $\bar{u}_A$ plotted in Figure 1.3.2b were calculated based on Equations 1.3.4, 1.3.5. The efficient transversal confinement of EM energy inside the nanocavity allows uniform $|\mathbf{E}|^2$ enhancement; Figure 1.3.2b shows $U_{A\_body} \sim U_{A\_tip}$, which results in an order of magnitude greater $\bar{u}_A$ at the tip.

$$U_A = U_{E,A} + U_{H,A} = \int_A \frac{1}{2}\varepsilon_0 |E|^2 + \int_A \frac{1}{2}\mu_0 |H|^2 \qquad \text{Equation 1.3.4}$$

$$\bar{u}_A = U_A/(\text{cross} - \text{section of tip}) = (U_{E,A} + U_{H,A})/(\text{cross} - \text{section of tip})$$

Equation 1.3.5

Finally, the tip length (l_{tip}) was optimized for longitudinal confinement of light for detection of targeted number of molecules by controlling the size, location, and enhancement magnitude of the hotspots formed inside the tip. In the l_{tip} optimization, parameters were set to w_{body} = 150 nm, h_{body} = 150 nm, l_{body} = 3 μm, α = 20°. A device with an infinite l_{tip} shows a gradual decrease in $|\mathbf{E}|^2$ enhancement along the tip due to absorption along the sidewalls of the tip (Figures 1.3.5a, b). On the other hand, a device with a finite l_{tip} experiences power reflection at the end of the tip [35]. This leads to the formation of Fabry-Perot resonances of different number of peaks (m) along the longitudinal direction of the tip [40]. In this case, a properly chosen α could provide matching standing wave vectors inside the taper that could result in pronounced $|\mathbf{E}|^2$ enhancement of the resonances in the tip. In addition, a shorter l_{tip} produces intensity patterns with fewer periodic resonant peaks, which reduces the overall hotspot volume. When l_{tip} = 500 nm, the device exhibits greater $|\mathbf{E}|^2$ of the m = 4 Fabry-Perot resonance at $\alpha \sim 20°$ and $\alpha \sim 45°$ (Figures 1.3.5a, b). When the tip is shorter (l_{tip} = 20 nm), the device shows further increase in the $|\mathbf{E}|^2$ enhancement of the m = 1 Fabry-Perot resonance at $\alpha \sim 20°$ and $\alpha \sim 60°$. The overall $|\mathbf{E}|^2$ enhancement increases with a shorter l_{tip} due to reflection

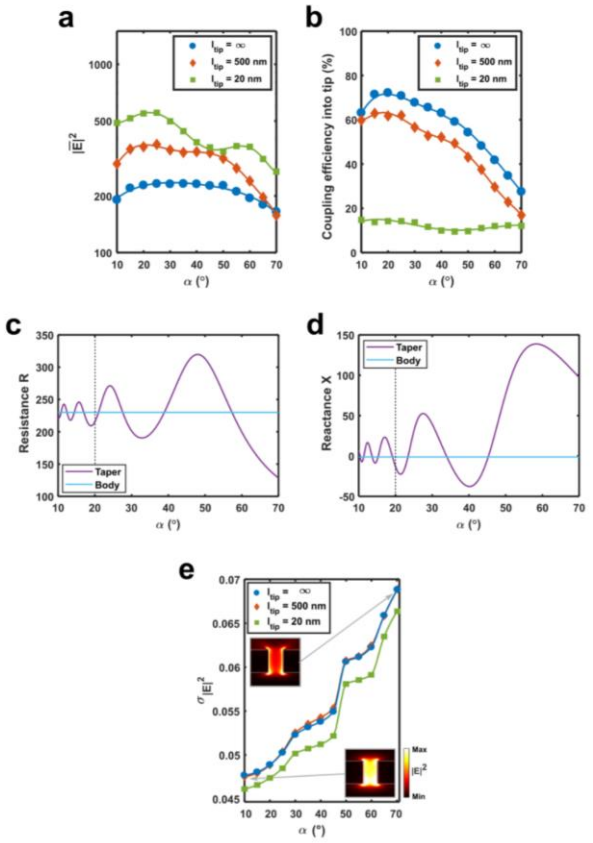

Figure 1.3.3 Optimization of the taper angle (a) Average $|\mathbf{E}|^2$ enhancement ($\overline{|\boldsymbol{E}|^2}$) at the tip with varied taper angle α. (b) Coupling efficiency from the body to the tip with varied taper angle α. Calculated (c) resistance and (d) reactance of the taper and body based on Supplementary Equations 2,3. Impedance matching between the taper and body happens at α ~ 20°. (e) Standard deviation of the normalized $|\mathbf{E}|^2$ enhancement distribution at the tip with varied taper angle α. Reprinted with permission from [61].

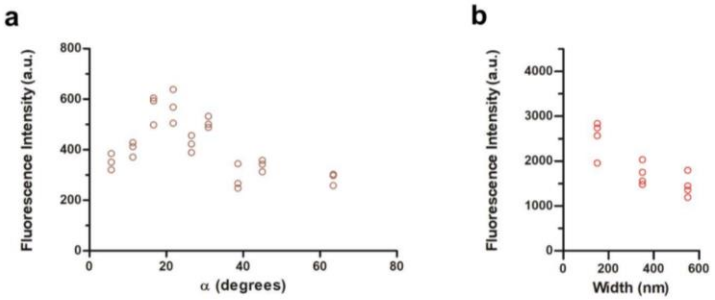

Figure 1.3.4 Experimental device optimization (a) Experimental results showing that the highest fluorescence intensity from the devices was obtained for taper angle (α) close to 20°, with the body width maintained at 150 nm, tip length as 500 nm and width as 20 nm. (b) Experimental results showing that devices with body width around 150 nm had higher fluorescence emission as compared to devices with wider body widths. Device taper angle was maintained at 20° for these tests. The experimental results support the parameters indicated by simulations. Reprinted with permission from [61].

from the tip end, which increases the average volumetric EM energy density $\bar{u}_V$ inside the tip (Figure 1.3.5c). $\bar{u}_V$ was calculated based on Equations 1.3.6, 1.3.7.

$$U_V = U_{E,V} + U_{H,V} = \int_V \frac{1}{2}\varepsilon_0|E|^2 + \int_V \frac{1}{2}\mu_0|H|^2 \qquad \text{Equation 1.3.6}$$

$$\bar{u}_V = U_V/(\text{volume of tip}) = (U_{E,V} + U_{H,V})/(\text{volume of tip}) \qquad \text{Equation 1.3.7}$$

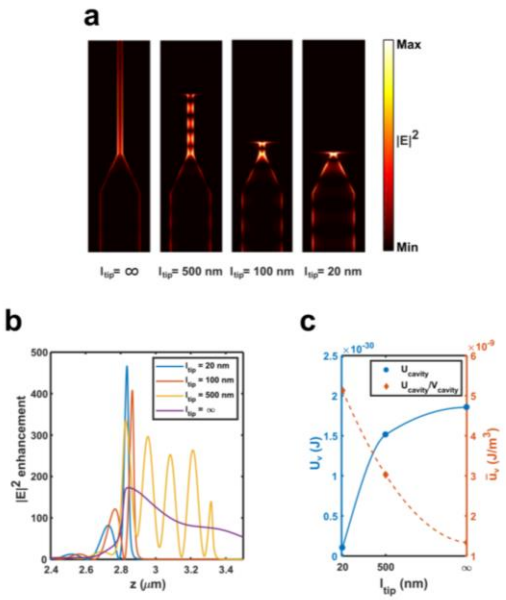

Figure 1.3.5 Optimization of the tip length (a) Electric field distribution of the guided mode with varied tip lengths (Infinite, 500 nm, 100 nm, 20 nm, from left to right). (b) Comparison between the $|E|^2$ enhancement profiles of different tip lengths. A shorter tip provides higher enhancement in a more confined area. (c) Comparison between the stored energy U and average energy density $\bar{u}$ in tips of different lengths. U and $\bar{u}$ were calculated based on Equation 1.3.6 and 1.3.7, respectively. A shorter tip provides a higher density of the stored energy inside the tip, whereas the total amount of stored energy decreases due to increased loss. Reprinted with permission from [61].

Figure 1.3.6a shows the profiles of EM energy density u at the cross-sections of the body (top) and tip (bottom) at $\alpha = 20°$. The total transversal EM energy stored inside the body (U_{A_body}) is efficiently confined inside the tip with minimal loss ($U_{A\_body} \sim U_{A\_tip}$), which significantly increases the average transversal EM energy density u_A at the tip (Figure 1.3.6b). The 3D-tapered gap plasmon nanocavity showed greater confinement of EM energy (greater u_A at the tip) than the 2D-tapered nanocavity and the tip-only structure (MIM structure without a taper) of the same tip size due to a larger cross-sectional area of the body being capable of storing greater U_{A_body} (see 1.6.2 Simulations). This extreme confinement of EM energy through the 3D taper suppresses evanescent-field type decay inside the 20×50 nm^2 tip (MIM gap), which is generally observed in high-$|E|^2$ plasmonic structures

such as a bowtie nanoantenna [8,41] or tip-only structures (MIM waveguides without a taper) [42] (Figures 1.3.6c, d and 1.6.2 Simulations). The optimized 3D taper achieved four times greater u_A and 40× improvement in uniformity $\sigma_{|E|2}$ than a bowtie nanoantenna of the same gap size (Figure 1.3.6e). All of the gap plasmon structures studied in the FDTD simulations (3D-, 2D-tapered nanocavities, and the tip-only structure) showed a trend that a greater u_A enabled a more uniform hotspot (a smaller $\sigma_{|E|2}$) and greater average $|E|^2$ ($\overline{|\boldsymbol{E}|^2}$). As a result, the optimized 3D-tapered nanocavity provided a large $\overline{|\boldsymbol{E}|^2}$= 230), uniform ($\sigma_{|E|2}$ = 0.05) $|E|^2$ profile at the tip along with an 11% net coupling efficiency. Experimental analysis of the taper angle and body width also matched the trend predicted by simulations, as maximal emission output was obtained from devices with taper angle α~20° and w_{body} = 150 nm. The volume and $|E|^2$ profile of the hotspot can be further optimized for capture of targeted number of molecules by varying l_{tip}. A shorter l_{tip} allows the coupled EM energy to be more densely packed longitudinally inside the tip, which results in greater $|E|^2$ within a smaller hotspot volume. A 20-nm long tip provided $\overline{|\boldsymbol{E}|^2}$ magnitude of 550 within a 20 × 50 × 5 nm^3 hotspot (Figures 1.3.6f, g). Based on the simulations, experimental results and considerations, devices were fabricated with the aforementioned dimensions (as shown in Figure 1.3.1) and fluorescence enhancement was studied.

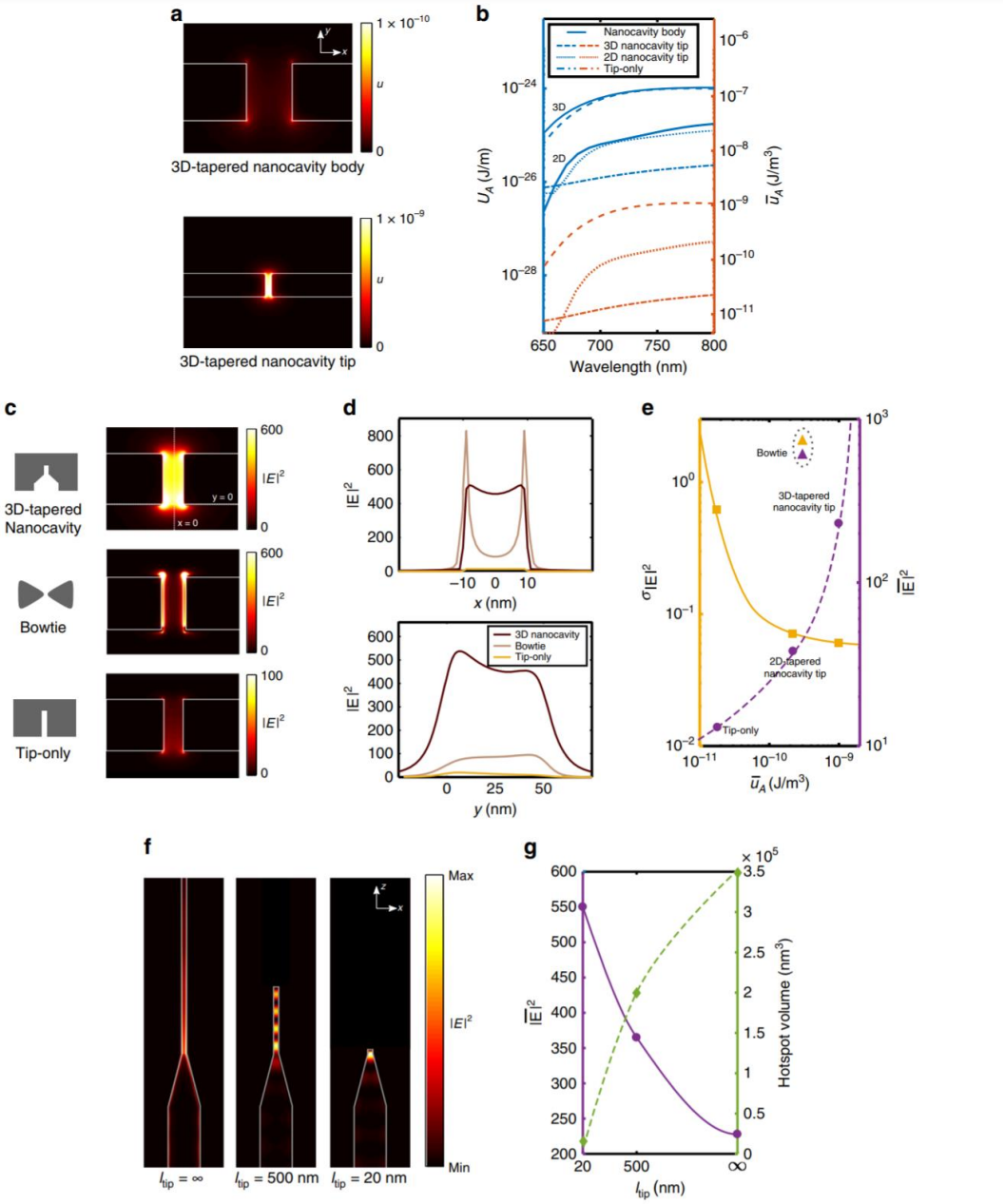

Figure 1.3.6 Design optimization of the 3D-tapered nanocavity using FDTD simulation. (a) Comparison between the cross-sectional views of the EM energy density profiles in the body (top) just before the 3D-taper (α = 20°) and at the tip (bottom). (b) The total transversal EM energy UA and average transversal EM energy density uA of the body and tip of the 3D- and 2D-tapered nanocavities and a tip-only structure. (c) Cross-sectional view of the $|E|^2$ profiles of the 3D-tapered nanocavity (top), a bow tie (middle), and a tip-only structure (bottom) of the same gap size (20 nm ×

50 nm). (d) $|E|^2$ inside the gaps of the structures at y = 0 (top) and x = 0 (bottom). (e) Hotspot uniformity $\sigma_{|E|2}$ and average $|E|^2$ at cross-sectional areas of the 3D- and 2D-tapered nanocavities, a tip-only structure (circle), and a bowtie (triangle). (f) Top view of the $|E|^2$ profiles in the devices with l_{tip} = 20 nm, 500 nm, and ∞. (g) $|E|^2$ and hotspot volume at the tips of the devices with varied l_{tip}. Reprinted with permission from [61].

1.4 Demonstration of 3D tapered nanocavity at single molecular resolution

We experimentally tested coupling of incident light into the nanocavity and gap plasmon-mediated volumetric confinement at the tips using surface-linked molecular layers and fluorescent labels. A molecular monolayer of biotin was assembled along the exposed silica surface of the 3D-tapered nanocavity, using silane-polyethylene glycol-biotin (SPB) as the reagent to form silane–silica covalent linkages (Figure 1.4.1a). Streptavidin linked with Alexa Fluor 750 (S-AF 750) was then used as a fluorescent label for detection of biotin in the tips, taking advantage of the well-known strong and highly-specific molecular interaction between biotin and streptavidin [43,44]. This two-step binding reaction allows the formation of a monolayer of fluorescently-tagged streptavidin on the silica surface along the length of the 3D-tapered nanocavity. We observed the capture of diffusing streptavidin molecules at high concentrations (1 μM) and resultant enhancement in fluorescence once a molecule binds to the tip region (Figures 1.4.1b, c).

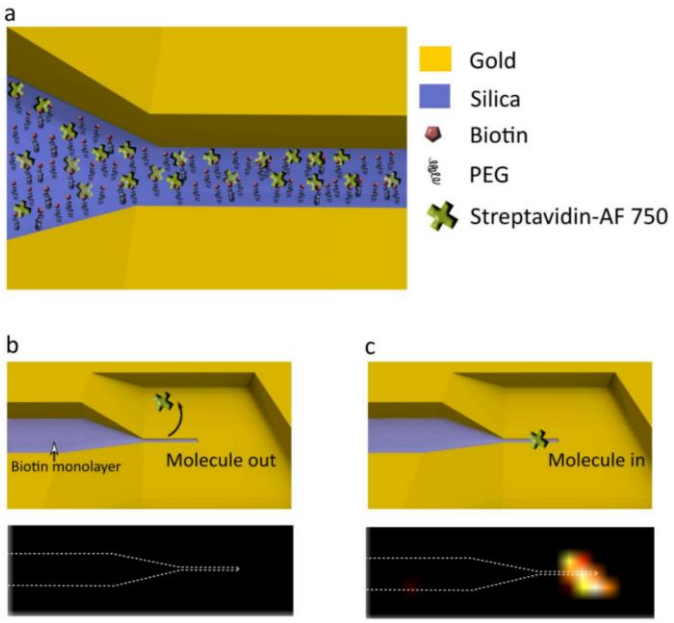

Figure 1.4.1 Molecular functionalization and imaging. (a) Schematic showing monolayer of PEG-biotin covering the base of the 3D-tapered nanocavity. (b) Fluorescence signal when streptavidin molecules are in solution but not at the tip. (c) Signal when a molecule binds at the tip region. Reprinted with permission from [61].

Detection of molecules diffusing in solution at micromolar concentrations has been an important target for biological tracking and has been demonstrated using nanostructures with zeptoliter detection volumes [25]. However, these detection methods lacked molecular specificity commonly required for bioassays. The silica base of our device serves as a targeted functionalization region inside the gap plasmon nanocavity, allowing specific capture of molecules diffusing in solution and differentiating them from the background through enhanced fluorescence signal. After molecular binding, chips were washed to remove unbound molecules and interrogated using tail-end and full illumination modes (Figures 1.4.2a, b). The tail-end illumination mode involves illumination of the back-end of the 3D-tapered nanocavity, whereas full illumination mode allows the complete device to be placed under illumination.

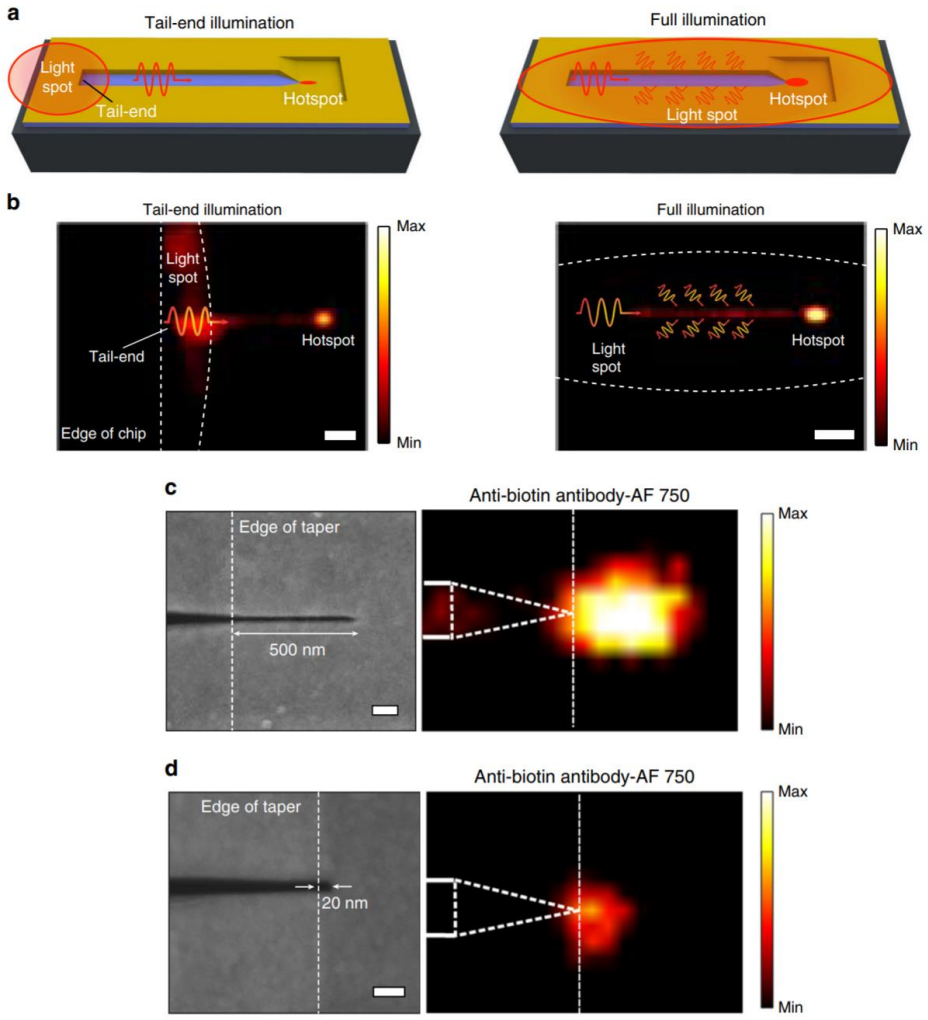

Figure 1.4.2 Molecular fluorescence enhancement and single molecule capture. (a) Illustration and (b) fluorescence images of streptavidin capture inside the nanocavities using tail-end (left) as well as full (right) illumination modes. Hotspot is visible at the end of taper within the 20 nm-wide tip. Scale bars are 1 μm. (c) SEM image (left) of a 3D-tapered nanocavity with tip length 500 nm and fluorescence image (right) obtained from the tip after antibody immobilization. 1D-array of antibodies is expected within the tip. Scale bar is 100 nm. (d) SEM image (left) of a 3D-tapered nanocavity tip with length 20 nm and fluorescence image (right) obtained from the short tip after antibody immobilization. Volumetric-limitation enables specific capture of single antibody at the end of the tip. Scale bar is 100 nm. Reprinted with permission from [61].

In Figure 1.4.3a, the coupling efficiency into the body (blue solid line) was calculated using FDTD by focusing a Gaussian light source and measuring power transmission through a cross-section at each longitudinal position of the body (z). Despite the reduced coupling efficiency into the body in the middle (0 μm < z < 3 μm), the amount of power coupled to the taper (Figure 1.4.3b) is doubled as z ~ 3 μm due to the dramatically reduced propagation loss (Figure 1.4.3a, red dashed line) as can be seen in Equation 1.4.1. The total coupling efficiency to the taper under full illumination is calculated to be ~15% (Figure 1.4.3b), which is ~10× higher than tail-end only excitation.

$$\begin{aligned}&\text{Coupling efficiency into taper}\\&= \text{Coupling efficiency into body} \times (1 - \text{Propagation loss inside body})\\&= \text{Coupling efficiency into body} \times (1 - e^{-2\alpha(3\mu m - z)})\end{aligned}$$

Equation 1.4.1

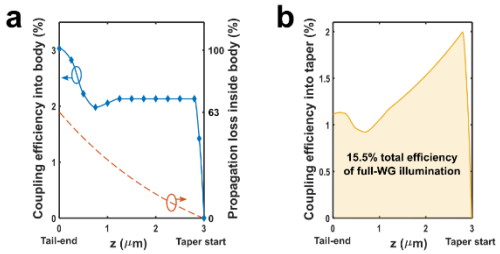

Figure 1.4.3 Coupling efficiency of full-waveguide illumination mode. (a) Coupling efficiency into the body (solid blue line) and propagation loss of the coupled light (dashed red line) at each longitudinal location (z) along the body length. (b) Coupling efficiency to the taper at each longitudinal location calculated based on Equation 1.4.1. Integrating the coupling efficiency along the body length, the total coupling efficiency under full-illumination is calculated to be 15.5%, which is ~10x greater than tail-end coupling efficiency shown in Figure 1.3.2e. Reprinted with permission from [61].

Excitation light from a near-infrared light-emitting diode light source (750 nm) was incident on the 3D-tapered nanocavities and a visible hotspot in the form of enhanced fluorescence was observed from the sub-20-nm tip region as a result of volumetric field confinement at the tips (Figure 1.4.2b). Due to improved coupling and light collection through the body of the device, about an order of magnitude improved intensity (~9×) at the tip was obtained using full illumination mode as

compared with tail-end illumination mode, which agrees with the calculation based on the FDTD simulations (~10×) (Figure 1.4.3). The role of the 3D-tapered nanocavity body towards fluorescence enhancement was further verified by fabricating dimensionally-varying structures. Nanocavities were fabricated with the full body, just 3D taper and tip, and stand-alone tips (l_{tip} = 500 nm for all three cases) and the mean fluorescence intensity observed at the tips was measured for all the cases (Figure 1.4.4). The trend for the nanocavities indicates that maximum intensity was obtained for the 3D-tapered nanocavity with full body. Observed fluorescence intensity sharply decreases when the whole device is reduced to just the 3D-taper and tip and decreases further for the stand-alone tip structures (Figure 1.4.4). These observations agree with the FDTD simulation results (Figure 1.4.5), where scattering at the backend or the sidewalls of the body incite SPP propagation towards the tip. Drastic decrease in light intensity for a taper-tip structure as well as standalone tip can be further attributed to loss in light collected from back scattering as well as edge scattering along the open edges of the body at the working wavelength.

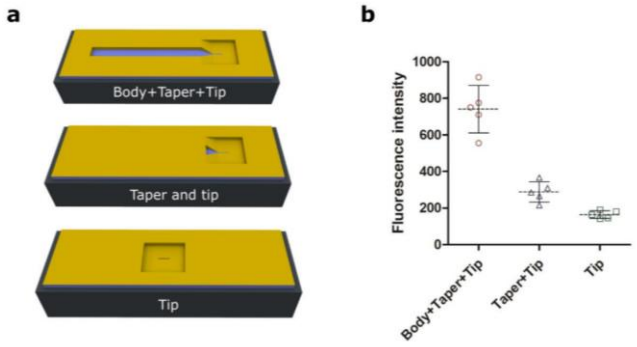

Figure 1.4.4 Experimental study on the effect of nanocavity structure on fluorescence. (a) 3D-tapered gap plasmon nanocavity, taper and tip, and tip only structures were fabricated with fragmented body length and (b) normalized fluorescence intensities at the tip was obtained for various structures demonstrating the effect of improved coupling through the device body. Data points, mean and s.d. for 5 samples at each condition are shown. Reprinted with permission from [61].,

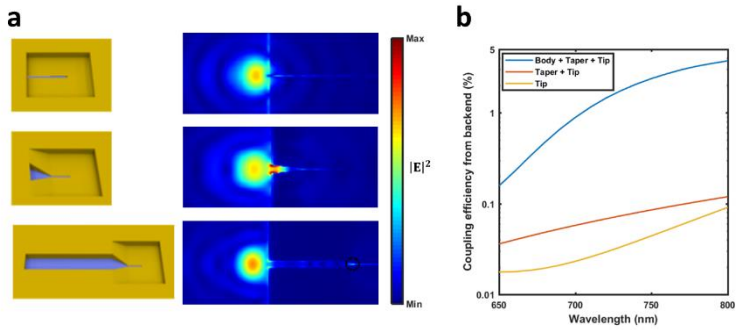

Figure 1.4.5 Coupling efficiency of tail-end illumination. (a) $|E|^2$ distribution at the tail-end of a tip (top), a taper (middle), and a body (bottom). A Gaussian beam centered at 750 nm with a spot size of 270-nm diameter (obtained using a 1.4-NA objective lens) was incident at the tail-end of each structure. A device with a body (bottom) shows a clear hotspot at the tip, which the upper two structures do not show. (b) Backend coupling efficiency of the three different combination structures in (a) plotted against wavelength (650-800 nm). Coupling efficiency is enhanced to more than an order of magnitude when a body is implemented to the device. Reprinted with permission from [61].

For subsequent molecular detection and analysis of plasmonic enhancement, full illumination mode was implemented. Limit of detection for biomolecules on the device was examined using two types of sensing experiments. First, detection of low concentration protein molecules in solution (10 pM–1 nM) was performed, testing device suitability for onchip diagnostics of rare disease-specific biomarkers (Figure 1.4.6). The detection limit in this case is governed by diffusive transport of molecules to the plasmonic hotspot and can be accelerated by improving molecule transport using convective flow, magnetic or dielectrophoretic trapping.

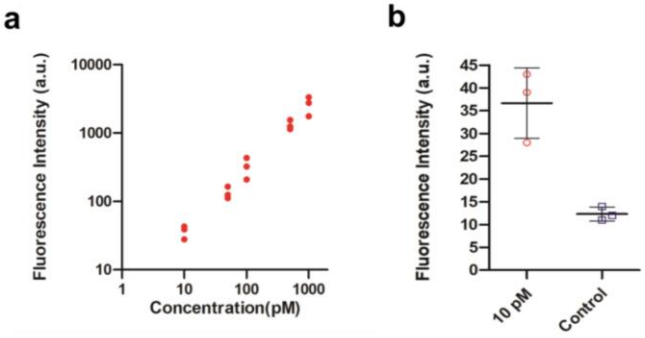

Figure 1.4.6 Detection of low concentration molecules on 3D-tapered waveguides (tip length 500 nm). (a) Log-log plot showing increase in signal with increase in concentration of added Streptavidin (10 pM – 1000 pM). (b) Fluorescence signal obtained from devices after testing with 10 pM streptavidin-AF 750. Negative control device had no biotin layer. Plot shows data points, mean, and s.d. for 3 devices at each condition. Reprinted with permission from [61].

Second, we examined the capture and detection of individual or small array of molecules at the hotspot, while high concentration of molecules was present in solution. User-controlled analysis of single or small array of molecules remains an important target for high-resolution analysis of protein function and behavior [45-47]. This is especially important in cases where ligands and biomolecules are physiologically present at higher (μM–mM) concentrations [48]. We control the number of molecules captured within the tips by altering the tip length. After formation of the biotin monolayer within the 3D-tapered nanocavities, we utilized an anti-biotin IgG primary antibody (tagged with DyLight 755 ~spectral response similar to AF-750) for performing fluorescence assays [49]. In order to compare the effect of tip length on capture of molecules, we performed these antibody binding experiments using devices with l_{tip} = 500 nm as well as l_{tip} = 20 nm (Figures 1.4.2c, d). The dimensions of a 3D-tapered nanocavity with a short tip (l_{tip} = 20 nm, w_{tip} = 20 nm) compared with those of an IgG antibody (length ~15–20 nm) [49,50] indicate that a single antibody should be specifically trapped within the tip region. We performed atomic force microscopy (AFM) which demonstrated uniform monolayer of PEG-biotin and antibodies on flat silica surfaces and indicated that only one antibody should specifically occupy the 20 nm × 20 nm tip (Figure 1.4.7). We obtained 1.5% variation between expected and measured fluorescence intensity for a single molecule at the

short tip, further indicating the presence of a single antibody at the short tip-end. The calculation was based on integrated fluorescence intensities from the tips and simulation-predicted $|E|^2$ profiles (Figure 1.3.6a) along with an assumption of packed molecular arrangement within the tips.

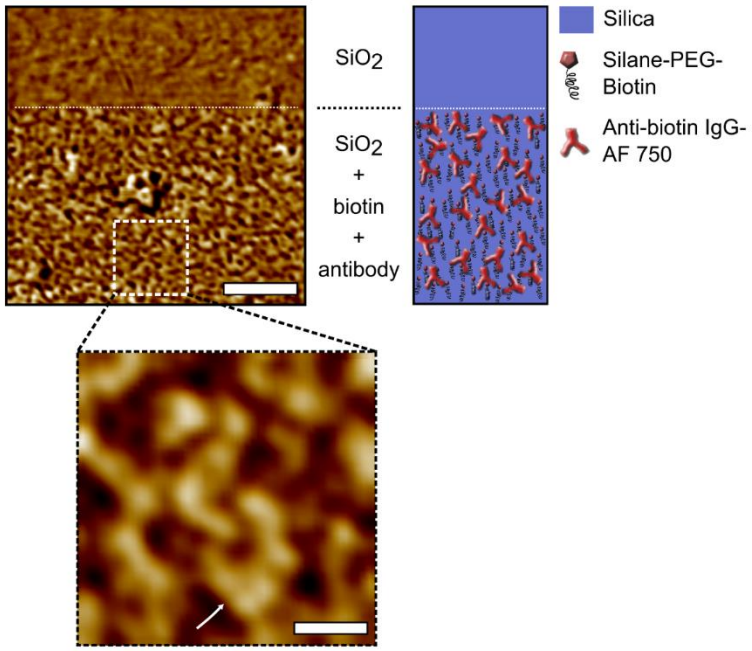

Figure 1.4.7 Tapping-mode images of the phase signal of the PEG-biotin conjugated antibody selectively coated on silica substrate showing the uniform monolayer arrangement in large scale. High resolution imaging as shown in an inset reveals the average size of the antibody of around 20 nm. The arrow highlights the typical three molecules with the tri-nodular flat orientation of the antibody. Scale bars, 200 nm (inset: 50 nm). Reprinted with permission from [61].

Next, we analyzed the enhancement of fluorescence experienced by an emitter within the tip, as compared with a non-enhancing substrate (silica or glass surface). As discussed previously, the tip region of the device exhibits a hotspot with uniformly distributed, highly confined electromagnetic field (Figure 1.4.8a). The emission enhancement was calculated using FDTD simulations (Figures 1.4.8b, c), where the net fluorescence enhancement experienced by a fluorophore is defined as a product of EM field intensity and quantum yield gain (Figures 1.4.9, 1.4.10). Quantum yield gain of fluorophores inside the tip was calculated using FDTD. A dipole source was placed at varied

locations along the x or y axis to monitor the radiation from the dipole and the tip structure. γ_r was obtained by measuring the transmission through a closed box around a dipole source (Equation 1.4.2).

$$\frac{\gamma_r}{\gamma_0} = \frac{P_{structure}}{P_0} \qquad \text{Equation 1.4.2}$$

γ_{nr} was obtained by subtracting the transmission through a closed box containing the waveguide tip structure from (Equation 1.4.3).

$$\frac{\gamma_{nr}}{\gamma_0} = \frac{P_{dipole} - P_{structure}}{P_0} \qquad \text{Equation 1.4.3}$$

Quantum yield was calculated using Equation 1.4.4 [51].

$$\eta = \frac{\gamma_r/\gamma_0}{1-\eta_0+\gamma_r/\gamma_0+\gamma_{nr}/\gamma_0} \qquad \text{Equation 1.4.4}$$

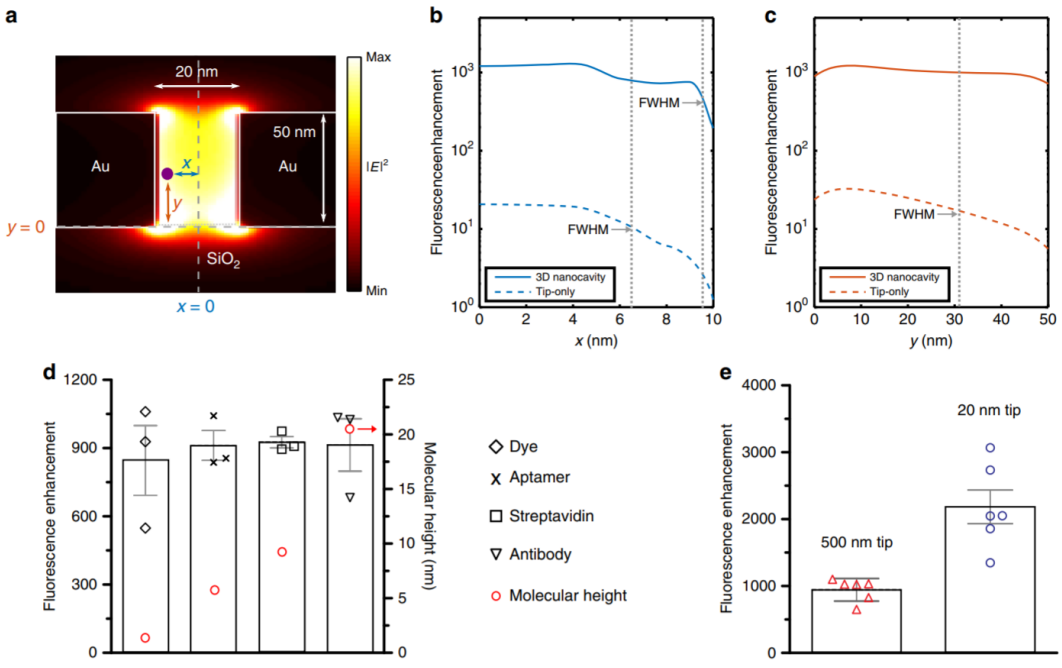

Figure 1.4.8 Overcoming electromagnetic field decay for molecular analysis. (a) Cross-section of the tip at the end of taper showing EM field intensity and placement of a fluorophore with distance along the x and y axis for a 500 nm long tip. Variations in net fluorescence enhancement, calculated as a

product between the EM enhancement and quantum yield gain, of the 3D nanocavity (solid line) and tip-only structure (dashed line) as a function of molecular position along the (b) x- and (c) y-axes. Metal-induced quenching effects are visible near the metallic sidewalls of both structures. The 3D nanocavity shows uniform fluorescence enhancement for about 95.5% (FWHM) of the x-axis and 100% of the y-axis. (d) Experimentally obtained enhancement factors calculated for various molecular assemblies using a tip with length 500 nm, demonstrating highly-enhanced fluorescence from all samples as a result of their placement within the plasmonic hotspot. The estimated height of the molecules from the silica surface has been shown. The near uniform mean enhancement indicates suitability towards using molecular assemblies of different heights, overcoming evanescent field decay typically associated with plasmonic nanostructures. Plot shows datapoints, mean and s.d. for three devices at each condition. (e) Increase in mean enhancement factor with decrease in tip length to 20 nm. Plot shows datapoints, mean and s.d. for six devices at each condition. Reprinted with permission from [61].

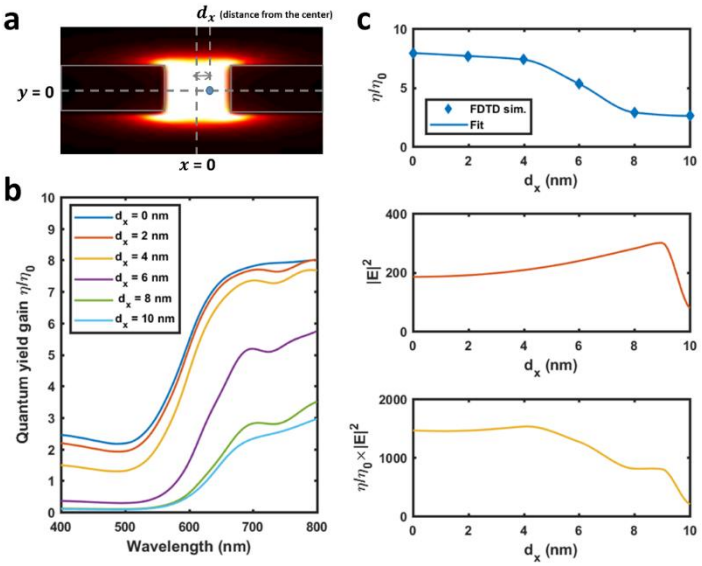

Figure 1.4.9 Quantum yield gain of an Alexa-750 fluorophore inside a 20-nm width and 50-nm height tip. (a) Cross-sectional view of the hotspot formed at the tip. d_x is the horizontal distance of a fluorophore from the center of the tip. (b) Comparison between the quantum efficiency at varied

horizontal locations calculated based on Eq. S4-3. Quantum yield gain is decreased as a fluorophore gets closer to the Au sidewall of the tip due to the quenching of fluorescent radiation. (c) Quantum yield gain η/η_0 (top), $|E|^2$ enhancement (middle), and $\eta/\eta_0 \times |E|^2$ (bottom) at 750 nm at varied horizontal locations. Reprinted with permission from [61].

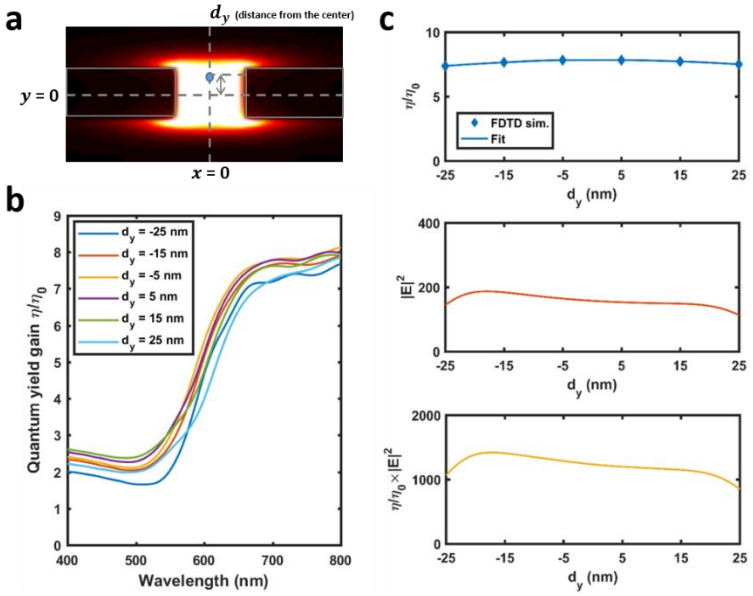

Figure 1.4.10 Quantum yield gain of an Alexa-750 fluorophore inside a 20-nm width and 50-nm height tip. (a) Cross-sectional view of the hotspot formed at the tip. d_y is the vertical distance of a fluorophore from the center of the tip. (b) Comparison between the quantum efficiency at varied vertical locations based on Eq. S4-3. Quantum yield gain does not change significantly with varied height of fluorophores. (c) Quantum yield gain η/η_0 (top), $|E|^2$ enhancement (middle), and $\eta \times |E|^2$ (bottom) at 750 nm at varied vertical locations. Reprinted with permission from [61].

As discussed previously, the 3D-tapered gap plasmon nanocavity provides superior $|E|^2$ uniformity within the gap compared with conventional MIM structures. Our analysis also shows that the 3D-tapered gap plasmon nanocavity allows greater radiative decay rate that results in up to 28.2%

enhanced quantum yield gain along the width of the channel as compared with the tip-only structure, thereby enabling ~500× greater net fluorescence enhancement (Figure 1.4.11, Figures 1.4.8b, c). For a 500 nm long tip, the expected fluorescence enhancement is >1000 for about 70 % of the channel width. The full-width half-maximum (FWHM) covers 95.5% of the x-axis with indication of fluorescence quenching very close to the metallic sidewalls (Figure 1.4.8b). Fluorescence enhancement is very uniform (~1000) along the y-axis and does not decline below half of the maximum enhancement throughout the channel height (Figure 1.4.8c). This is especially important as variation along the y-axis represents the increase in fluorophore height from the bottom silica surfaces. This can be a result of the size of molecule the fluorophore is attached to or based on number of molecules in the assembly. The simulations indicate that this variation should have minimal impact on the enhancement experienced by the emitter, which has been a longstanding challenge for plasmonics-enhanced fluorescence In order to experimentally verify the optimized fluorescence enhancement response predicted in Figure 1.4.8b, c, we performed tests using diversely-sized molecules including dye molecules, aptamers, smaller proteins and antibodies. These molecules were specifically bound to the 3D-tapered nanocavity, and fluorescence enhancement was analyzed compared with non-structured SiO2 control samples. While the dye molecules were covalently bound to the bottom silica surface, all other molecules were specifically bound to their respective recognition agents or antigens preassembled on the surface (see 1.6.3 Molecular binding tests). The expected height of the fluorophore from the silica base of the nanocavity is indicated in Figure 1.4.8d and varies from <1 nm to ~20 nm. The experimentally calculated enhancement performance of the device showed a uniform response for various molecular shapes and heights, which agrees with the simulation results shown in Figure 1.4.8c. We expect this device to maintain the same enhancement for molecular assemblies with height up to 50 nm, which is defined by the height of the tip for this device. The level of enhancement was dependent on the tip length as expected. For tips with length 500 nm, the enhancement was close to 950 whereas shorter tips (ltip = 20 nm) provided higher enhancement (EF~2200) due to stronger $|E|^2$ enhancement at the tip region for diverse molecular sizes (Figure 1.4.8e, Figure 1.4.12). These results matched the trend and values predicted earlier by simulation-based analysis (see 1.6.4 Calculation of experimental enhancement factor). As fluorescence enhancement is dependent on the quantum yield of the fluorophore used,

we also used another metric, enhancement figure of merit—which normalizes the enhancement with respect to the dye quantum yield and allows comparison of device performance to other nanostructures [27]. The device showed an enhancement figure of merit close to 260, which is one of the highest values obtained for fluorescence enhancement obtained using plasmonic nanostructures, and uniquely provides this enhancement independent of molecule size within the nanocavity tip.

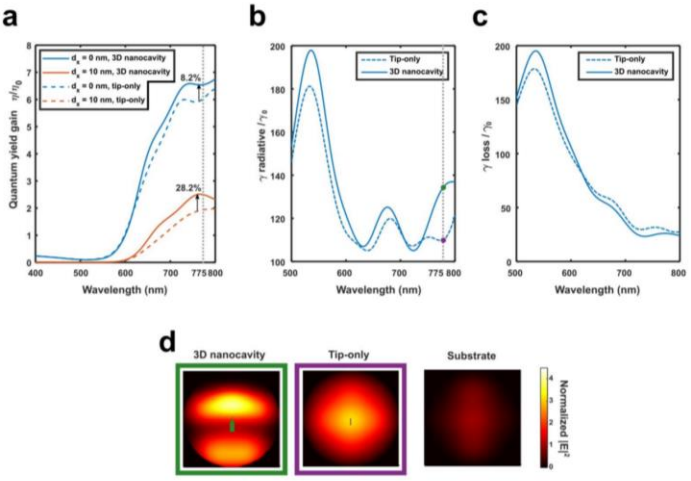

Figure 1.4.11 Comparison between quantum yield gain profiles of a fluorophore inside the 3D-tapered gap plasmon nanocavity and tip-only structure. (a) Quantum yield gain profiles of the 3D nanocavity (solid line) and tip-only (dashed line) structure at x = 0 (blue) and x =10 nm (red). Normalized (b) radiative decay rate and (c) non-radiative decay rate profiles of the 3D nanocavity (solid line) and tip-only structure (dashed line). d Normalized farfield projection of radiative intensity at 775 nm. Fluorophore was placed at x = 0, y = 25 nm inside the 3D nanocavity (green, left), inside the tip-only structure (purple, middle), and on the substrate (right). The intensity is normalized such that the far-field peak intensity from the substrate equals 1. The normalized radiative intensity peak ($\propto$ Tradiative/T0) represents the radiative decay rate ($\gamma r/\gamma 0$) at 775 nm shown as markers in (c). The enhanced radiative decay rate of the 3D nanocavity results in 8.2% – 28.2% greater quantum yield gain than the conventional MIM (tip-only) structure. Reprinted with permission from [61].

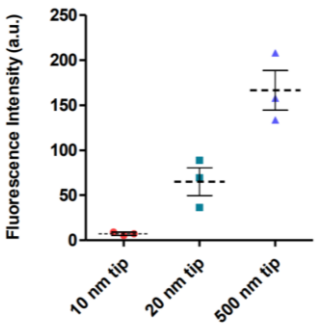

Figure 1.4.12 Fluorescence intensity with tip length. Fluorescence intensity (background subtracted) obtained using tips of various lengths after performing binding assay with biotin and SAF-750. Individual data points, mean and s.d. for 3 devices at each condition, are shown. Reprinted with permission from [61].

1.5 Conclusion

We have demonstrated 3D-tapered gap plasmon nanocavities, which provide one of the highest enhancements of fluorescence obtained by plasmonic nanostructures (EF: ~2200 with figure of merit ~260), independent of the size of the molecular assemblies used in the assay. Overcoming molecule size- and placement-dependent extreme variation in plasmonic fluorescence enhancement has been a major challenge restricting widespread application of this method in bioassays. The nanostructure geometry presented in this work demonstrates a way to overcome this limitation thereby improving the consistency and range of plasmon-enhanced emission for diversely sized assembly of molecules. Simultaneously, we also demonstrate capture and visualization of single antibodies at the tip as well as sensing of proteins at low concentrations (10 pM). These advantages can be readily transferred towards applications such as highly sensitive biosensing using molecular labels of varying sizes and analysis of single molecules or tightly controlled arrays of molecules for protein orientation, protein function, and biological polymer formation studies [45–47]. While the device geometry promises several benefits, weaknesses of the current fabrication process include low throughput using focused ion beam lithography and high footprint of the device compared with smaller nanostructures. Future

improvements can target the replacement of current fabrication process with wafer-scale methods including nanoimprinting, e-beam lithography, and template stripping for reproducible manufacturing of nanocavities in combination with anisotropic etching methods for the tapered portions. We may also see further improvement in device performance after replacing ion beam milling with alternative methods mentioned above, which are known to yield smoother device surfaces, and have shown such improvements in the past [27]. The presented device design can also provide advantages in other areas of nanophotonics for optical confinement, data-transfer, quantum optical communication, and molecular sensing in mid-infrared and terahertz domains.

1.6 Methods and materials

1.6.1 Device fabrication

3D-tapered nanocavity fabrication. Single-side polished silicon wafers with thermally grown SiO2 (thickness: 1 μm) were purchased from University Wafers, Boston, USA. E-beam evaporation was used to deposit 50 nm gold (Au) on the wafers. 3D-tapered nanocavity patterns were milled through the gold and silica using a FEI Nova 600 dual beam system as shown in Fig. 1. Au (50 nm) was deposited again using e-beam deposition. Second round of milling was performed using Nova 600 to remove gold from the bottom of the substrates, exposing the silica and to mill the tip.

1.6.2 Simulations

We used a commercial software developed by Lumerical Inc. for the FDTD analyses. In all analyses, the mesh size was 1 nm and uniform throughout the device area. For the $|E|^2$ and uniformity analyses, a 750-nm dipole source was placed at the tail-end of the 3D-tapered nanocavity body and the intensity of the guided AS mode was monitored across the cross-section of the tip $\overline{|E|^2}$ at each α was calculated by averaging the $|E|^2$ profile over the cross-sectional area (20 × 50 nm^2) of the tip. $\sigma_{|E|2}$ was calculated by normalizing the $|E|^2$ enhancement profiles (setting 1 as the highest) and calculating 2D standard deviation of the profiles over the cross-sectional area. 2D-tapered nanocavity was designed to provide only lateral confinement (body cross-sectional area: 150 × 50 nm^2) along with the same taper length of 500 nm and tip cross-sectional area (20 × 50 nm^2) as the 3D-tapered nanocavity. The tip-only structure was a simple MIM waveguide without a taper that provided the

same cross-sectional area (20 × 50 nm^2). The bowtie antenna was a set of two equilateral Au triangles (side length 140 nm, thickness 50 nm) separated by 20 nm on a 3-nm thick Cr layer on top of a 25-nm thick ITO [8,41], which provided the same cross-sectional area at the gap (20 × 50 nm^2). For the coupling efficiency into body analyses (Figures 1.4.3, 1.4.5), a 1.4-NA Gaussian source centered at 750-nm was focused onto either the tail-end or varied longitudinal locations (z) throughout the body. In both cases, transmitted power through the cross-section was calculated at each location of incidence. For the fluorescence enhancement analysis, a 750-nm dipole source was placed inside the tip and transmitted power through a closed box enclosing the dipole and tip was monitored in order to obtain radiative and non-radiative decay rates (Figures 1.4.9, 1.4.10).

1.6.3 Molecular binding tests

3-Aminopropyl-triethoxysilane (APTES) was obtained from Sigma-Aldrich, USA. The nanocavity chips were cleaned with acetone, methanol, and isopropanol prior to binding experiments. A 1% APTES solution was prepared in toluene (anhydrous) and allowed to bind on the chips for 30 min. This step functionalizes the silica surface with amino groups available for further binding. The substrates were washed with toluene to remove weakly bound APTES molecules. The chips were baked at 110 °C for 30 min and then cleaned again with DI water for 15 min. The samples were then dried with nitrogen. Alexa Fluor 750 NHS ester was purchased from Thermofisher Scientific USA and dissolved in DMSO (1 mg/ml). The solution was added to the substrates with stirring and dye molecules were allowed to bind to the functionalized substrates for one hour. The chips were then cleaned well with DMSO and water. A drop of water was placed on the chips, covered with a coverslip, and then imaged.

For aptamer sensing, insulin from bovine pancreas was purchased from Sigma Aldrich (USA). Insulin was mixed in PBS at a concentration of 10 μM. Solution was added to the chips and left undisturbed for an hour to allow physisorption of the peptide hormone to the surfaces. BSA (0.1%) was then added to the chips and allowed to interact with the surface to account for any nonspecific binding. An insulin-binding aptamer (sequence: 5′ GGT GGT GGG GGG GGT TGG TAG GGT GTC TTC 3′) with AF-750 conjugated to the 5′ end was obtained from IDT technologies (St. Louis, USA). Aptamer was dissolved at a concentration of 1 μM in a folding buffer (Tris: 10 mM;

$MgCl_2 \cdot 6H_2O$: 1 mM; NaCl: 100 mM; pH: 7.4) and added to the substrate for an hour. The samples were washed with folding buffer after an hour and then imaged.

Surface biotinylation was done with SPB (MW: 1000 and 5000) purchased from Laysan Bio Inc. (USA). For surface functionalization, SPB powder was dissolved in 50% ethanol: DI water. This solution was added to substrates with exposed silica surface and left undisturbed for an hour. The substrates were then washed with DI water.

For streptavidin binding, Streptavidin Alexafluor 750 conjugate (SAF-750) was purchased from Thermofisher Scientific (USA). Streptavidin in PBS (pH 7.4, concentration: 0.1 mg/ml) was added to chips with biotin monolayer and left undisturbed for an hour. The chips were then washed with DI water and imaged. A layer of water was maintained at all times on the chip through molecular functionalization and imaging. For Streptavidin bioassays, the concentration of streptavidin in PBS was varied while maintaining the duration of incubation (1 h).

For antibody binding, anti-biotin antibody (Mouse monoclonal (Hyb-8), IgG1, MW: 244 kDa) conjugated with DyLight 755 fluorophore (response similar to Alexafluor 750) were obtained from Novus Biologicals (USA). The antibody was diluted in PBS at a concentration of 0.05 mg/ml and added to the chips. The solution was left undisturbed for 2 h. The samples were then washed with DI water.

In order to test the behavior of smaller probes, dye molecules (AF-750) were covalently linked directly to the silica-base of the nanocavities. For molecule-specific bioassays, we utilized short chain (length: 30 basepairs) single-stranded DNA aptamers labeled with AF-750 at the 5´ end. These molecules form G-quadruplex tertiary structures with dimensions ranging between 2-4 nm [52] and were used to detect insulin (monomer diameter: 2 nm [53]) that was physically adsorbed within the nanocavities [54]. As shown previously (Figure 1.4.2b), proteins (StreptavidinAF 750, diameter: 5 nm) [55], which recognized and bound to biotinylated monolayers, (expected height: 3.5 nm) [56], were also utilized for on-chip assays. The polymeric biotin-streptavidin assembly provides an increase in probe-dimension as well as change in orientation as compared to the aptamer-based samples. Predominantly, bioassays rely on application of even larger proteins, i.e. antibodies for highly-specific detection of target molecules. IgG antibodies have a globular diameter around 15 nm, which can vary depending on the molecular mass of the antibodies and associated conjugates

[50,57]. The expected average fluorophore height shown in Figure 1.4.8e includes the diameter of the surface-bound antigen (insulin or biotin) added to the diameter of the biorecognition element (aptamer, streptavidin or antibody).

Topology and phase images of dried antibody monolayer on silica substrates were obtained on an AFM system (Bruker Dimension Icon, Santa Barbara, CA, USA) using a 100 μm long monolithic silicon cantilever (All-In-One-Al, NanoAndMore USA Corp (BudgetSensors), Watsonville, CA, USA). All the experiments were conducted under ambient laboratory conditions using tapping mode with a resonance frequency of about 350 kHz. Images were analyzed afterward by commercial software Nanoscope Analysis.

Fluorescence imaging was performed using a Leica DMI 6000 widefield fluorescence microscope. Scanning electron micrographs were taken using FEI Nova 600 and 200 dual beam systems. Images were analyzed using Fiji (ImageJ) software [58]. Graphs were created in Matlab and Graphpad Prism 5.01.

1.6.4 Calculation of experimental enhancement factor

Experimental fluorescence enhancement factors were calculated by comparing the ratio of molecular fluorescence on a flat silica surface as compared to molecules placed within the tips of the tapered waveguide structures. In Equation 1.6.1 [59,60], I1 is the integrated fluorescence intensity from N1 number of molecules placed inside the waveguide tip, and I2 is the total fluorescence intensity from N2 number of molecules on a flat silica surface.

$$EF = \frac{I1 \times N2}{I2 \times N1} \qquad \text{Equation 1.6.1}$$

Since, the labeling of the surfaces was performed using self-assembly using excess of molecules, we can assume the surfaces to have a uniform surface density of molecules, η. Then the number of molecules can be represented as: $N1 = \eta \times A1$ and $N2 = \eta \times A2$, where A1 is the surface area of silica within the tip and A2 is surface area of silica on the flat surface used as control. The uniform signal enhancement response shown by fluorophores attached to dimensionally varying probes for bioassays matches well with the response predicted by simulations (Figures 1.4.8-10). When multiplied with the backend coupling efficiency of the device body (2.38%) and the intensity

enhancement due to full-illumination mode, the simulation-derived effective EF is calculated to be ~460, which is close to the experimentally calculated EF shown in Figure 1.4.8e.

1.7 Bibliography

[1] D. Darvill et al., Phys. Chem. Chem. Phys. 2013, 15(38), 15709-15726.

[2] P. Goy et al., Phys. Rev. Lett. 1983, 50 (24), 1903-1906.

[3] R. G. Hulet et al., Phys. Rev. Lett. 1985, 55 (20), 2137-2140.

[4] E. Yablonovitch, Phys. Rev. Lett. 1987, 58, 2059-2062.

[5] M. Boroditsky et al., Lightwave Technol. 1999, 17 (11), 2096-2112.

[6] K. H. Drexhage, J. Lumin. 1970, 1, 2, 693-701.

[7] I. Gontijo et al., Phys. Rev. B 1999, 60 (16), 11564-11567

[8] A. Kinkhabwala et al., Nat. photonics 2009, 3(11), 654-657.

[9] O. L. Muskens et al., Nano Lett. 2007, 7(9), 2871-2875. DOI:10.1021/nl0715847

[10] J. R. Lakowicz, Anal. Biochem. 2005, 337 (2), 171-194.

[11] F. Tam et al., Nano Lett. 2007, 7(2), 496-501.

[12] J. Eid et al., Science 2009, 323, 133–138.

[13] B. A. Flusberg et al., Nat. Methods 2010, 7, 461–465.

[14] A. Ambrosi et al., Anal. Chem. 2009, 82, 1151–1156.

[15] S. Chen et al., Nano Lett. 2011, 11, 1826–1830.

[16] R. De La Rica & M. M. Stevens, Nat. Nanotechnol. 2012, 7, 821–824.

[17] G. Acuna et al., Science 2012, 338, 506–510.

[18] H. Yokoe & T. Meyer, Nat. Biotechnol. 1996, 14, 1252–1256.

[19] A. I. Dragan et al., Plasmonics 2012, 7, 739–744.

[20] A. L. Feng et al., Sci. Rep. 2015, 5, 7779.

[21] P. Anger et al., Phys. Rev. Lett. 2006, 96, 113002.

[22] P. Bharadwaj et al., Nanotechnology 2006, 18, 044017.

[23] S. Kühn et al., Mol. Phys. 2008, 106, 893–908.

[24] R. Bardhan et al., Small 2008, 4, 1716–1722.

[25] D. Punj et al., Nat. Nanotechnol. 2013, 8, 512–516.

[26] R. Chikkaraddy et al., Nature 2016, 535, 127–130.

[27] V. Flauraud et al., Nano Lett. 2017, 17, 1703–1710.

[28] V. S. Volkov et al., Nano Lett. 2009, 9, 1278–1282.

[29] M. Schnell et al., Nat. Photonics 2011, 5, 283–287.

[30] D. K. Gramotnev & S. I. Bozhevolnyi, Nat. Photonics 2014, 8, 13–22.

[31] E. Bermúdez-Ureña et al., Nat. Commun. 2015, 6, 7883.

[32] D. Pile & D. K. Gramotnev, Appl. Phys. Lett. 2006, 89, 041111.

[33] D. K. Gramotnev et al., Phys. Rev. B 2007, 75, 035431.

[34] S. Vedantam et al., Nano Lett. 2009, 9, 3447–3452.

[35] H. Choo et al., Nat. Photonics 2012, 6, 838–844.

[36] W. Bao et al., Science 2012, 338, 1317–1321.

[37] J. Conway, Efficient optical coupling to the nanoscale 2006, Vol. 68.

[38] J.-S. Huang et al., Nano Lett. 2009, 9, 1897-1902.

[39] Y. Xu et al., Plasmonics 2011, 6, 337- 343.

[40] H. T. Miyazaki & Y. Kurokawa, Phys. Rev. Lett. 2006, 96, 097401.

[41] K. D. Ko et al., Nano Lett. 2010, 11, 61–65.

[42] W. Cai et al., Adv. Mater. 2010, 22, 5120–5124.

[43] L. Chaiet & F. J. Wolf, Arch. Biochem. Biophys. 1964, 106, 1–5.

[44] H. Grubmüller et al., Science 1996, 271, 997–999.

[45] S. H. Park et al., Nano Lett. 2005, 5, 729–733.

[46] J. D. Brodin et al., Nat. Chem. 2012, 4, 375–382.

[47] A. D. Doyle et al., J. Cell Biol. 2009, 184, 481–490.

[48] M. J. Levene et al., Science 2003, 299, 682–686.

[49] Y. H. Tan et al., ACS Nano 2008, 2, 2374–2384.

[50] T. Werner et al., Proc. Natl Acad. Sci. USA. 1972, 69, 795–799.

[51] D. L. Mack et al., Nat. Commun. 2017, 8, 14513.

[52] N. An et al., Proc. Natl. Acad. Sci. USA. 2014, 111, 14325-14331.

[53] T. Blundell et al., Diabetes 1972, 21, 492-505.

[54] W. Yoshida et al., Biosens. Bioelectron. 2009, 24, 1116-1120.

[55] W. A. Hendrickson et al., Proc. Natl. Acad. Sci. USA. 1989, 86, 2190-2194.

[56] N. Dos Santos et al. Biochim. Biophys. Acta Biomembr. 2007, 1768, 1367-1377.

[57] Y. H. Tan et al., ACS Nano 2008, 2, 2374-2384.

[58] J. Schindelin et al., Nat. Methods 2012, 9, 676–682.

[59] W. Cai et al., Surf. Sci. 1998, 406, 9-22.

[60] E. J. Smythe et al., Nano Lett. 2009, 9, 1132-1138.

[61] S. Kumar et al., Nat. Commun. 2020, 11, 1-9.

Chapter 2

NANOPHOTONIC APPLICATION TO INTRAOCULAR PRESSURE (IOP) SENSING

This chapter was adapted from:

Lee, J., Park, H., Du, J. et al., A microscale optical implant for continuous in vivo monitoring of intraocular pressure. Microsystems & Nanoengineering 3, 17057 (2017). DOI: 10.1038/micronano.2017.57

Han, S. J. †, Park, H. †, Lee, J. O., & Choo, H. Effect of optical aberrations on intraocular pressure measurements using a microscale optical implant in ex vivo rabbit eyes. Journal of Biomedical Optics, 23(4), 047002 (2018). DOI: 10.1117/1.JBO.23.4.04700

†These authors contributed equally.

2.1 Introduction to glaucoma

Glaucoma is a disease that damages the optic nerves caused by an increased intraocular pressure (IOP) and a leading cause of reduced vision or blindness [1,2], with a significant portion of patients exhibiting progressive vision loss despite treatment [3–6]. There are two different types of glaucoma: open angle glaucoma and closed angle glaucoma. Open angle glaucoma accounts for 90% of glaucoma patients and is caused by an increased resistance to drainage of aqueous humor at the trabecular meshwork and Schlemm's canal, which leads to pressure build-up inside the eye (Figure 2.1.1, left). Closed angle glaucoma is a more severe type of glaucoma that is caused by a structural change in the anatomy of the eye that results in the obstruction of outflow through the drains (Figure 2.1.1, right).

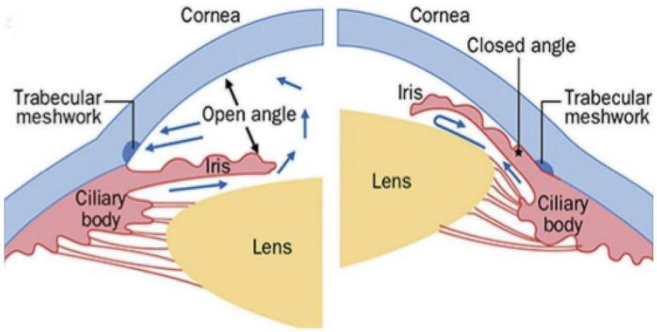

Figure 2.1.1 Illustration of two main types of glaucoma; open angle glaucoma (left) and closed angle glaucoma (right). Reprinted with permission from [83].

Current therapies aim to lower IOP, which is the only known modifiable risk factor and thus the key parameter for clinical monitoring [7–10]. Despite its central role in glaucoma management, IOP is measured only a few times a year using specialized tonometers in the clinic. These infrequent 'snapshot' views of IOP are problematic because an individual's IOP can fluctuate on a daily, weekly, or seasonal basis [11–16]. IOP can be influenced by activity, diet, and other factors that are not completely understood [17–21]. If the daily (or more frequent) IOP pattern of a glaucoma patient is available, the physician can predict disease progression and personalize therapy based on detailed knowledge of individualized trends in IOP [22]. This is similar to the approach used to treat other chronic progressive diseases such as hypertension and diabetes, in which home monitoring of blood pressure and blood sugar is integral to disease management. In addition, pathophysiological studies and drug-discovery research demand accurate, frequent, and preferably automated assessments of IOP in humans and testing animals [23,24]. Over recent decades, animal models have significantly contributed to the understanding of the cellular and molecular bases of glaucoma [25]. However, the relationship between IOP and other factors, such as obesity, genetic contributions [26,27], retinal ganglion cell death [28], age, and ocular blood circulation [29], are not fully understood yet due to the limited accuracy and usability of conventional tonometry.

2.2 IOP sensing techniques

All tonometry approaches available in practice, such as rebounding tonometry, pneumotonometry, dynamic contour tonometry, and Goldmann applanation tonometry, perform indirect measurements of IOP. The accuracy of these approaches is adversely influenced by variations in individual corneal biomechanics [30] and measurement complexity, rendering them unsuitable for use in large-scale animal studies. Recently developed contact-lens-based IOP sensors also provide indirect IOP measurements. They track changes in the corneal scleral angle as a surrogate measure and provide relative IOP trends in mV rather than mmHg [31–40]. Such measurements can only be obtained for up to 24 h because of side complications that accompany long-term use [41–43].

To overcome the aforementioned limitations, implants based on radio frequency (RF) technologies have been used to monitor IOP [47–58]. Due to the inductive coils requiring a larger size to achieve a longer readout distance and better accuracy, the typical size of these implants ranges from a millimeter to a few centimeters [52,59]. As a result, *in vivo* measurements have thus far been obtained only with large RF implants that measure 0.5 to 1 cm in diameter [51,64,65]. Such large implants have damaged surrounding 1 tissues and led to medical complications [66,67].

2.3 Design and principle of nanophotonic IOP sensor

In this chapter, we present a microscale implantable optical sensor (900 μm in diameter) for use with a remote optical readout detector in clinics, laboratories, and potentially home environments. This approach enables (1) an IOP sensor in a microscale size that allows minimally invasive sensor implantation in the eye using well-stablished intraocular lens (IOL) [61] or silicone-haptics procedures, (2) a practical readout distance of 3 to 5 cm, which can be extended beyond 10 cm, (3) the use of near-infrared (NIR) light from a tungsten bulb that is not perceived by the patient, and (4) an excellent accuracy in IOP readouts (mean average: 0.29 mm Hg; maximum deviation: 1 mm Hg) over the clinically relevant IOP range of 0–40 mm Hg.

The nanophotonic IOP sensor is a hermetically sealed hollow disk that serves as a pressure-sensitive cavity that supports optical resonances. The top half of the sensor is a deformable nanodot-array-integrated silicon-nitride (SiN) membrane attached to a micromachined silicon ring. The bottom half is a hollow disk made of Si (Figures 2.3.1a and b). The optical resonance is supported by reflections from the nanodot-integrated SiN membrane and bottom Si mirror. The two parts are assembled into

a cavity using medical grade epoxy, resulting in a 7-μm gap between the SiN membrane and the Si mirror.

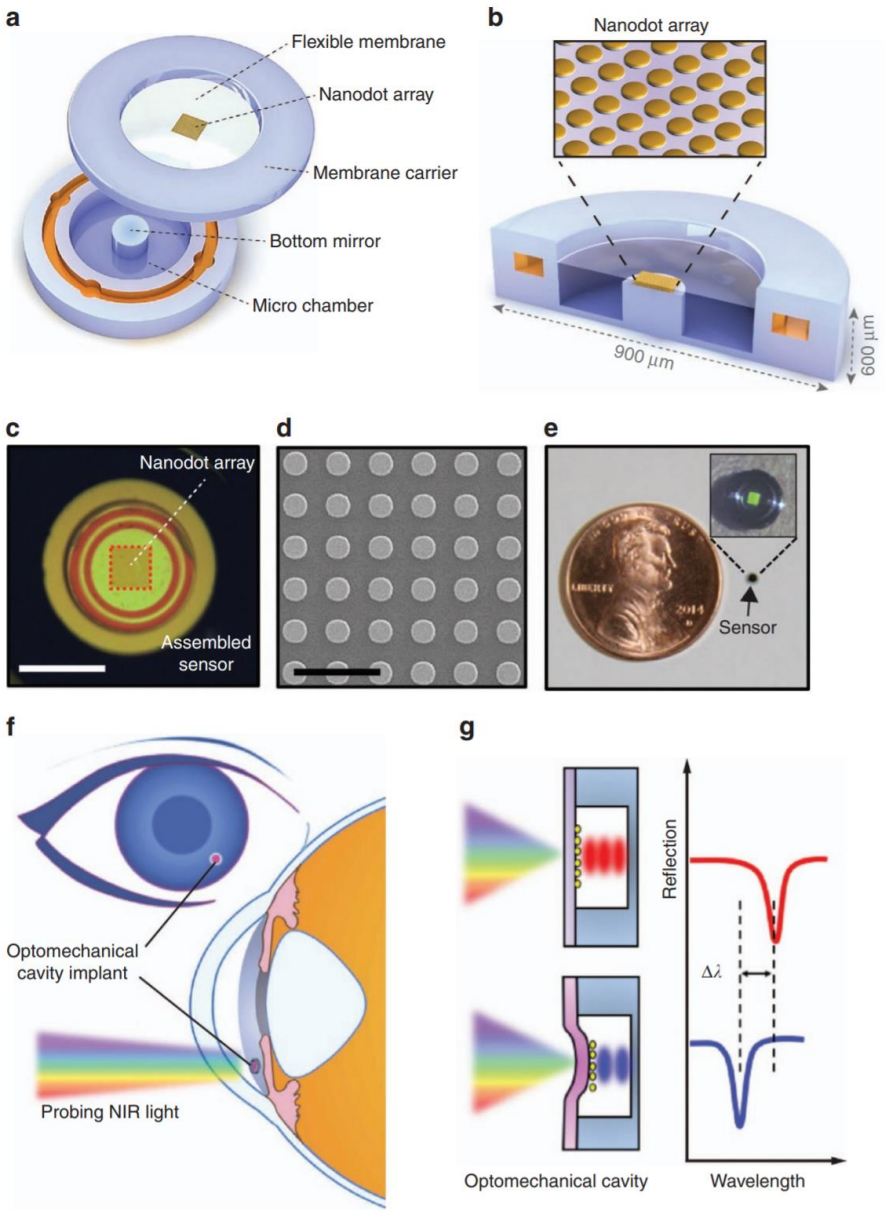

Figure 2.3.1 A microscale nanophotonic intraocular pressure (IOP) sensor and operating principles. (a) A three-dimensional (3D) illustration of the top structure with a nanodot-embedded deformable SiN membrane and the bottom structure with a Si reflective surface in the center and a cylindrical hollow cavity, before assembly. (b) A cross-sectional schematic view of an assembled sensor and a zoomed-in image of the nanodot array in the SiN membrane (inset). (c) A microscope image taken

perpendicular to the device surface showing the square nanodot array in the middle of the sensor (scale bar: 500 μm). (d) Scanning electron microscopy (SEM) image of the gold nanodot array on a SiN membrane: the diameter of each dot is 600 nm (scale bar: 2 μm). (e) A photograph of a completed device with a diameter of 900 μm (inset: a zoomed-in image of the sensor taken at an angle at which the rectangular nanodot array assumes a green-blue color). (f) A nanodotenhanced IOP sensor located in the anterior chamber and interrogated using NIR light. (g) A schematic illustrating the shift in the sensorreflected resonance as a function of the gap distance within the sensor's optical cavity, which in turn is related to IOP. Reprinted with permission from [84].

The optical resonances inside the nanophotonic IOP sensor are optimized using a gold nanodot array fabricated onto the deformable SiN membrane (Figures 2.3.1b–d). By optimizing the diameter of the gold nanodots, we can match the reflectivity of the nanodot-integrated SiN membrane to the that of the bottom Si surface, which maximizes the amplitude of the optical resonance (Figure 2.3.2a). The nanodot array diameter for optimal membrane reflectivity were studied using the finite difference time domain (FDTD) simulations and experimental measurements. While the periodicity and gold nanodot height were fixed at 1000 nm and 100 nm, respectively, the diameter of the gold nanodot forming a square lattice array was varied from 400 nm to 800 nm at steps of 50 nm. These dimensions were fabricated on SiN membranes as well as implemented in the FDTD simulations (Figure 2.3.2b). Gold nanodots of different diameters were fabricated using electron-beam lithography (see 2.7.1 Nanophotonic IOP sensor fabrication). For simulations, the optical constants of gold from Johnson and Christy were used within the wavelength range of 550 – 950 nm [62]. A uniform mesh size of 5 nm in all *x*, *y*, and *z* directions was used for the gold nanodot array. Figures 2.3.2c-e show the experimentally obtained reflection spectra. In Figure 2.3.2d, the average experimental reflection within the wavelength range of 800 nm – 1000 nm was calculated for each nanodot diameter and compared with the results from the FDTD simulations. As expected, the resonance (peak-to-valley) amplitude is maximized when the nanodot diameter is 600 nm, which matches reflection of the nanodot-integrated SiN membrane to that of Si (0.3) (Figure 2.3.2e).

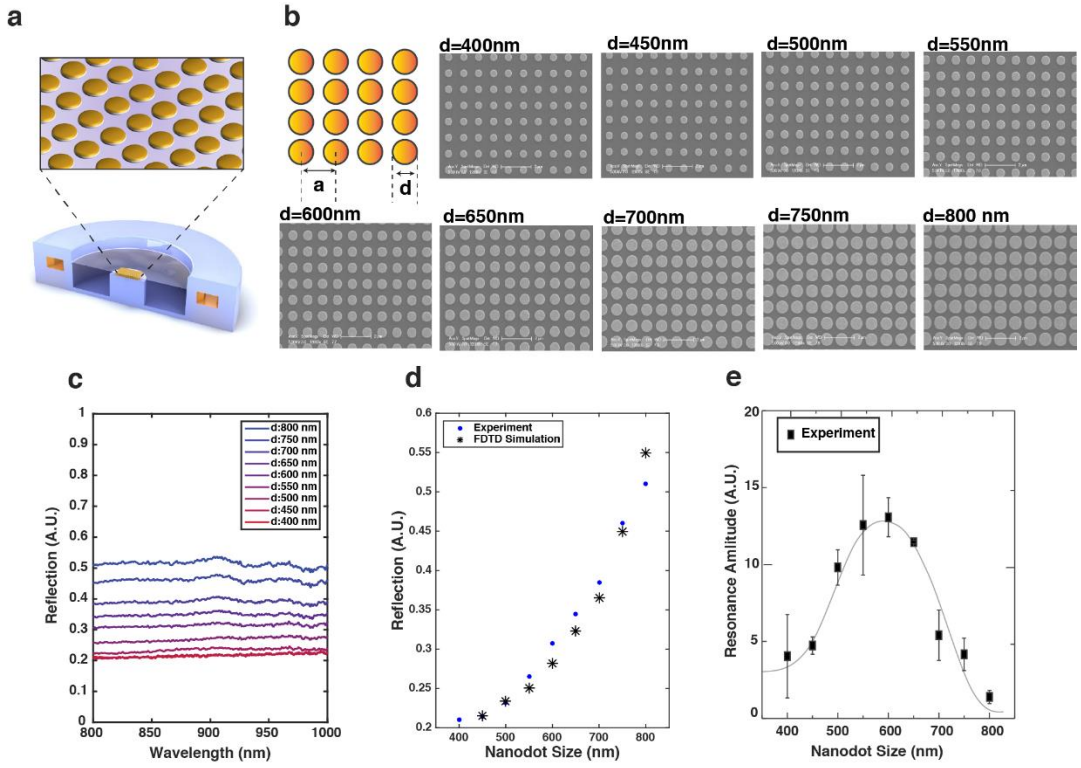

Figure 2.3.2 Au-nanodot array designs for cavity resonance optimization. (a) A schematic illustration of the Au-nanodot array embedded in the Si3N4 membrane. (b) SEM images of the Au-nanodot arrays with nine different diameters (400, 450, 500, 550, 600, 650, 700, 750, and 800 nm) spaced at an array-pitch size of 1000 nm. The height of the individual dots, which is the thickness of the gold, is 100 nm. (c) The reflection measurements as a function of the Au-dot diameters. The dot arrays exhibit almost wavelength-independent reflectivities in the wavelength range of interests. (d) The comparison between the average of experimentally measured reflection vs. FDTD-simulation results within 800-1000 nm wavelength range for nine different Au-dot diameters. (e) Experimentally characterized resonance amplitudes as a function of Au-nanodot diameters; the optimal diameter was found to be 600 nm. Reprinted with permission from [84].

Based on the above analysis, a 200 × 200 μm^2 array with a nanodot diameter of 600 nm and periodicity of 1000 nm was fabricated to optimize the amplitude of the cavity resonance (Figures 2.3.1c, d). The final sensor dimensions after assembly are 900 μm in diameter and 600 μm in height,

thus the area of the assembled sensor including the surrounding Si frame is 0.635 mm^2 and the volume is 0.381 mm^3 (Figure 2.3.1e). Moreover, the area of the core optomechanical cavity is 0.283 mm_2 (600 μm in diameter) occupying only 44% of the entire sensor area and suggesting further miniaturization. This compact size is an order of magnitude smaller than the state-of-the-art research devices [46,63,64] and three orders of magnitude smaller than commercially available sensors [58]. For IOP monitoring, the sensor is implanted into the eye where the nanodot-integrated SiN membrane is exposed to IOP and broadband invisible NIR light (800– 1100 nm) from a tungsten light bulb (Figure 2.3.1f) (see 2.7.2 Surgical procedures for *in vivo* testing). At a given IOP, the sensor has a corresponding gap size that supports a resonance located at a specific wavelength (Figure 2.3.1g, top). When IOP increases, the nanodot-integrated SiN membrane is deflected inwards, which results in a decreased gap that supports a new resonance that is shifted to a shorter wavelength (Figure 2.3.1g, bottom). When IOP decreases, the SiN membrane deflects outwards, which results in an increased gap that supports a resonance shift to a longer wavelength. The location of these resonance peaks and dips can be identified using a commercially available mini-spectrometer and used to determine the gap size and therefore the ambient pressure (IOP).

We chose the near infrared (NIR) wavelength range of 800– 1100 nm as our light source to take advantage of the fact that NIR light is minimally absorbed in the cornea and the aqueous humor and is also invisible to the human eye. SiN was selected as the membrane material due to its high optical transparency, large refractive index, extremely low water permeability, and robust mechanical resilience. The relatively high refractive index of 1.98 for SiN allows the implementation of a sensor cavity with a strong optical resonance in saline or aqueous humor because the resonance amplitude of an optical cavity is heavily dependent on the reflectivity of its surfaces. If the reflectivity is too high or too low, the resonance may become very sharp or flat, which significantly lowers the SNR [65–67]. The thickness of the SiN membrane was optimized to maximize the amplitude of the sensor resonance. The resonance spectrum of the nanophotonic IOP sensor is the result of combined effects of two separate resonances: one from the thickness of the membrane, and the other from the cavity gap between the membrane and the bottom silicon surface. The resonance from the silicon nitride membrane defines the outer envelope of smaller ripples created by the resonances from the gap (Figure 2.3.3). Our FDTD analysis determined that the optimal thickness of the silicon-nitride

membrane was 0.3 μm, which maximized the magnitude of the outer envelope in the 800–1100 nm range.

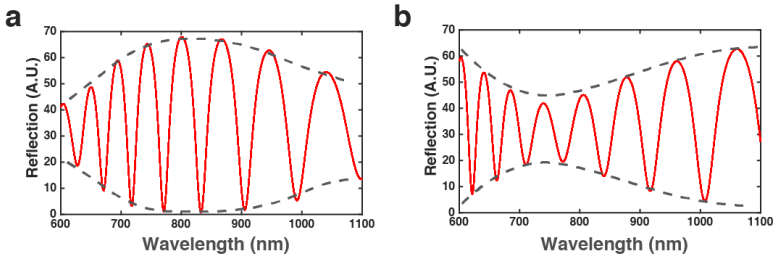

Figure 2.3.3 Optimizing the Si_3N_4 membrane thickness in the NIR range. (a) The calculated reflection spectrum when the Si_3N_4 membrane thickness is 300 nm; the peak-to-valley height is maximized in the wavelength range of interest. (b) The calculated reflection spectrum when the Si_3N_4 membrane thickness is 190 nm; this would be the worst case that lowers the amplitude and degrades the remote readout performance. Reprinted with permission from [84].

The optimal diameter for the 0.3 μm-thick SiN membrane was determined using a series of finite-element-method (FEM) simulations and a high-order analytical model for a thin diaphragm [68,69]. For the pressure range of 0 – 40 mmHg, SiN membranes with diameters between 200 and 1000 μm were all found to exhibit linear deformation as a response to hydrostatic pressure changes. 600 μm was chosen as the SiN-membrane diameter to facilitate the fabrication and assembly of the cavity.

The accuracy, range, and linearity of the fabricated nanophotonic IOP sensors were tested in a controlled pressure chamber filled with saline (Figure 2.3.4a). The pressure inside the chamber was varied between 0 and 100 mmHg at steps of 0.05 mmHg using an integrated water column and a programmable syringe pump (NE 1000, ABC Scientific, CA, USA). The chamber pressure was monitored using an electronic pressure sensor (1210 Pressure Sensor, TE Connectivity Ltd., Schaffhausen, Switzerland) with an accuracy of ± 0.1 mmHg. A custom-built table-top detection system for broadband NIR light (800–1100 nm) (Figure 2.3.4a) was used to excite the resonances inside the nanophotonic IOP sensor through an optically transparent window of the chamber. The optical resonances from the sensor were collected using a commercially available spectrometer (MAYA 2000 Pro, Ocean Optics, Dunedin, FL, USA) that was connected to the detection system. As expected from the previous discussion, the resonance dips in the reflection spectra shifts to shorter

wavelengths as the cavity gap decreases with increasing chamber pressure (Figure 2.3.4b). The experimentally measured spectral shifts (Figure 2.3.4b) are in good agreement with the analytical shifts (Figure 2.3.4c). The analytical shifts were obtained from an optomechanical model (OMM) that consisted of physical and material parameters that enables calculation of ambient pressure for any given spectrum measurement. The pressure calculation was performed by one-to-one mapping between the measured spectrum and its corresponding IOP [62]. In the pressure range of 0-40 mmHg, the nanophotonic IOP sensor showed highly linear responses, and the deviations from the electronic pressure-gauge reading remained below 1 mmHg with root mean square error (RMSE) of 0.29 mmHg (Figure 2.3.4d).

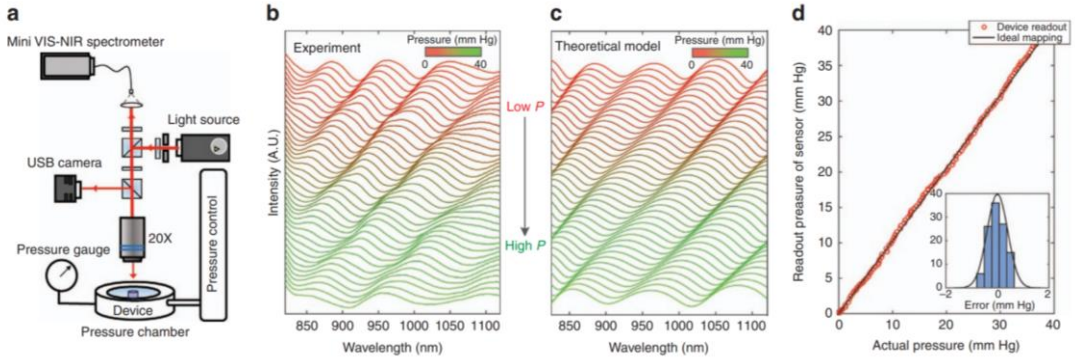

Figure 2.3.4 Sensor characterization in a controlled pressure chamber. (a) Intraocular pressure (IOP) sensor characterization in a controlled pressure chamber with a digital pressure gauge. A schematic of the sensor optical resonance detector is shown above the pressure chamber. (b) Experimentally determined spectra from the sensor in the pressure range from 1 to 40 mm Hg with the spectra corresponding to 1 mm Hg shown at the top and the spectra for 40 mm Hg shown at the bottom. The spectra for the intervening IOPs are shown in sequence from top to bottom. (c) Theoretically predicted spectra corresponding to the pressure range from 1 (top spectra) to 40 mm Hg (bottom spectra). (d) Highly linear, very close one-to-one matching between the sensor measurements (vertical axis) and the digital pressure-gauge readouts (horizontal axis). The black line shows a theoretical perfect match of sensor and digital pressure-gauge readings, and the red circles indicate actual experimental measurements corresponding to the pressure readout based on the optomechanical model (OMM). Histogram shows the error distribution (RMSE: 0.29 mm Hg). Even in the worst case,

the sensor reading was within ±1 mm Hg of the digital pressure-gauge readings. Reprinted with permission from [84].

2.4 *Ex vivo* and *in vivo* demonstration of nanophotonic IOP sensor

The sensors that were characterized in the pressure-controlled chamber in chapter 2.3 were characterized in *ex vivo* rabbit eyes. The sensors were inserted through a clear corneal incision and placed directly on top of the iris with the nanodot-integrated SiN membrane facing up. (Figures 2.4.1a, b). The IOP inside the *ex vivo* eyes was increased via saline infusion at steps of 1 mmHg. The resulting IOP was monitored using a 21-gauge needle that was directly inserted into the anterior chamber and connected to the same digital pressure gauge. The resonance spectra of the nanophotonic IOP sensor were collected using the same custom-built system shown in Figure 2.3.4a. The peak locations of the same sensor from both the test chamber (Figure 2.4.1c) and the *ex vivo* eye characterizations (Figure 2.4.1d) are in good agreement. The difference between the readouts from the same sensor inside an *ex vivo* eye and the digital pressure gauge was less than 1.3 mmHg throughout 10-27 mmHg (Figure 2.4.1e).

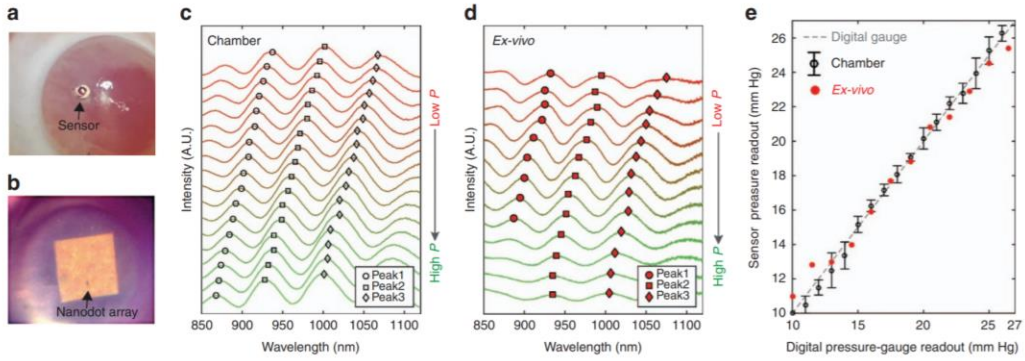

Figure 2.4.1 Sensors in ex vivo rabbit eyes and spectra collected over a range of induced intraocular pressures (IOPs). (a) A photograph of an implanted sensor inside the anterior chamber of an ex vivo rabbit eye. (b) A microscope image showing the 200-μm2 nanodot array of a sensor taken thorough the cornea and the aqueous humor in an ex vivo eye. (c) The spectra from a sensor tested in the controlled pressure chamber for pressures. The open symbols show the location of the three reflected resonance peaks. (d) The spectra from the same sensor shown in c when tested in an ex vivo eye as the internal pressure of the ex vivo eye was varied using a 21-gauge needle and a syringe pump. Red

symbols show the location of the three reflected resonance peaks. (e) Mapping comparison between the sensor's pressure readout obtained from pressure chamber testing (black circle) and ex vivo eye testing (red circle). The vertical axis indicates sensor measurements, and the horizontal axis indicates the digital pressure-gauge readouts. The black error bars indicate standard deviations (n=15). Reprinted with permission from [84].

Sensors with performance metrics that had been fully characterized in the pressure chamber were implanted into the eyes of New Zealand white rabbits to investigate their performance *in vivo*. Two methods were used for sensor implantation. In one method, individual sensors were attached to an intraocular lens (IOL) (Figure 2.4.2a) and placed into the lens capsular bag following the surgical extraction (See 2.7.2 Surgical procedures for *in vivo* testing) of the crystalline lens (Figures 2.4.2b, c). A cavity of approximately 1 mm in diameter and 0.5 mm in depth was mechanically cut into the IOL. Sensors were placed into the cavity using medical grade UV adhesive (Loctite 3321, Loctite Corp. Rocky Hill, CT, USA) with the nanodot-integrated SiN membrane side facing outwards from the IOL cavity. In the other method, sensors were attached to 125-μm-thick clear silicone-membrane haptics (Figure 2.4.2d), and rolled up for insertion into the anterior chamber through a clear corneal incision. The silicone haptics were manually fabricated from medical grade silicone membrane (125 μm thick) (BioPlexus, Ventura, CA, USA) into a barbell shape approximately 2.5 mm in width and 12.5 mm in length. The two haptic arms then spontaneously unfolded to extend into the iridocorneal angle and mechanically anchor the sensor within the anterior chamber (Figures 2.4.2e, f).

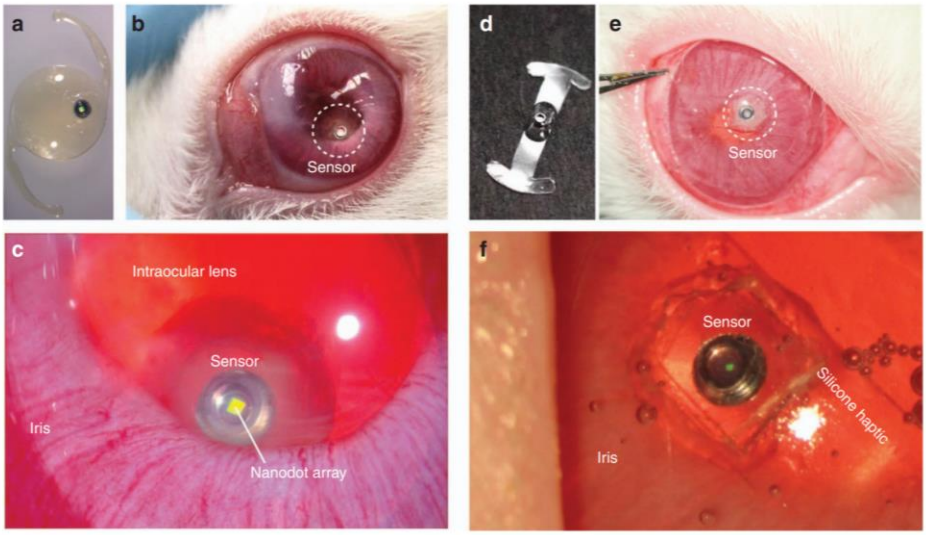

Figure 2.4.2 Nanophotonic IOP sensors in rabbit eyes. (a) An IOP sensor attached to a one-piece acrylic IOL. The sensor is the black circular object with a central bright area that represents the nanodot array. (b) A nanophotonic IOP sensor (located within the dashed circle) implanted into a rabbit eye. (c) A higher magnification view of the same sensor as in b. The bright square in the middle of the sensor represents the nanodot array. The translucent material surrounding the sensor is the epoxy adhesive used in the sensor assembly and sensor attachment to the IOL. (d) A nanophotonic IOP sensor attached to thin silicone membrane haptics. (e) A nanophotonic IOP sensor mounted on silicone haptics (located within the dashed circle) implanted into a rabbit eye. (f) Higher magnification of the same sensor as in e. The bright square in the middle of the sensor represents the nanodot array. The silicone haptics appear transparent after implantation into the eye. Reprinted with permission from [84].

Next, we characterized the *in vivo* performance of implanted sensors in rabbit eyes using the custom-built detector. The data reported here were obtained from five sensors implanted in five rabbits (or one sensor per rabbit) for up to 4.5 months. The optical alignment was carried out by monitoring both camera image and the spectra in real time. The initial alignment between the sensor and the detector was achieved relatively easily by using a coaxially integrated USB-camera and maximizing the reflection back from the sensor until the sensor appeared as a bright spot saturated with light in

the image. The bench-top testing showed that the bright spot guarantees an optical alignment within ± 3°. Then the alignment was further improved by manipulating the translational stages of the detector until the resonance amplitude captured by the spectrometer appeared maximized. This would lead to an alignment accuracy within ± 1°. Furthermore, in order to reduce the potential error in angular alignment during *in vivo* measurements, we continuously recorded the spectra at a sampling rate of 10 Hz for 20 s and choose only the highest-quality spectra with SNR over 15 dB. Using this high-speed sampling approach allowed us to filter out erroneous measurements with low SNRs in post-measurement processing and to minimize the IOP-estimation error that could results from movements, such as breathing, of the test subject.

Examples of 20 individual resonance spectra collected over 2 s from a sensor following the *in vivo* implantation are shown in Figure 2.4.3a. The captured resonance signals were stable, with an excellent signal-to-noise ratio (SNR) of 15 dB. For testing the ability of nanophotonic IOP sensors to detect the short term increase and decrease in IOP *in vivo*, we injected 5% hypertonic saline intravitreally into the eyes of anesthetized rabbits with the implanted nanophotonic IOP sensors to cause a quick increase in IOP that peaked at 25–30 mmHg followed by a gradual decrease to the baseline over 1.5–2 h. The resonance spectra of the sensors were captured in parallel with IOP measurements using a commercial rebound tonometer (TonoVet, Icare, Vanda, Finland) for 45–60 min after the injections. The experimentally induced IOP profiles measured by the nanophotonic IOP sensor and by the TonoVet are shown in Figure 2.4.3b. Prior to the saline injection, the sensor IOP readout was 8 mmHg and the TonoVet-derived IOP was 6.3 mmHg. The first sensor IOP readout captured at 2 min after the intravitreal saline injection showed an increase in IOP to 27.0 mmHg, which was followed by a gradual decrease over 43 min. The same trend in IOP was recorded by the TonoVet (Figure 2.4.3b). Moreover, the nanophotonic IOP sensors provided readouts for up to 138 days after the *in vivo* implantation. Figure 2.4.3c shows six IOP measurements obtained from each of an implanted sensor and the TonoVet on Days 0, 20, 40, 76, 110, and 138 after implantation. IOP readings from the sensor on each day were averaged from 200 measurements made over 20 s: these were 7.8 ± 0.16 (Day 0), 5.3 ± 0.24 (Day 20), 7.7 ± 0.27 (Day 40), 12.3 ± 0.19 (Day 76), 3.9 ± 0.45 (Day 110), and 6.6 ± 0.54 (Day 138) mmHg. The corresponding TonoVet IOP readings were 6.7 ± 0.6 (Day 0), 6.0 ± 1.0 (Day 20), 8.7 ± 0.6 (Day 40), 11.3 ± 0.6 (Day 76), 5.7 ± 0.6 (Day 110)

and 6.3 ± 0.6 (Day 138) mmHg. Each TonoVet IOP readout is an average of 3–6 individual measurements.

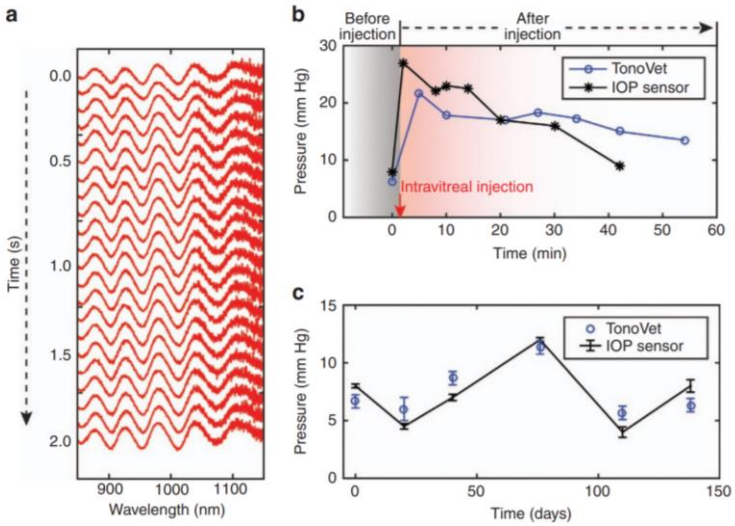

Figure 2.4.3 *In vivo* spectra and IOP measurements. (a) A 2 s block of stacked resonance spectra from a 20 s remote optical detector measurement session performed at 10 Hz. The first spectra obtained at the start of the 2 s block are displayed at the top of the stack. The spectra recorded at subsequent times are sequentially stacked towards the bottom. (b) The IOP measurements before and after intravitreal injection of hypertonic saline to cause transient IOP elevation at 138 days after implantation. The sensor-derived IOPs (black symbol, n =20) and the TonoVet-derived IOPs (open blue circles, n=6) mirror each other and show a rise in IOP after injection followed by a gradual decline over the following 43– 55 min. Error bars indicate standard deviations. (c) A comparison of IOP derived from sensor measurements vs TonoVet IOP measurements over a 138-day period. Reprinted with permission from [84].

2.5 Effect of optical aberrations on IOP readouts using nanophotonic IOP sensor

The nanophotonic IOP sensors presented in the previous chapters provide more accurate and frequent IOP monitoring and to improve treatment outcomes. Because NIR light is used to excite the resonance and obtain the IOP readout, the performance of the sensing system is inevitably influenced by optical aberrations that originate from the refractive-index profiles of the cornea and the anterior chamber of the eye. Although such optical aberrations and their influence on the

performance of intraocular lenses have been characterized extensively using Shack–Hartmann (SH) sensors in previous clinical studies [70–76], the relationship between the performance of the implantable optical IOP sensor and ocular optical aberrations has yet to be studied. Clearly understanding the relationship between the ocular aberrations and the quality of IOP monitoring could ensure the effective and proper use of implantable optical IOP sensors across diverse patient groups.

In this chapter, we characterize the optical aberrations present in the corneas and anterior chambers of *ex vivo* rabbit eyes and examine their influence on the accuracy and signal-to-noise ratio (SNR) of IOP monitoring using the nanophotonic IOP sensor implants (Figures 2.5.1a, b). The aberrated wavefronts of the optical reflection from an implanted sensor are related to the distortion and dislocation of a focal point, which in turn affects the accuracy and SNR of optical IOP monitoring (Figure 2.5.1c). A customized setup was developed by coaxially integrating an SH sensor and a commercially available spectrometer to measure consecutively both the optical aberrations of the *ex vivo* eyes and the reflected optical spectra from the implanted nanophotonic IOP sensors (Figure 2.5.1d, see 2.7.3 Experimental setup and calibration for aberration study).

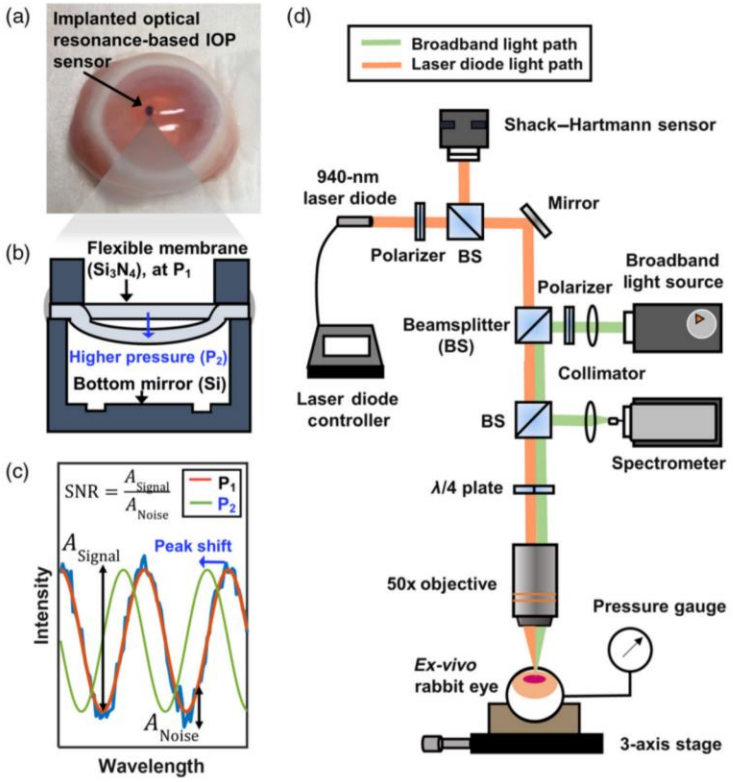

Figure 2.5.1 Principles and setup for aberration measurements using the IOP sensor implantation. (a) A photograph of an ex vivo rabbit eye after IOP-sensor implantation. (b) A cross-sectional illustration of the hermetically sealed optical IOP sensor: an increase in IOP from P1 to P2 deflects the flexible membrane and changes the cavity's optical resonance. (c) The optical resonance spectra reflected from the IOP sensor: the increase in IOP from P1 to P2 blueshifts the resonance, and there is one-to-one mapping between the resonance spectrum and the corresponding IOP. The accuracy is calculated by extracting the peak position, retrieving an IOP value, and comparing with the pressure-gauge readout. The SNR is calculated by extracting the amplitudes of the signal and noise and calculating the ratio between the two. (d) An illustration of the experimental setup for measuring optical aberrations and resonance spectra. Two light sources, the 940-nm laser diode (orange) and the broadband light source (green), share most of the optical path that includes an objective lens and an ex vivo rabbit eye. Reprinted with permission from [85].

First, we implanted a well-characterized reference chip coated with a thin photoresist film in *ex vivo* rabbit eyes and measured the optical spectra and the wavefront aberrations consecutively; doing so revealed the influence of the aberrations on the accuracy and SNR of the optical spectra obtained from the implanted reference chip by eliminating the influence of ambient pressure or variation in the sensor geometry on the measurements. To study the influence of the optical aberrations on the sensor performance, we obtained one spectral and five aberration measurements in sequence and grouped them as one set. For the spectral measurement, we used only the broadband light source and collected an optical spectrum ranging from 800 to 1100 nm from an implant through the integrated spectrometer every 100 ms at a resolution of 0.22 nm. The sensor used in the experiments showed two peaks within the bandwidth of the collected spectrum. After collecting the optical spectra, we turned off the broadband light source and turned on the laser diode to perform five consecutive aberration measurements every 1 s at a frame rate of 79 fps. Between each set of measurements, we irrigated the *ex vivo* rabbit eyes with saline solution to maintain a uniform tear film. The reference chip was prepared by coating a silicon wafer with 15-μm-thick photoresist (Microchemicals GmbH, Germany) and dicing it into 1-mm × 1-mm chips. The static, unchanging resonance came from the photoresist layer. Ten of these chips were inserted into 10 *ex vivo* rabbit eyes (Pel-Freeze, Rogers, Arkansas) through a 1-mm incision on the side of the corneas and placed at the center of the anterior chamber. A commercially available high-accuracy (0.26 mm Hg) digital pressure gauge (3584K11; McMasterCarr, Elmhurst, Illinois) was connected to a 21-gauge needle that in turn was inserted directly into the anterior chambers of the *ex vivo* eyes to provide reference IOP values. The optical spectra obtained from the sensor measurements were analyzed using a custom-built MATLAB™ signal processing algorithm that detects the location of the peaks and valleys and calculates the corresponding IOP value [77]. The aberration-measurement data were processed using the software provided with the SH sensor (Thorlabs, Newton, New Jersey). We included tip and tilt in our analysis because they play an important role in the resonance of optical cavities. The root-mean-square (rms) wavefront error was calculated by averaging the values of the lowest 21 Zernike coefficients (representing up to the fifth Zernike order) obtained in the five consecutive measurements. The Zernike orders and terms used in our work are summarized in Table 2.5.1 [78].

Zernike order	Radial/ azimuthal degree (n, m)	Expression	Aberration
First	$(1, -1)$	$2\rho \sin(\theta)$	Tilt
	$(1, 1)$	$2\rho \cos(\theta)$	Tip
Second	$(2, 0)$	$\sqrt{3}(2\rho^2 - 1)$	Defocus
	$(2, -2)$	$\sqrt{6}\rho^2 \sin(2\theta)$	Oblique astigmatism
	$(2, 2)$	$\sqrt{6}\rho^2 \cos(2\theta)$	Vertical astigmatism
Third	$(3, -1)$	$\sqrt{8}(3\rho^3 - 2\rho)\sin(\theta)$	Vertical coma
	$(3, 1)$	$\sqrt{8}(3\rho^3 - 2\rho)\cos(\theta)$	Horizontal coma
	$(3, -3)$	$\sqrt{8}\rho^3 \sin(3\theta)$	Vertical trefoil
	$(3, 3)$	$\sqrt{8}\rho^3 \cos(3\theta)$	Oblique trefoil
Fourth	$(4, 0)$	$\sqrt{5}(6\rho^4 - 6\rho^2 + 1)$	Primary spherical
	$(4, -2)$	$\sqrt{10}(4\rho^4 - 3\rho^2)\sin(2\theta)$	Oblique secondary astigmatism
	$(4, 2)$	$\sqrt{10}(4\rho^4 - 3\rho^2)\cos(2\theta)$	Vertical secondary astigmatism
	$(4, -4)$	$\sqrt{10}\rho^4 \sin(4\theta)$	Oblique quadrafoil
	$(4, 4)$	$\sqrt{10}\rho^4 \cos(4\theta)$	Vertical quadrafoil
Fifth	$(5, -1)$	$\sqrt{12}(10\rho^5 - 12\rho^3 + 3\rho)\sin(\theta)$	Vertical secondary coma
	$(5, 1)$	$\sqrt{12}(10\rho^5 - 12\rho^3 + 3\rho)\cos(\theta)$	Horizontal secondary coma
	$(5, -3)$	$\sqrt{12}(5\rho^5 - 4\rho^3)\sin(3\theta)$	Vertical secondary trefoil
	$(5, 3)$	$\sqrt{12}(5\rho^5 - 4\rho^3)\cos(3\theta)$	Oblique secondary trefoil
	$(5, -5)$	$\sqrt{12}\rho^5 \sin(5\theta)$	Vertical pentafoil
	$(5, 5)$	$\sqrt{12}\rho^5 \cos(5\theta)$	Oblique pentafoil

Table 2.5.1 Zernike coefficients of the first five orders [78].

Figure 2.5.2a shows the rms-wavefront error obtained in double-pass aberration measurements reflecting off the reference chips. The rms-wavefront errors were 0.10 to 0.26 μm. When spectral measurements were made on the reference chips implanted in ex vivo eyes, the locations of the

resonance peaks deviated by 2.33 ± 1.41 nm from the reference-chip measurements made in water (Figure 2.5.2b). We observed no significant correlation between the total rms-wavefront error and the deviation in resonance-peak positions. When we analyzed the deviation in terms of the rms-wavefront error of each Zernike order, the first-order Zernike coefficients (tip and tilt) had the strongest correlation to the peak-location error (Figures 2.5.2c, d). The SNR of the obtained spectra from the implanted reference chips showed a negative correlation with the rms-wavefront error (Figure 2.5.2e). We observed no single dominant Zernike coefficient that was strongly correlated with the SNR. Even the optical spectrum obtained in the presence of the highest rms-wavefront error (0.26 μm) still showed a robust SNR of 22.8 dB, well above the required 15-dB minimum SNR for IOP measurements.

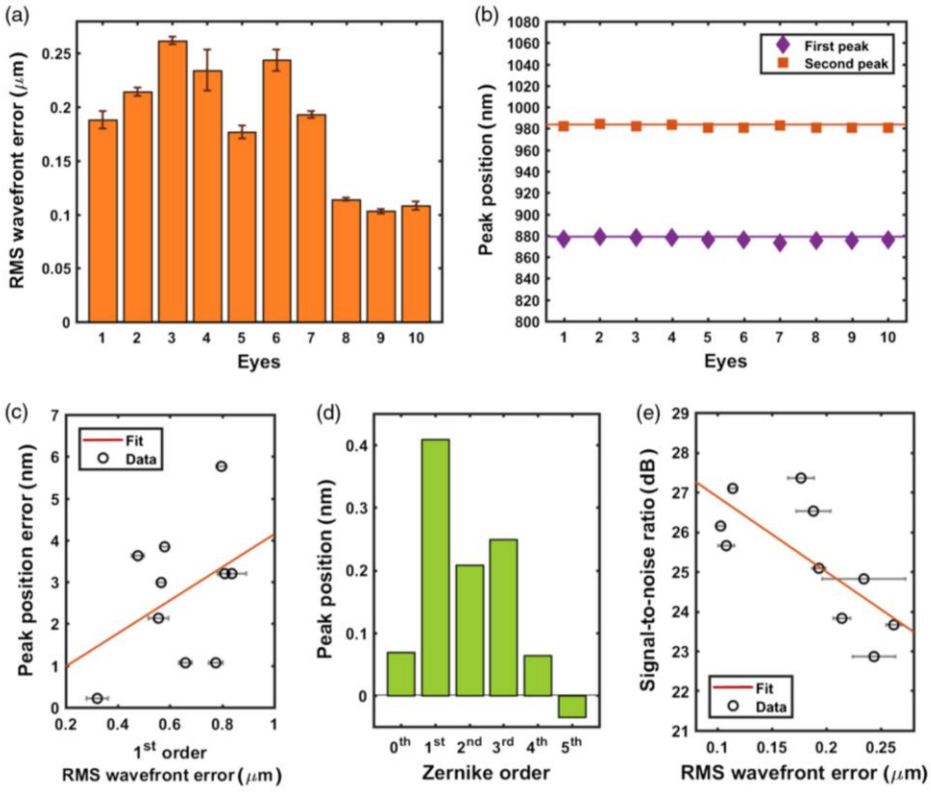

Figure 2.5.2 Measurements of reference chips implanted in 10 *ex vivo* rabbit eyes. (a) rms-wavefront error of the readouts from the reference chips. (b) Comparison between the peak locations in the optical spectra of a mock chip submerged in water (solid line) and implanted in *ex vivo* rabbit eyes

(squares and diamonds). (c) The absolute errors in the measured peak locations plotted against the first-order Zernike rms-wavefront error. (d) Correlation coefficient of each Zernike order in relation to the error in the measured peak position. (e) SNR of the optical spectra of implanted reference chips plotted against the rms wavefront error. Reprinted with permission from [85].

Next, we studied the effects of the aberrations on the quality of IOP readout using the nanophotonic IOP sensors with a micro-optical cavity. Before the experiments were performed, each sensor was characterized and calibrated using the 0.55-NA objective to remove any readout errors that could originate from the experimental setup. A sensor mounted on a flexible strip was implanted through a 3-mm incision on the side of the cornea and positioned at the center of the anterior chamber of 10 ex vivo rabbit eyes (Figure 2.5.1a), whereupon we sutured the incision to prevent leakage. The first five eyes (#1 to 5) were measured without injection of saline solution, whereas the last five eyes (#6 to 10) were injected with saline solution to emulate the IOP levels observed in living rabbits, resulting in IOP values of 16 to 20 mmHg. After the measurements of each eye, a sensor was retrieved and rinsed in isopropyl alcohol and deionized water for reuse and the used ex vivo rabbit eye was disposed. While the pressure of five *ex vivo* rabbit eyes (#1 to 5) was maintained at their original values of <6 mm Hg, the other five *ex vivo* rabbit eyes (#6 to 10) were injected with saline, resulting in pressures of 10 to 17 mmHg (Figure 2.5.3a). The rms-wavefront errors of the *ex vivo* eyes with saline injection were 0.38 to 0.94 μm, which were higher than the 0.21- to 0.68-μm range measured in the *ex vivo* eyes without injection (Figure 2.5.3b). The values of the IOP-readout error from the implanted sensors were smaller than 1 mmHg with an accuracy of 0.58 ± 0.32 mm Hg (Figure 2.5.3c), and the absolute values of the IOP error increased with rms-wavefront error (Figure 2.5.3d). The factor contributing most to the IOP error was the third-order Zernike term (Figure 2.5.3e), which corresponds to comatic and trefoil aberrations. Figure 2.5.3f shows that the SNR of the optical resonance spectra reflected from the implanted sensors decreased with rms-wavefront error.

The magnitudes of the optical aberrations that we characterized in the *ex vivo* rabbit eyes were very close to the values reported previously in other studies [79]. Our rms-wavefront errors from all measurements, which lie within 0.37 ± 0.23 μm, are slightly larger than previously reported *in vivo*

values, likely because of posthumous distortion of the eye geometry. In the reference-chip testing, the first-order Zernike coefficients presenting tip and tilt showed the highest correlation (r = 0.41) with erroneous shifts observed in the locations of the resonant peaks (Figure 2.5.2d). This was due to misalignment between the measurement setup and the reference chip. It was challenging to achieve perfect normal incidence between the optical axis of the measurement setup and the surface of the implanted reference chips because the precision of chip placement inside the *ex vivo* rabbit eyes was limited. The second- (defocus and astigmatism) and third-order (coma) Zernike coefficients were also correlated with the peak-location error, with the third-order coefficient being slightly more dominant. This is again attributed to the fact that defocus and coma are closely related to the precision of the optical alignment. It is also due to the dominance of coma in the native aberration of rabbit eyes [80]. This outcome is consistent with the principles of thin-film interference or Fabry–Perot cavity resonance; the interference or resonance is heavily dependent on the optical path length, which is determined by the angle of incidence [80].

A similar trend is observed between the rms-wavefront error of each Zernike order and the readout error of the IOP sensors (Figure 2.5.3e), except that the first-order Zernike coefficients, namely tip and tilt, were not as dominant as in reference-chip testing. This indicates that we accomplished better measurement alignment when measuring the IOP sensors. Unlike the implanted reference chips with a 1 × 1-mm2 flat reflective surface, the IOP sensors have a smaller, recessed sensing region made of two different surfaces that tend to be more angle sensitive. This angle sensitivity requires better optical alignment during measurements. Therefore, the correlation between the first-order Zernike coefficients and the IOP error became relatively weak. The third-order rms-wavefront error, which represented coma, showed the strongest correlation with the IOP error, and its correlation magnitude of 0.29 was close to the 0.25 observed during the reference-chip measurements (Figure 2.5.2d), indicating that the comatic aberrations that we observed in both cases were most likely a part of the native aberrations present in the *ex vivo* rabbit eyes [80]. The second most contributing factor for the IOP error was the second-order rms wavefront error, which represents defocus. In addition to the inherent second-order rms wavefront error to the rabbit cornea, the deformable membrane of the sensor contributed to the increase in the second-order rms-wavefront error and its correlation to the IOP error. This trend is consistent with the previous study that showed that the second-order rms-

wavefront error originating from a deflected membrane was more sensitive to IOP than the fourth- and higher-order rms-wavefront errors [81].

When the sensors were implanted at three different radial distances from the pupil center in the anterior chamber (Figures 2.5.4a, b), however, the first-order Zernike coefficients became the dominant factor that increased the total rms-wavefront error (Figure 2.5.4c) and the IOP error (Figure 2.5.4e). As the IOP sensor became farther from the center of the pupil, the curvature of the cornea also increased and caused a larger degree of refraction at the interfaces, resulting in significant tip and tilt. Although the third-order Zernike coefficients show the same trend as the first-order ones, the magnitude of the first-order Zernike coefficients is much greater than that of the third-order ones. The dominance of the first-order Zernike coefficients explains the underestimated IOP readouts because of the redshift of the peaks from the sensors positioned farther away from the pupil center. Unlike the first- and third-order terms, the second- and fourth-order rms wavefront errors decreased at a greater distance from the pupil center. This is partly attributed to the smaller defocus term in the second-order rms wavefront error as the depth of the sensor location decreased and enabled better focusing. In addition, both the second- and fourth-order coefficients include astigmatism terms, which are negatively correlated with the depth of the sensor location. When a sensor is located closer to the cornea, the focused light illuminates through a smaller area on the cornea, thereby introducing less astigmatism.

The SNR of the optical spectra obtained from the reference-chip measurements was 22.8 to 27.5 dB (Figure 2.5.2e), which exceeds the 7 to 23 dB of the IOP sensors as shown in Figure 2.5.3f. This is partly due to the larger measured/reflected area (1 mm × 1 mm) of the implanted reference chips compared with that of an implanted IOP sensor (0.6 mm in diameter). The major factor that decreased the SNR in both cases was the presence of the larger aberrations (Figures 2.5.2e, f). The larger aberrations came from the implant and/or the biomechanics of ex vivo rabbit eyes. The IOP sensor introduced extra aberration due to its flexible surface geometry.43 The native aberration of the sensors (0.168 ± 0.014 μm) accounts for the increase in the average aberration in Figure 2.5.3b (0.514 μm) when compared with that in Figure 2.5.2a (0.184 μm). Additionally, the increase in IOP and the variation in the Young's modulus of the corneas could result in the increase in the radius of corneal curvature and the increased aberration [82].

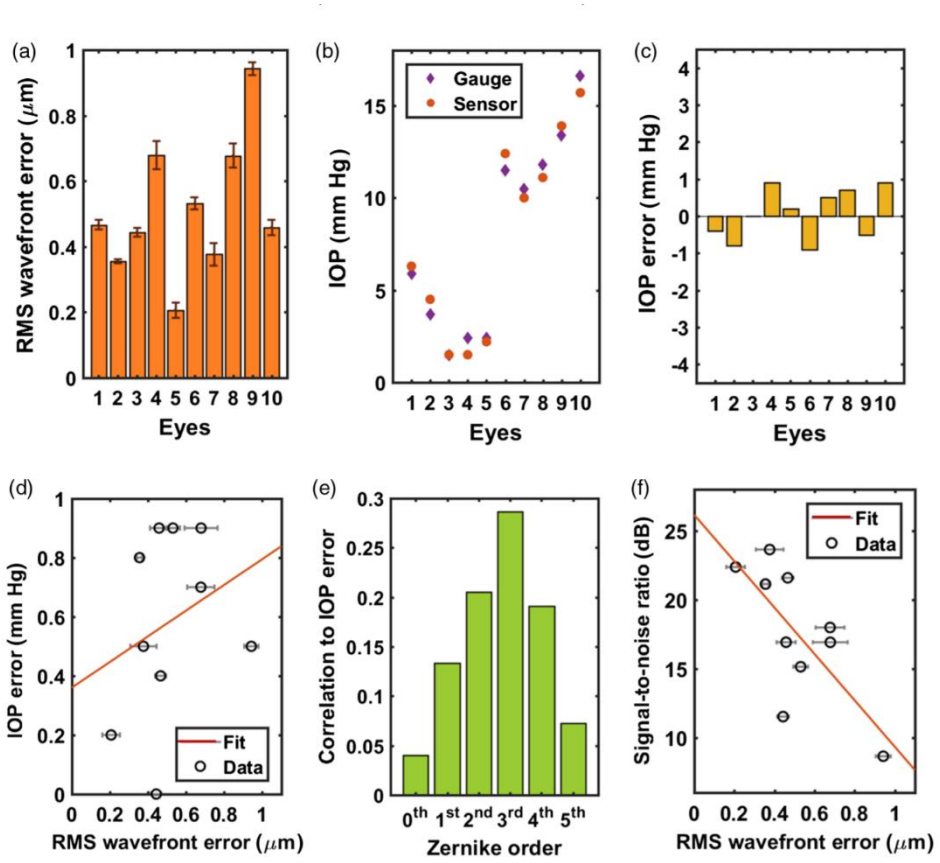

Figure 2.5.3 Aberrations, accuracy, and SNR measured using optical cavity implants in 10 ex vivo rabbit eyes. (a) rms-wavefront errors present in the reflection from implanted nanophotonic IOP sensors. Eyes #6 to 10 were injected with saline to increase the IOPs. (b) Comparison between the measured IOP values obtained from an implanted nanophotonic IOP sensor and a digital pressure gauge. (c) IOP error in the readouts from an IOP sensor. (d) Absolute IOP error plotted against the rms-wavefront error. (e) Correlation coefficient of each Zernike order in relation to the absolute IOP error. (f) SNR of the optical spectra of an implanted nanophotonic IOP sensor plotted against the rms-wavefront error. Reprinted with permission from [85].

The reduction in the SNR of the readouts under the greater rms-wavefront errors was observed in both reference-chip testing and IOP-sensor testing as well as in sensor-location testing that involved three sensors implanted at three different radial distances (Figure 2.5.4g). When compared with the

SNR of the readouts in reference-chip testing and IOP-sensor testing (Figures 2.5.2e, f), the SNR values obtained from this experiment (Figure 2.5.4f) followed a similar fitting line to those used in Figures 2.5.2e and 2.5.3f. Furthermore, the dominance of the first Zernike order was observed in the case of sensor-location testing (Figure 2.5.4d) but not in the case of IOP-sensor testing (Figure 2.5.3e). These outcomes indicate that the SNR of the readouts was primarily dependent on the total rms-wavefront error and was not particularly dependent on a single Zernike order. With no significant reduction in the SNR near the edge of the anterior chamber, this optical-resonance-based IOP-sensing implant is highly promising for use in human eyes without interrupting the vision.

Finally, we investigated the effect of the position-dependent aberrations on IOP measurements by implanting the sensors at multiple locations inside an *ex vivo* rabbit eye and correlating IOP with spectral measurements. Three nanophotonic IOP sensors were implanted and positioned radially at three different locations inside the anterior chamber of an *ex vivo* rabbit eye. A cross-sectional view of the three sensors placed at different positions is shown in Figure 2.5.4a. Three IOP sensors were attached to a strip at an interval of 2.5 mm, and the strip with the sensors was inserted through an incision and positioned inside the anterior chamber of an *ex vivo* rabbit eye (Figure 2.5.4b). The rms-wavefront error measured on each IOP implant is shown in Figure 2.5.4c. The rms-wavefront error increased with the distance from the implant to the center of the pupil or the optical axis of the eye. The first-order Zernike coefficients contributed the most to the larger rms-wavefront error observed at a greater distance from the center of the pupil (Figure 2.5.4d). The IOP readings from the three implanted sensors and the reference pressure gauge are plotted in Figure 2.5.4e. The sensor located at the farthest possible distance (5 mm) from the pupil center showed the largest IOP error of 0.9 mmHg but still remained below 1 mmHg, which is the clinically accepted maximum IOP error. In Figure 2.5.4f, the rms-wavefront error increased with the distance of the sensor from the center; consequently, the SNR of the optical spectra obtained from the IOP sensor decreased but stayed above 15 dB, which was the minimum SNR required for the sensor readout.

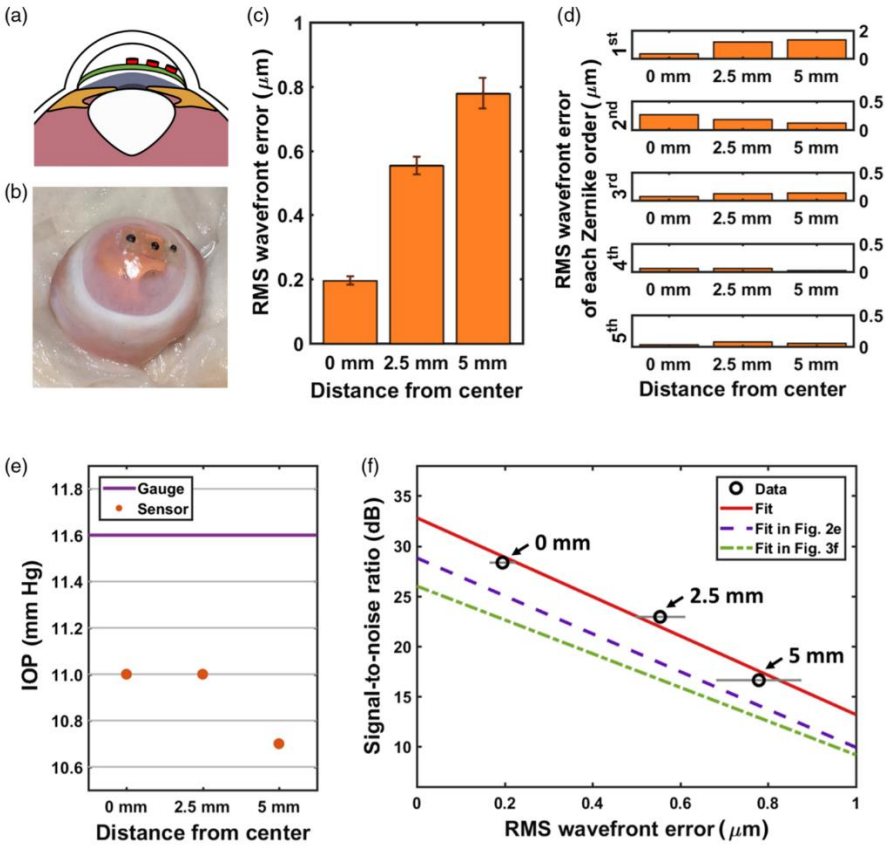

Figure 2.5.4 Measurements using three IOP sensors implanted at three different locations. (a) A cross-sectional illustration of the IOP sensors placed at three different locations. (b) A photograph of the three IOP sensors implanted inside the anterior chamber of an ex vivo rabbit eye. (c) The rms-wavefront error of the readout from each implanted IOP sensor. (d) rms-wavefront error of each Zernike order at different locations. (e) Comparison between the readings from the digital pressure gauge and the implanted IOP sensors. (f) SNR of the optical spectra of the implanted IOP sensors plotted against the rms-wavefront error. Reprinted with permission from [85].

2.6 Conclusion

Chapter 2 provided proof of concept for the remote detection of IOP from an implanted nanophotonic IOP sensor using invisible NIR light. The sensor is extremely compact and measures less than 1 mm in size. The bench testing in a pressure-controlled chamber demonstrated IOP readings in the clinically useful range of 0–40 mm Hg with an average accuracy of 0.29 mm Hg and in the *ex vivo*

eyes with an accuracy of ± 1.3 mmHg when measured against a commercial pressure gauge in both cases. If we limit the measurement range to, for example, between 10 and 11 mmHg, the sensor provided a much-improved pressure resolution of 0.07 mmHg. Such a fine level of pressure resolution easily exceeds the 1-mmHg resolution observed in commercial tonometers and is very promising. *In vivo* testing showed that implanted nanophotonic IOP sensors were able to reliably measure short-term changes in IOP that matched concurrently obtained TonoVet IOP readings. Furthermore, the sensor performance was also confirmed over a period of 138 days. The remote optical detector also has a simple configuration that allows easy optical alignment for use in a laboratory and clinics, and it can be further simplified and implemented in a form of a hand-held detector for use in the home environment. In addition, the effect of optical aberrations on the accuracy and the SNR of optical IOP monitoring obtained using the nanophotonic IOP sensors were studied. Both reference chips and nanophotonic IOP sensors showed high accuracy (15 dB). These results indicate that the use of optical cavity implants shows great promise for accurate and easy monitoring of IOP.

More precise and detailed characterization of our sensor's in vivo performance in subsequent work will require improved reference-IOP measurements in the eye. If nanophotonic IOP sensors are eventually used in the clinical setting, sensors mounted on silicone haptics can potentially be implanted in all glaucoma patients in addition to those undergoing lens extraction and IOL placement. Sensors attached onto the IOLs were implanted using standard surgical techniques for lens phacoemulsification and IOL implantation. This surgical procedure, independent of an attached sensor, can cause corneal edema and a substantial inflammatory tissue reaction in the rabbit eyes, particularly during the first 1–2 weeks after surgery. On the other hand, sensors mounted on silicone haptics did not elicit any noticeable inflammatory reaction in the anterior chamber after implantation, and the ocular recovery was excellent even on the second day after surgery with only mild incisional edema. Tissue buildup following a 4-month implantation period was noted to be minimal with no evidence of toxicity. The current version of the nanodot-enhanced IOP sensor is almost an order of magnitude smaller than sensors based on the LC coupling, and further miniaturization is possible. With further sensor refinements and detector automation, the system can become a viable choice for patient-initiated IOP monitoring in the home environment and drug-discovery research in labs.

2.7 Methods and materials

2.7.1 Nanophotonic IOP sensor fabrication

The top half of the sensor with a SiN membrane was created by growing 2 μm-thick thermal silicon dioxide (SiO2) and a 300 nmthick silicon-nitride (SiN) layer using a low pressure chemical vapor-deposition technique in sequence on a double-sidepolished wafer (diameter: 4 inches; thickness: 300 μm). The SiN and SiO2 layers on one side of the wafer were completely removed using reactive ion etching, followed by buffered hydrofluoric (BHF) acid. The hollow circular opening in the top structures was created by first depositing a 300-nm-thick Al2O3 layer in an e-beam evaporator (Mark 50 System, CHA Industries, Inc., Fremont, CA, USA) onto the cleaned side of the wafer. Photolithography (photoresist: AZ 9245, AZ Electronic Materials, USA Corp., Branchburg, NJ, USA) was then used to define solid disks in the Al2O3 layer as masks, and Bosch deep reactive ion etching (Plasmalab System 100 RIE/ICP, Oxford Instruments, Abingdon, UK) was performed through the wafer at an etch rate of 1–2 μm per min, stopping at the SiO2 layer at the bottom surface of the wafer. The gold-nanodot arrays were placed on the SiN membrane by first soaking the top structure wafer in BHF to remove the SiO2 layer, and electron-beam lithography (Raith EBPG 5000+ Electron Beam Writer, Raith Nanofabrication, Dortmund, Germany) was then performed to pattern the gold nanodots on the suspended SiN membrane. To separate out each individual top structure from the processed wafer, another run of the reactive ion-etching (RIE) process was used as a dicing step. The bottom structure of the sensor, which consists of a reflective Si surface and a hollow cylindrical cavity, was fabricated in another Si wafer. A carefully controlled Bosch process was used to create 7 μm-deep cylindrical trenches with a smooth bottom surface (AFM-measured peak-to-peak roughness: 1.3 nm) to serve as the mirror in the sensor cavity. Finally, the top and bottom structures were aligned under a microscope and bonded together using a medical grade epoxy. All sensors were pre-characterized in a pressurized chamber after fabrication and devices with high SNR values (415 dB) were selected for implantation.

2.7.2 Surgical Procedures for in vivo testing

Sensor Attachment to Delivery Platforms: The nanophotonic IOP sensors were attached to either an IOL or to silicone haptics for delivery and placement into the eye. A cavity of approximately 1 mm in diameter and 0.5 mm in depth was mechanically cut into the IOL. Sensors were placed into this

cavity using medical grade UV adhesive (Loctite 3321, Loctite Corp. Rocky Hill, CT, USA) with the deformable membrane side facing outwards from the IOL cavity. The silicone haptics were manually fabricated from medical grade silicone membrane (125 μm thick) (BioPlexus, Ventura, CA, USA) into a barbell shape approximately 2.5 mm in width and 12.5 mm in length. The sensor was attached to the silicone haptics with medical grade silicone adhesive (Med-1000 RTV silicone adhesive, Nusil Technology, Carpenteria, CA, USA). The sensor and haptics were sterilized using 70% alcohol for 15 minutes and then rinsed with sterile 0.9% saline solution prior to use.

Animals: The New Zealand White rabbits (females 2.5-3.2 kg in weight) were obtained from Western Oregon Rabbit Company (Philomath, OR. USA) and housed in an USDA approved facility at UCSF. The use of animals in this study adhered to the Association for Research in Vision & Ophthalmology Statement for the Use of Animals in Ophthalmic and Vision Research. The experimental protocol in this study has been approved by the Institutional Animal Care and Use Committee (IACUC) of the University of California San Francisco. Rabbits were used in an observational study of *in vivo* sensor performance. The results reported here were broadly representative of the 5 sensors implanted and studied up to 4.5 months. No statistical analysis was performed to compare results from different rabbits. No randomization of animals was performed and no masking of the investigators was utilized.

Implantation of Sensors Attached to Intraocular Lenses: Dilating eyedrops (phenephrine 2.5% and cyclopentolate 1%) were applied to the eye intended for surgery once every 5 minutes for a total of three times. Ketamine (35mg/kg) and xylazine (3mg/kg) were then intramuscularly injected. The animal was transferred to the surgical table and placed under isoflurane anesthesia. The heart rate, breathing rate, core temperature, and O_2 saturation were monitored throughout surgery. Topical proparacaine hydrochloride (0.5%) was applied to the eye, followed by 1 drop of 5% povidone-iodine. A 1-mm sideport incision was made followed by the injection of an ophthalmic viscosurgical device (OVD) (Provisc, Alcon, Fort Worth, TX, USA) into the anterior chamber. A 3.0-mm primary corneal incision was created, and capsulorhexis forceps were introduced to perform a 4.5-mm capsulotomy. Following hydrodissection, the native lens was subjected to phacoemulsification (Alcon Infiniti Phacoemulsification System, Alcon, Fort Worth, TX, USA), and irrigation and aspiration were performed for cortical cleanup using 0.9% saline with 1:1000 epinephrine and 10

IU/mL heparin. A one-piece acrylic IOL (Acrysof SN60 WF, Alcon, Fort Worth, TX, USA) with a sensor attached was inserted into the recommended IOL cartridge and loaded into the IOL inserter according to the manufacturer's instructions. The folded IOL with the sensor was then inserted into the capsular bag, and the IOL position was adjusted as needed. The OVD was then removed by irrigation, and one 10-0 suture was placed to close the primary incision. Cefazolin antibiotic was applied sub-conjunctivally and a neomyxin / dexamethasone ointment was applied to the eye. The rabbit was then removed from anesthesia and allowed to revive before being returned to the housing area.

Implantation of Sensors with Silicone Haptics: The pre-surgical preparation, anesthesia, and monitoring of rabbits was as described above for animals with IOL / sensor implantation. A 2.8-mm corneal incision was made and OVD injected into the anterior chamber. The sensor with silicone haptics was folded onto itself, grasped with a pair of forceps, and introduced through the corneal incision. The haptics were allowed to unfold spontaneously and positioned into the iridocorneal angles for fixation. The OVD was then removed by irrigation, and a 10-0 suture was placed to close the incision as needed. A subconjunctival antibiotic and an antibiotic / steroid ointment were applied as described above.

2.7.3 Experimental setup and calibration for aberration study

The setup enabled consecutive measurements of optical spectra and aberrations by incorporating two different systems: (1) a commercially available NIR spectrometer (Maya 2000; Ocean Optics, Dunedin, Florida) operating at 800 to 1100 nm with a broadband (400 to 1300 nm) halogen fiber-optic light source (OSL1; Thorlabs, Newton, New Jersey) for spectral resonance measurements and (2) a 150-µm-pitch CMOS-based SH sensor (WFS20-5C; Thorlabs, Newton, New Jersey) with a 940-nm laser diode (LP940-SF30; Thorlabs, Newton, New Jersey) for aberration characterization. Both the broadband light and the 940-nm laser were collimated and aligned coaxially to form focal points identical in size and location on the implant under measurement. The two distinct measurements, namely spectral and aberration, shared the same optical path, including an achromatic (690 to 1200 nm) quarter-wave plate (AQWP05M-980; Thorlabs, Newton, New Jersey), a 0.55-NA objective lens (50× M PLAN APO; Mitutoyo, Japan), the cornea of the ex vivo rabbit eye, the

anterior chamber, and the active area of the sensor. A 0.55-NA objective provided a focal spot size that matched the active area of the sensor. Therefore, we were able to obtain the aberration data only from the active area of the sensor and the corneal area right above it. Before use, the integrated SH sensor was pre-characterized to remove any aberrations that could originate from the objective lens and other optical components in the experimental setup; this was done using a polished silicon chip immersed in water as a reflective surface for double-pass calibration. After calibration, the experimental setup showed an accuracy of 9.317 nm or approximately $\lambda/101$, which is very close to the accuracy of $\lambda/100$ specified by the manufacturer.

2.8 Bibliography

[1] H. A. Quigley HA and A. T. Broman, Br. J. Ophthalmol. 2006, 90, 262–267.

[2] Y. C. Tham et al., Ophthalmol. 2014, 121, 2081–2090.

[3] A. T. Broman et al., Investig. Ophthalmol. Vis. Sci. 2008, 49, 66–76.

[4] M. Malihi et al., Ophthalmol. 2014, 121, 134–141.

[5] D. Peters et al., Am. J. Ophthalmol. 2013, 156, 724–730.

[6] D. Peters et al., Acta Ophthalmol. 2014, 92, 421–425.

[7] H. A. Quigley, Lancet 2011, 377, 1367–1377.

[8] B. Bengtsson B et al., Ophthalmology 2007, 114, 205–209.

[9] C. G. De Moraes CG et al., Arch. Ophthalmol. 2011, 129, 562–568.

[10] A. Heijl et al., Arch. Ophthalmol. 2002, 120, 1268–1279.

[11] A. M. Bhorade et al., Ophthalmology 2009, 116, 717–724.

[12] S. M. Drance SM, Tran. Can. Ophthalmol. Soc. 1960, 23, 131–140.

[13] J. B. Jonas et al., Am. J. Ophthalmol. 2005, 139, 1136–1137.

[14] Y. Kitazawa, T. Horie, Am. J. Ophthalmol. 1975, 79, 557–566.

[15] M. C. Leidl et al, Br. J. Ophthalmol. 2014, 98, 1315–1319.

[16] B. Mottet et al., Investig. Ophthalmol. Vis. Sci. 2012, 53, 8186–8191.

[17] S. De Smedt et al., J. Glaucoma 2012, 21, 539–544.

[18] J. H. Liu et al., Investig. Ophthalmol. Vis. Sci. 2003, 44, 4439–4442

[19] J. H. Liu et al., Investig. Ophthalmol.Vis. Sci. 2003, 44, 1586–1590.

[20] N. Ni et al., J. Glaucoma 2012, 21, 590–595.

[21] M. Pekmezci et al., Arch. Ophthalmol. 2011, 129, 276–281.

[22] E. Hughes et al., J. Glaucoma 2003, 12, 232–236.

[23] W.-H. Wang et al., Investig. Ophthalmol.Vis. Sci. 2005, 46, 4617–4621.

[24] J. Danias et al., Investig. Ophthalmol.Vis. Sci. 2003, 44, 1138–1141.

[25] K. Zhang et al., Nat. Rev. Drug Discov. 2012, 11, 541–559.

[26] A. D. Huberman et al., Nature 2015, 527, 456–457.

[27] E. C. Johnson et al., Investig. Ophthalmol.Vis. Sci. 2007, 48, 3161–3177.

[28] L. Guo et al., Investig. Ophthalmol. Vis. Sci. 2005, 46, 175–182.

[29] J. Flammer et al., Prog. Retin. Eye Res. 2002, 21, 359–393.

[30] E. Chihara et al., Surv. Ophthalmol. 2008, 53, 203–218.

[31] G.-Z. Chen et al., Sens. Actuators A, Phys. 2013, 203, 112–118.

[32] K. Mansouri, T. Shaarawy, Br. J. Ophthalmol. 2011, 95, 627–629.

[33] C. Faschinger, G. Mossböck, Der Ophthalmologe: Zeitschrift der Deutschen Ophthalmologischen Gesellschaft 2010, 107, 918–922.

[34] M. Leonardi et al., TRANSDUCERS 2003 – Int. Conf. Solid-State Sens. Actuators Microsyst., 8-12 Jun 2003, Boston, MA, USA, 2003, 1043–1046.

[35] K. Mansouri et al., Arch. Ophthalmol. 2012, 130, 1534–1539.

[36] M. Greene, B. Gilman, Investig. Ophthalmol. Vis. Sci. 1974, 13, 299–302.

[37] M. Leonardi et al., Acta Ophthalmol. 2009, 87, 433–437.

[38] M. Leonardi et al., Investig. Ophthalmol. Vis. Sci. 2004, 45, 3113–3117.

[39] Y.-C. Huang et al., Sensors, 3-6 Nov 2013, Baltimore, MD, USA, 2013, 1–4.

[40] N. M. Farandos et al., Adv. Healthcare Mat. 2015, 4, 792–810.

[41] P. M. Ladage et al., Eye Contact Lens 2004, 5, 7.

[42] M. Imayasu et al., Ophthalmology 1994, 101, 371–388.

[43] D. H. Ren et al., CLAO J. 1999, 25, 81.

[44] A. Koutsonas et al., Investig. Ophthalmol. Vis. Sci. 2015, 56, 1063–1069.

[45] A. Todani et al., Investig. Ophthalmol. Vis. Sci. 2011, 52, 9573–9580.

[46] K. C. Katuri et al., IEEE Sens. J. 2008, 8, 12–19.

[47] C. C. Collins, IEEE Trans. Biomed. Eng. 1967, 14, 74–83.

[48] C.-I. Jang et al., App. Phys. Lett. 2016, 108, 103701.

[49] Ç .Varel et al., J. Micromech. Microeng. 2014, 24, 045012.

[50] E. Y. Chow et al., IEEE Trans. Biomed. Circuits Syst. 2010, 4, 340–349.

[51] N. Xue et al., J. Microelectromech. Syst. 2012, 21, 1338–1346.

[52] K. Stangel et al., IEEE J. Solid-State Circuits 2001, 36, 1094–1100.

[53] L. Rosengren et al., Sens. Actuators A: Phys. 1994, 43, 55–58.

[54] M. H. Ouda et al., IEEE Trans. Microw. Theory Tech. 2013, 61, 2177–2184.

[55] A. Donida et al., IEEE Trans. Biomed. Circuits Syst. 2015, 9, 777–789.

[56] P.-J. Chen et al., J. Microelectromech. Syst. 2008, 17, 1342–1351.

[57] G. Chitnis et al., IEEE Trans. Biomed. Eng. 2013, 60, 250–256.

[58] S. Melki et al., JAMA Ophthalmology 2014, 132, 1221–1225.

[59] S. M. Ittoop et al., Adv. Therapy 2016, 33, 1679–1690.

[60] N. Sharma et al., J. Cataract Refract. Surg. 1999, 25, 1585–1588.

[61] E. J. Hollick et al., Ophthalmology 1999, 106, 49–55.

[62] G. Hill et al., Sens. Actuators A 2007, 138, 52–62.

[63] G. Chen et al., 2011 IEEE Intl. Solid-State Circuits Conf. 20-24 Feb 2011, San Francisco, CA, USA, 2011, 310-312.

[64] M. H. Ouda et al., IEEE Trans. Microw. Theory Tech. 2013, 61, 2177–2184.

[65] D. A. Miller, IEEE J. Quantum Electron. 1981, 17, 306–311.

[66] G. Hernández, Fabry-Perot Interferometers. Cambridge University Press 1988, vol. 3. [67] J. Santos et al., App. Opt. 1992, 31, 7361–7366.

[68] W. P. Eaton et al., Tech. Proc. Intl. Conf. Model. Simul. Microsyst., 19–21 Apr 1999, San Juan, Puerto Rico, USA, 1999, 640–643.

[69] P. B. Johnson, R.-W. Christy, Optical constants of the noble metals. Phys. Rev. B 1972, 6, 4370.

[70] B. C. Platt and R. Shack, J. Refract. Surg. 2001, 17(5), S573–S577.

[71] P. M. Prieto et al., J. Opt. Soc. Am. A 2000, 17(8), 1388–1398.

[72] J. Liang et al., J. Opt. Soc. Am. A 1994, 11(7), 1949–1957.

[73] L. N. Thibos and H. Xin, Optom. Vision Sci. 1999, 76(12), 817–825.

[74] A. Guirao et al., Arch. Ophthalmol. 2002, 120(9), 1143–1151.

[75] S. Marcos, B. Sergio, and J. A. Ignacio, J. Refract. Surg. 2005, 21(3), 223–235.

[76] F. Taketani et al., J. Cataract Refractive Surg. 2004, 30(10), 2158–2162.

[77] K. H. Kim et al., IEEE Sens. J. 2017, 17(22), 7394–7404.

[78] L. N. Thibos et al., J. Refractive Surg. 2002, 18(5), S652–S660.

[79] L. Chen et al., Clin. Exp. Optom. 2014, 97(6), 534–539.

[80] M. C. Teich and B. Saleh, Fundamentals of Photonics, 1991, 22nd ed., Wiley Interscience, New York.

[81] A. Nazarov et al., J. Biomed. Opt. 2017, 22(4), 047001.

[82] J. Liu and C. J. Roberts, J. Cataract Refractive Surg. 2005, 31(1), 146–155.

[83] J. L. Wiggs, L. R. Pasquale, Hum. Mol. Genet. 2017, 26(R1), R21–R27.

[84] J. O. Lee et al., Microsyst. Nanoeng. 2017, 3(1), 1-9.

[85] S. J. Han et al., J. Biomed. Opt. 2018, 23(4), 047002.

Chapter 3

NANOPHOTONIC APPLICATION TO ANGLE-AND-POLARIZATION INDEPENDENT STRAIN/PRESSURE SENSING

3.1 Introduction to plasmonics

Plasmonics is a study of interactions of light and collective motions of conduction electrons present in metals (plasmons) [1]. At optical frequencies, light incident at the interface of metals and dielectrics creates localized electric field that excites plasmon at the surface of metals, which we call 'surface plasmons (SPs)'. There are two different categories of SPs. The first category is called surface plasmon polaritons (SPPs), which propagate along the metal-dielectric interface (Figure 3.1.1a) [2]. SPPs are bound states of electromagnetic waves that are excited by momentum matching coupling techniques using a prism [3], a blazed metal grating [4], or an array of holes in a metal film [5]. Another category of SPs is called localized surface plasmons (LSPs), which are localized oscillations of electromagnetic fields at the metal-dielectric interface (Figure 3.1.1b). LSPs can be excited on isolated metal particles [6,7] or an array of metal particles [8]. Due to its nature not requiring momentum matching, LSPs have been widely applied to areas such as photovoltaics [9-11], LSP resonance spectroscopy [6,7,12,13], and biosensors [14-17]. In these application areas, LSP performance was optimized by engineering the dimensions of plasmonic arrays such as periodicity, size, height, or geometry of plasmonic nanoparticles.

All these engineering techniques aim to control the SP modes by changing the refractive index (RI) profiles perceived by the electromagnetic waves at the metal-dielectric interface. Electromagnetic modes of lower frequencies (longer wavelengths) prefer to be localized in high RI regions, whereas

the modes of higher frequencies (shorter wavelengths) prefer to be localized in low RI regions [18]. Therefore, by optimizing the local RI profile of the plasmonic array, a SP mode of a desired performance at a specific frequency can be enabled.

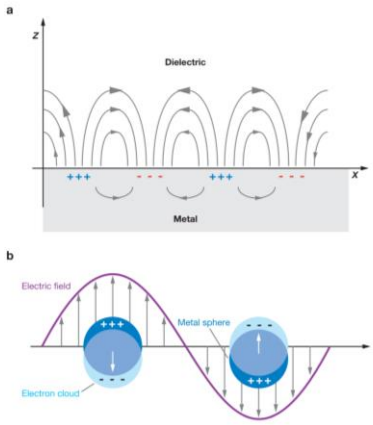

Figure 3.1.1 Illustrations of (a) surface plasmon polariton (SPP) and (b) localized surface plasmon (LSP) [2]. Reprinted with permission from the Royal Society of Chemistry.

3.2 Challenges for plasmonic sensors

Most plasmonic nanostructures are either planar or 2-dimensionally (2D) periodic arrays at subwavelength scales and thus provide a constant value or variation in the in- (*xy*) plane RI ($n_{sp}(x,y)$) profile. Such nanostructures mostly support in-plane SPs whose resonance is angle-and-polarization sensitive [19-21]. Out-of-plane SP was demonstrated by embedding 2D plasmonic nanostructures in a polyurethane matrix and enabled impressively narrow sub-radiant resonances, however, they are angle-and-polarization sensitive [22]. Perfect absorbers [23–26] form the largest category and serve as rare examples of 2D periodic plasmonic arrays that can be nonetheless optimized to show an angle independent absorption peak location under transverse-electric (TE) polarization. However, a significant deviation in the absorption peak wavelength at a greater incident angle is inevitable under transverse-magnetic (TM) polarization in such arrays [27], except for those involving ultra-deep subwavelength-scale absorption layers that are about $\lambda/100$ in thickness [26,28,29]. In addition, perfect absorbers are not suitable for optomechanical applications, which form a vast category of medical implants and wearable devices since the mirror layer becomes fragile under mechanical stress.

3.3 Plasmonic refractive index (RI) gradient and normal-to-plane surface plasmon mode

As discussed in 3.2, the biggest challenge of plasmonic sensors is that LSP resonances are incredibly sensitive to the incident angle and polarization of light. Therefore, plasmonic sensors have been limited to applications in which optical-bench alignment or a microscope can be provided. In addition, precise optical alignment requires a trained technician. For this reason, although the era of optics and photonics in healthcare and biomedicine has already arrived, the application of plasmonic sensing techniques to these fields has remained challenging, especially for medical implants [14-16,30,31] and wearable devices [32-34] that often involve live, moving objects and require easy measurements that can be performed by anyone and at any place.

At a metal-dielectric interface spanning in the *xy* plane, we can engineer the RI profiles in 3 perpendicular axes- *x, y, z*, when the scale of RI variation along the *z* axis is comparable to or smaller than the wavelength of light. Therefore, an RI variation along the normal-to-plane (*z*) axis may be as powerful as an in-plane (*xy*) RI variation for plasmonic resonance engineering. We could optimize an RI profile of a system in 3 dimensions (3D) and realize a plasmonic resonance that is the least sensitive to incident electric field orientation. How do we optimize the 3D RI profile for alignment-free (angle-and-polarization independent) plasmonic systems? Nature has presented her solution in dielectric systems to this deep-rooted problem of plasmonics. Extensive studies on the corneas of diverse moth and butterfly species have revealed their anti-reflective property over a wide range of incident angles, which greatly improves their vision [35]. Wide-angle transmission of light is enabled by a gradual change in the effective RI along the normal-to-plane axis to the cornea ($n_{eff}(z)$). The subwavelength protuberances on the corneal surface results in a gradual increase of $n_{eff}(z)$ from top ($n_{eff}(z) = 0$) to bottom ($n_{eff}(z) = 1.52$) of the structures and therefore creates a RI gradient profile that makes the surface less angle sensitive [36,37]. Implementation of such wide-angle anti-reflective geometry has brought significant improvements in device performance for diverse applications, especially in optics [38], photovoltaics [39–41], imaging [42], and medical sensors [16]. Nevertheless, the principle of normal-to-plane RI engineering has rarely been implemented for improvement of LSP resonance performance.

In this chapter, we apply the RI gradient principle to the normal-to-plane axis of a periodic plasmonic array on a rigid substrate and realize a ‘normal-to-plane’ LSP mode that is angle-and-polarization

independent. Figure 3.3.1a is a photograph of the Hypolimnas salmacis [43] a species in the Nymphalidae family, which is known to possess large-to-full size (class II and III) protuberances on the corneas [44]. The scanning-electron microscope (SEM) image in Figure 3.3.1b shows the pseudo-hexagonal array of protuberances made of chitin on the corneal surface of the species. The array introduces an RI gradient, which is the derivative of n_{eff} along the axis normal to the plane of periodicity ($|dn_{eff}/dz|$). The RI gradient profile enables wide-angle transmission of light, thereby greatly improving vision of the species (Figure 3.3.1c) [36,37].

The biggest difference between the RI gradients realized by dielectrics and metals is that LSP resonances come into play when the array is made of metals. Therefore, an optimized 'plasmonic RI gradient' can create a LSP resonance peak or dip that is angle-and-polarization insensitive instead of broadband angle-independent spectra that are observed in dielectric RI gradient arrays. Figure 3.3.1d shows the plasmonic RI gradient array that implemented periodic subwavelength gold paraboloids. The paraboloidal shape of the plasmonic RI gradient array is inspired by the geometry of protuberances on the butterfly corneas. Unlike its dielectric counterparts, the plasmonic RI gradient array supports a 'normal-to-plane' LSP mode, which is a super-radiant LSP mode that shows a peak and can be excited and detected independently of incident angle or polarization of light.

The plasmonic RI gradient array was fabricated following the steps 1-4 shown in Figure 3.3.1e. For steps 1-3, a hexagonal array of gold conical frustums is produced by electron-beam lithography (EBL), electron-beam evaporation, and metal lift-off. In step 4, the conical frustums are treated with focused-ion beam (FIB) milling, which results in the parabolic shape that creates an optimal $|dn_{eff}/dz|$ profile that supports a normal-to-plane LSP mode. For the angle-and-polarization independent opto-mechanical sensing application, polydimethylsiloxane (PDMS) membranes implemented with the plasmonic RI gradient array were fabricated through the same processes followed by two additional steps 5 and 6 (see 3.7.1 Sample fabrication).

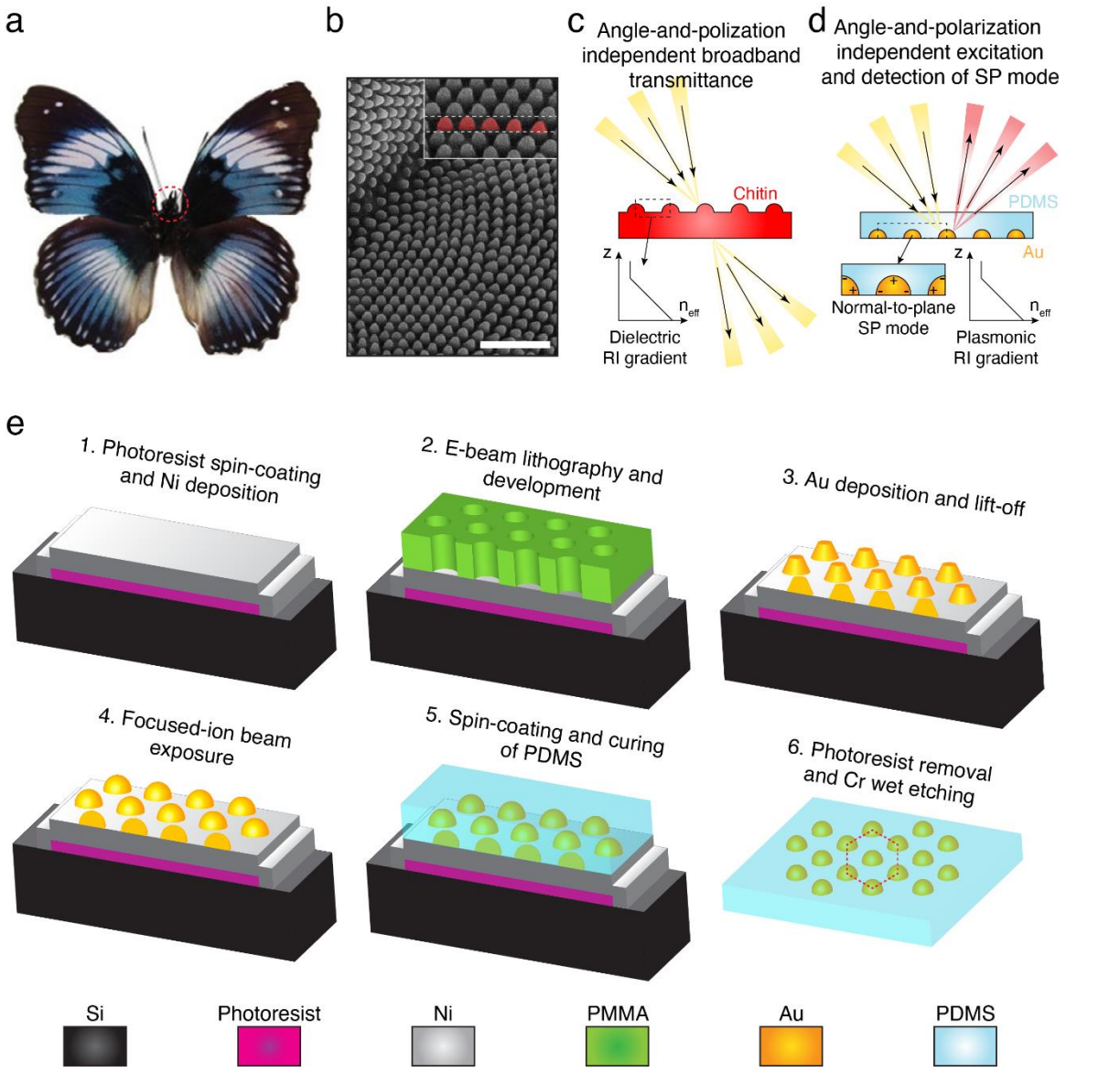

Figure 3.3.1 Concept of the plasmonic RI gradient array (a) Photograph of the *Hypolimnas salmacis*. (b) SEM image of the class II protuberances on the corneal surface of the *Hypolimnas salmacis*. Scale bar 1.5 μm. (c) The subwavelength protuberances on the cornea introduce an RI gradient on the surface that is anti-reflective at wide angles. (d) The plasmonic RI gradient is realized by gold paraboloids that mimic the geometry and principle of the protuberances on the butterfly corneas. (e) Fabrication processes of the plasmonic RI gradient array (steps 1-4) and silicone membranes with an embedded plasmonic RI gradient array (steps 5-6) for opto-mechanical application.

First, we show the relationship between the plasmonic RI gradient and angle independency of super radiant SP modes under TM polarization. We focus our discussion on TM polarization because angle-dependent behaviors in the majority of plasmonic systems are observed under TM polarization due to the dependence of the incident electric field orientation on the incident angle. In Figure 3.3.2a, we plot n_{eff} versus the distance from the metal-dielectric interface *z* and compare the different plasmonic RI profiles realized by arrays of gold disks, gold rounded disks, gold hemi-ellipsoids, and gold paraboloids. All the arrays have the same lattice constant (a = 300 nm), diameter (d = 240 nm), and height (h = 100 nm). The disk array shows a constant $n_{eff}(z)$ profile along the z axis. Therefore, it does not provide a RI gradient and we call this array a non-RI gradient array. The rounded disk array provides a partially RI gradient profile on the upper half of the structure where rounded edges exist and does not provide a RI gradient at the bottom half of the structure. Both the hemi-ellipsoid and paraboloid arrays provide a RI gradient profile from the bottom to top of the structure ($0 \leq z \leq$ h). However, the difference exists in the shape of the RI gradient profiles. The paraboloid array provides the closest-to-linear plasmonic RI profile, which in other words, results in the most uniform RI gradient ($|dn_{eff}/dz| \sim$ constant) and the smallest standard deviation within $0 \leq z \leq$ h ($\sigma(|dn_{eff}/dz|) \sim 0$).

The super-radiant LSP mode of each array at an angle of incidence $\theta = 30°$ is shown in Figure 3.3.2b. In order to show how the LSP modes resonate around the structures, dipole moment orientations (green arrows) and angles φ were calculated and overlaid on the E*z* and E*x* profiles on the surface of each structure, which were projected to the *xy* (top rows) and *xz* (bottom rows) planes. Dipole moment $\vec{p}$ was calculated based on Equation 3.3.1, where q is the charge present on the metal-insulator interface, ε_0 is vacuum permittivity, and $\vec{E}$ is electric field, which was obtained from the *xz* (TM polarization) or *yz* (TE polarization) planes in FDTD simulations. Dipole moment angle φ is defined as the angle between the normal-to-plane (*z*-) axis and $\vec{p}$, which was calculated based on Equation 3.3.2, where $\vec{d}$ is the position vector of q, and C is a closed loop along the metal-insulator interface.

$$\nabla \cdot \vec{E} = \frac{q}{\epsilon_0} \qquad \text{Equation 3.3.1}$$

$$\vec{p} = \oint_C q\vec{d} = |\vec{p}|\angle(90° - \varphi)$$ Equation 3.3.2

With a more linear plasmonic RI profile along the normal-to-plane axis, φ of E*z* and E*x* LSP modes become close to 0º. We name the SP mode of the paraboloid array because the 'normal-to-plane' mode since both of its E*z* and E*x* dipole moments are oriented normal to the plane of periodicity.

We used two different methods- finite-difference time-domain (FDTD) method and transfer matrix method (TMM, see 3.7.2 Computational analysis)-to obtain the reflection peak shifts (|Δλ|) from θ = 30° to 60° of the super-radiant LSP modes supported by disk, rounded disk, hemi-ellipsoid, and paraboloid arrays. While FDTD method is suitable for plasmonic resonance analyses, TMM is optimized for analyzing stratified media and therefore has been widely used in studies on dielectric RI gradient structures, i.e., butterfly corneas [37]. The left axis of Figure 3.3.2c shows the relationship between plasmonic RI gradient uniformity ($\sigma(|dn_{eff}/dz|)$) and |Δλ|. A more uniform plasmonic RI gradient (a smaller $\sigma(|dn_{eff}/dz|)$) results in a smaller |Δλ|. In addition, |Δλ| obtained from both FDTD (blue circle markers) and TMM (blue triangle markers) analyses are in good agreement, which proves that angle-dependent or -independent behaviors of the super-radiant LSP modes are the result of the plasmonic RI gradient. φ shown in Figure 3.3.2b were plotted in Figure 3.3.2c (right axis) and shows a strong correlation to |Δλ| (red square and diamond markers), which indicates the close relationship between φ and a plasmonic RI gradient profile. Therefore, the paraboloid array that provides the most uniform RI gradient supports the normal-to-plane LSP mode that resonates normal to the plane of periodicity (φ ~ 0º) and is the most angle independent. Likewise, the same paraboloid geometry made of biological dielectric substance called chitin was proven to be the most angle independent [37].

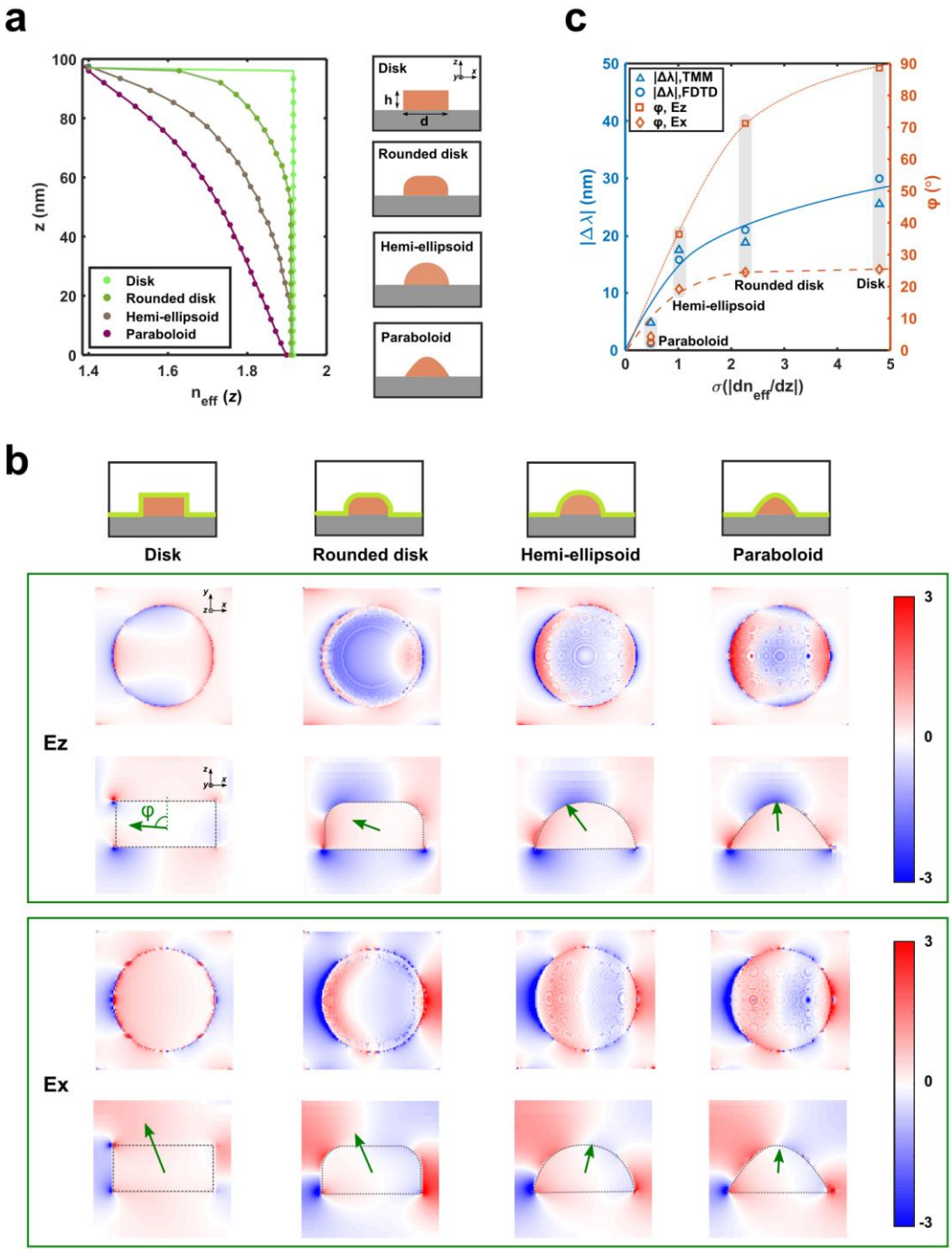

Figure 3.3.2 Principle of the plasmonic RI gradient (a) FDTD-based calculation of n_{eff} perceived by 620 nm wavelength for the hexagonal arrays of disks, rounded disks, hemi-ellipsoids, and paraboloids along the normal-to-plane (z) axis. Dimensions of all arrays are set to a = 300 nm, d = 220 nm, h = 100 nm.

(b) 2D (*x*-*y* plane) projection images of $E_{\tilde{z}}$ (first row) and E_x (third row) on the 3D surfaces and 2D (*x*-$\tilde{z}$ plane) images of $E_{\tilde{z}}$ (second row) and E_x (fourth row) at $\theta = 30°$ at the peak wavelengths of disk, rounded disk, hemi-ellipsoid, and paraboloid arrays. φ were overlaid on the 2D (*x*-$\tilde{z}$ plane) images of $E_{\tilde{z}}$ (second row) and E_x (fourth row). (c) $|\Delta\lambda|$ from $\theta = 30°$ to 60° (left axis) calculated using TMM (triangle) and FDTD (circle) analyses and φ (right axis) of $E_{\tilde{z}}$ (square) and E_x (diamond) modes plotted against $\sigma(|dn_{eff}/d\tilde{z}|)$ for disk, rounded disk, hemi-ellipsoid, and paraboloid arrays.

The paraboloid array also supports a normal-to-plane mode under TE polarization. The normal-to-plane LSP mode under TE polarization is plotted in Figure 3.3.3 and compared to that of TM polarization. The E*y* LSP mode shows a very similar profile to E*x* LSP mode under TM polarization. The E*z* LSP mode shows a very similar profile to E*z* LSP mode under TM polarization. As a result, the angle-independent normal-to-plane LSP resonance peaks in the reflection spectra, originated from these LSP modes that resonate along the normal-to-plane axis, are observed in both TM (Figure 3.3.3c) and TE polarizations (Figure 3.3.3d). Therefore, the normal-to-plane LSP mode is angle-and-polarization independent. Unless stated otherwise, we focus our discussion on TM polarized incident light because angle-dependent behaviors in the majority of plasmonic systems are observed under TM polarization due to the dependence of the incident electric field orientation on θ [27].

In Figure 3.3.4, the plasmonic RI gradient array was experimentally demonstrated and compared with a non-RI gradient (disk) array of the same lattice constant (a = 300 nm), diameter (d = 220 nm), and height (h = 100 nm). Figure 3.3.4a is the SEM images of the fabricated plasmonic RI gradient array, which clearly shows its paraboloidal geometry. On the other hand, Figure 3.3.4b shows the non-RI gradient array of disks with flat-top surfaces and defined upper edges. The reflection spectra of the plasmonic RI gradient and non-RI gradient arrays were calculated using the FDTD method at $0^o \leq \theta \leq 60^o$ (Figures 3.3.4c, e). The angle-independent normal-to-plane peaks are located at λ = 640 nm and 680 nm (Figure 3.3.4c). In Figure 3.3.4d, the dipolar moment was overlaid on the E*z* profile at the normal-to-plane peak wavelength (λ = 640 nm) at θ = 30°, 60°. The dipolar moment is aligned

perpendicular to the *xy* plane throughout $25^{o} \leq \theta \leq 60^{o}$ and therefore results in angle independence of the peak.

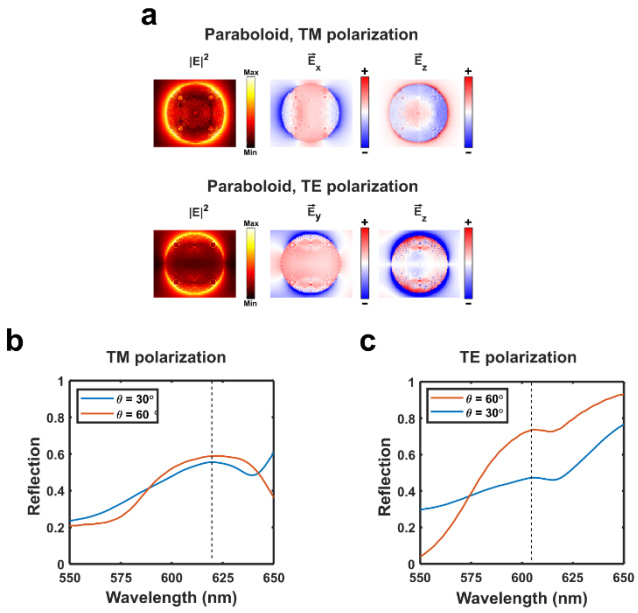

Figure 3.3.3 Polarization-independent normal-to-plane mode. (a) *xy* plane projection images of the normal-to-plane modes formed on the surface of a paraboloid array (a = 300 nm, d = 200 nm, h = 100 nm) under TM (top row) and TE (bottom row) polarizations. (b) Reflection peaks of the normal-to-plane mode at θ = 30°, 60° under TM polarization. (c) Reflection peaks of the normal-to-plane mode at θ = 30°, 60° under TE polarization.

At $\theta < 25^{o}$, the normal-to-plane peak at 640 nm is less prominent since the mode shows much weaker excitation on the apex of the paraboloid due to lack of Ez component in the incident TM polarized light (Figure 3.3.4c). Conversely, the normal-to-plane peak at 680 nm is strongly excited throughout $0^{o} \leq \theta \leq 30^{o}$ and becomes weaker at $\theta > 30^{o}$. Figure 3.3.5 shows the profiles of the normal-to-plane LSP resonance at 640 nm for $\theta = 0^{o}$ (left) and $\theta = 30^{o}$ (right). At $\theta = 30^{o}$, the electric field localization at the apex of the paraboloid is clearly visible, while it is absent at $\theta = 0^{o}$. This explains why the peak is much more prominent at $\theta = 30^{o}$.

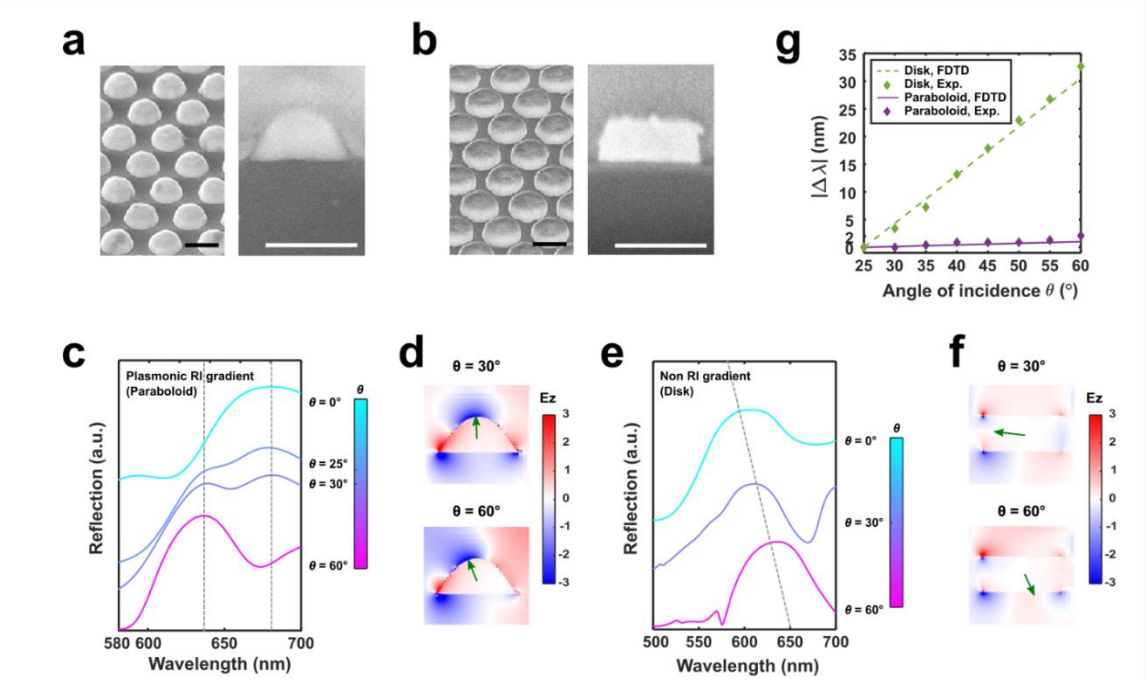

Figure 3.3.4 Experimental verification of the plasmonic RI gradient principle. (a) Isometric (left) and cross-sectional (right) SEM images of the fabricated plasmonic RI gradient array (a = 300 nm, d = 220 nm, h = 100 nm) at a 52° view angle. Scale bars 200 nm. (b) Isometric (left) and cross-sectional (right) SEM images of the fabricated non-RI gradient (disk) array (a = 300 nm, d = 220 nm, h = 100 nm) at a 52° view angle. Scale bars 200 nm. (c) FDTD-calculated reflection of the plasmonic RI gradient array under TM polarization. Both the 640-nm and 680-nm peaks are angle independent at θ = 25° – 60°. (d) $\mathbf{E}_z$ profiles and dipole moments of the 640-nm normal-to-plane mode at θ = 30°, 60°. (e) FDTD-calculated reflection of the non-RI gradient array under TM polarization. The peak is highly angle dependent. (f) $\mathbf{E}_z$ profiles and dipole moments of the SP mode (λ = 600 nm) at θ = 30°, 60°. (g) Comparison of experimental and FDTD-calculated $|\Delta\lambda|$ between the plasmonic RI gradient and non-RI gradient arrays over the range of θ = 25°-60°.

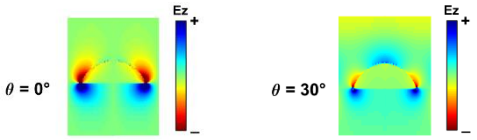

Figure 3.3.5 E_z distributions of the normal-to-plane mode (λ = 640 nm) on the plasmonic RI gradient structure at $\theta = 0°, 30°$ under TM polarization.

Two normal-to-plane peaks observed at θ = 30º exist when the filling factor (f = d/a) and aspect ratio (r = h/d) of the plasmonic RI gradient array are large enough to induce a Fano-type resonance [45] between the adjacent gold paraboloids (Figure 3.3.6a, b). The normal-to-plane peaks can be detected within different ranges of θ depending on f and r of the plasmonic RI gradient array. In addition, the magnitude of |Δλ| and the operation range of θ can be optimized by changing the filling factor ($f = d/a$) and aspect ratio ($r = h/d$) of the plasmonic RI gradient structure. This is because φ of the normal-to-dipolar mode varies depending on f and r.

When f becomes greater, the reflection shows two normal-to-plane mode peaks due to a Fano-type interference [46, 47] induced by a smaller distance between the adjacent gold paraboloids. In this case, the normal-to-plane dipolar modes are detected either at $0° \leq \theta \leq \theta^{*1}$ or $\theta \geq \theta^{*2}$, where θ^{*1} (θ^{*2}) is the upper (lower) limit in the detectable range of the first (second) normal-to-plane peak. θ^{*1} and θ^{*2} depend on f and r. These two normal-to-plane peaks are separated by a Fano-type dip (Figure 3.3.6a). The two normal-to-plane peaks show very similar mode profiles, whereas the Fano-type resonance (dip) shows an asymmetric mode profile (Figure 3.3.6b). The 1st peak becomes less prominent with a greater θ, whereas the 2nd peak becomes more prominent with a greater θ and the reason was discussed previously (Figure 3.3.5).

Figure 3.3.6c shows an example of |Δλ| and θ operation ranges for the two normal-to-plane peaks for r = 0.4, where the 2nd normal-to-plane peak shows at f ≥ 0.5. The left figure shows $|\Delta\lambda(\theta = 0° - \theta^{*1})|$ profiles of the 1st normal-to-plane mode at f > 0.6. f < 0.6 is a out-of-plane mode range, which will be discussed in later in this chapter. A larger f results in a smaller θ^{*1}. The right figure shows $|\Delta\lambda(\theta = \theta^{*2}\text{-}60°)|$ profiles of 2nd normal-to-plane mode at f ≥ 0.5. A larger f results in a smaller θ^{*2}.

Unlike the plasmonic RI gradient array, the non-RI gradient array shows an angle-dependent peak (Figure 3.3.4e). In Figure 3.3.4f, the dipolar moment orientations are overlaid on the Ez profiles of the non-RI gradient array at λ = 600 nm for θ = 30°, 60°. The dipolar moment orientation of the non-RI gradient array is neither perpendicular to the *xy* plane nor consistent throughout $0^{o} \leq \theta \leq 60^{o}$. Due to the absence of a RI gradient, the dipole moment the non-RI gradient array is angle dependent (Figure 3.3.7). In Figure 3.3.4g, both the experimental and simulation results show much improved angle independency of the plasmonic RI gradient array (|Δλ| = 2.1 nm experimentally and |Δλ| = 0.8 nm using FDTD method) compared to the non-RI gradient array (|Δλ| = 32.7 nm experimentally and |Δλ| = 30.5 nm using FDTD method).

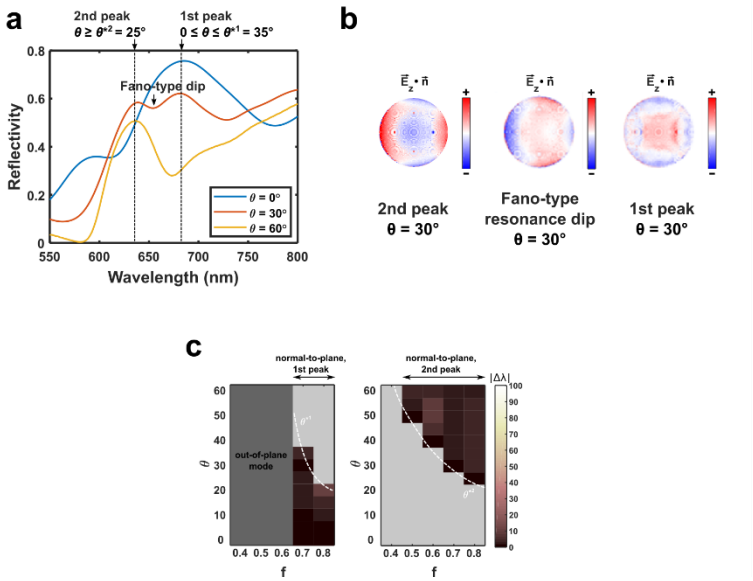

Figure 3.3.6 Two normal-to-plane mode peaks and their detectable ranges. (a) Reflectivity plot of the plasmonic RI gradient array (a = 300 nm, f = 0.7, r = 0.4) at θ = 0°, 30°, 60°. At θ = 30°, the Fano-type resonance shows as a dip between the 1st and 2nd peaks. (b) E_z mode profiles on the plasmonic RI gradient at θ = 30° for λ = 640 nm, 653 nm, and 680 nm, where the 2nd peak, Fano-type resonance dip, 1st peak appears respectively. (c) $|\Delta\lambda(\theta = 0° - \theta^{*1})|$ (left) and $|\Delta\lambda(\theta = \theta^{*2} - 60°)|$ (right) for r = 0.4.

The super-radiant modes of a plasmonic array appear as prominent peaks in the reflection spectra, whereas, the sub-radiant modes of a plasmonic array appear as dips in the reflection spectra [22]. The direct relationship between the near-field modes and far-field spectra of a plasmonic array was thoroughly discussed in [48]. Therefore, when the dipole moment ($\vec{p}$) of a super-radiant mode changes depending on θ because a plasmonic array does not exhibit a RI gradient, it results in a far-field peak shift. Since the dipole moment is calculated based on Equations 3.3.1 and 3.3.2, the change in $\vec{p}$ can be observed via the near-field profiles of the super-radiant modes.

The magnitudes of E_x and E_z at the metal-insulator interface ($|E_{xloc}|^2$ and $|E_{zloc}|^2$) of the plasmonic RI gradient and non-RI gradient arrays under TM polarization at θ = 30°, 60° were obtained using the finite-difference time-domain (FDTD) analysis at the circled locations shown in Figures 3.3.7a, c and plotted in Figures 3.3.7b, d, respectively. Both $|E_{xloc}|^2$ and $|E_{zloc}|^2$ profiles of the plasmonic RI gradient array show an angle-independent enhancement peak at $\lambda \sim 600$ nm, which indicates angle-independency of $\vec{p}$. The red-shift of the far-field peak ($\lambda \sim 640$ nm) shown in Figure 3.3.4c from the near-field peak location is known to result from the damping of the system [48], and this is why $\vec{p}$ at 640 nm, θ = 60° is slightly off from the normal-to-plane axis in Figure 3.3.4d (bottom). On the other hand, the enhancement peak of the non-RI gradient array is angle-dependent, which indicates angle-dependency of $\vec{p}$.

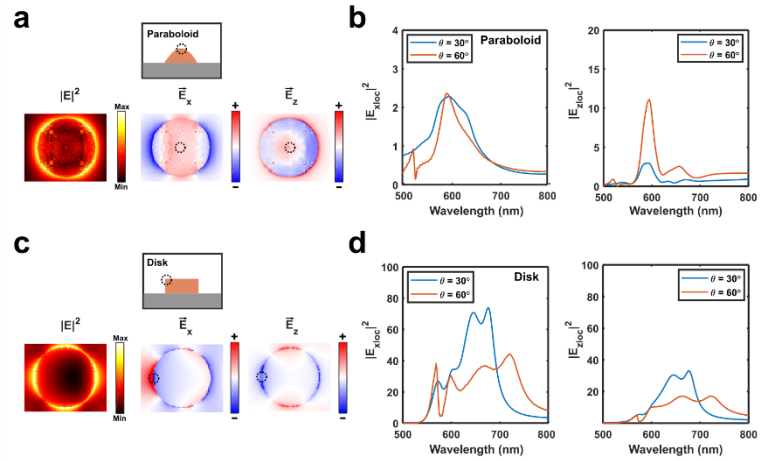

Figure 3.3.7 Comparison of angle-dependent behaviors in paraboloid and disk arrays. (a) Super-radiant mode profiles and (b) near-field enhancement spectra at θ = 30° and 60° computed at the

circled point in (a) of the plasmonic RI gradient (paraboloid) array. (c) Super-radiant mode profiles and (d) near-field enhancement spectra at $\theta = 30°$ and 60° computed at the circled point in (c) of the non-RI gradient (disk) array. (e) Sub-radiant mode profiles and (f) near-field enhancement spectra at $\theta = 30°$ and 60° computed at the circled point in (e) of the plasmonic RI gradient (paraboloid) array. (g) Super-radiant mode profiles and (h) near-field enhancement spectra at $\theta = 30°$ and 60° computed at the circled point in (g) of the non-RI gradient (disk) array.

3.4 Opto-mechanical properties of normal-to-plane mode

In this chapter, we discuss the opto-mechanical properties of the normal-to-plane mode under applied strain. By embedding the plasmonic RI gradient array into a flexible membrane, we realize plasmonics-based angle-and-polarization independent opto-mechanical system operating in the near IR wavelength. Based on the observed opto-mechanical properties, we provide plasmonic RI gradient array design guidelines for angle-and-polarization independent strain or pressure sensing.

There have been numerous studies on implementation of plasmonic arrays into strain sensing as discussed in Chapter 3.2, however, these applications have been limited to a certain θ due to the angle dependency of plasmonic modes [27,49]. Capability of engineering the robustness of the normal-to-plane mode by optimizing f and r makes the plasmonic RI gradient array a great candidate for angle-and-polarization independent opto-mechanical applications such as strain and pressure sensors for use in industry, medical fields, etc. The dimensions of a plasmonic RI gradient array need to meet the following Equation 3.4.1 in order to support a normal-to-plane mode. Failing to meet the condition results in an out-of-plane mode, which makes the array angle-and-polarization dependent.

$$f \times (r + 0.1) \geq 0.34 \qquad \text{Equation 3.4.1}$$

The striking difference between the normal-to-plane and out-of-plane surface modes is the orientation of dipolar moment that surface plasmons form on the gold paraboloids. The normal-to-plane mode shows $\varphi < 30°$, the out-of-plane mode shows $30° \leq \varphi < 90°$, and the in-plane mode shows $\varphi = 90°$. The range of φ for the normal-to-plane modes was defined based on the FDTD analyses at each $0.4 \leq f \leq 0.8$ and $0.3 \leq r \leq 0.7$, which cover the range of gold paraboloid dimensions that can

be fabricated. The transitions between the normal-to-plane and out-of-plane modes can be clearly seen in Figure 3.4.1a, where φ are overlaid on the $|\mathbf{E}|^2$ profiles of SP modes at $\theta = 30°$. The top row ($f = 0.6$) shows the transition occurs at $0.4 < r < 0.5$. The bottom row ($r = 0.4$) shows the transition occurs at $0.6 < f < 0.7$. When φ is plotted against r, the transition is clearly seen as φ of the normal-to-plane mode is much smaller than that of the out-of-plane mode (Figure 3.4.1b). All φ after the transition to the normal-to-plane mode within $0.3 \leq r \leq 0.7$, $0.4 \leq f \leq 0.8$ were calculated to be smaller than 30º. In Figure 3.4.1c, we filled yellow for $\varphi < 30°$ and $30° \leq \varphi < 90°$, respectively, at each f and r, and marked where the transition from the out-of-plane to normal-to-plane mode happens (red dashed line). The normal-to-plane mode is supported when Equation 3.4.1 is met. The transitions observed in Figure 3.4.1 are in good agreement with the provided equation.

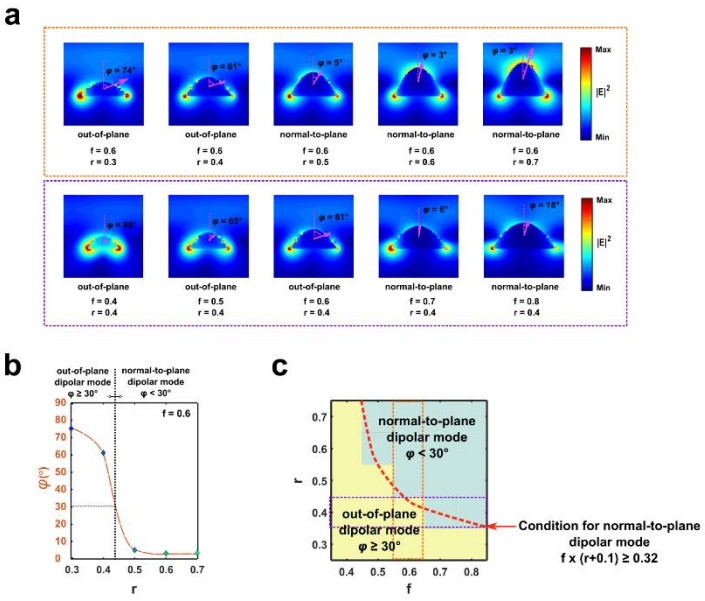

Figure 3.4.1 Transition from the normal-to-plane mode to out-of-plane mode. (a) Dipole moment orientation overlaid on the $|\mathbf{E}|^2$ profiles of SP modes at $\theta = 30°$ for $f = 0.6$ (top row) and $r = 0.4$ (bottom row). (b) φ plotted against r at $f = 0.6$ and $\theta = 30°$, showing an abrupt transition between the out-of-plane and normal-to-plane dipolar modes at $0.4 < r < 0.5$. (c) Transition between the out-of-plane to normal-to-plane dipolar modes happens at $f \times (r + 0.1) \sim 0.34$.

In order to assess the angle-independent performance of the plasmonic RI gradient array, we introduce the term resolution R(ε), which is the smallest difference in the applied strain ε that a plasmonic RI gradient array can detect over a specific range of $\theta_{min} \le \theta \le \theta_{max}$. Mathematically, R(ε) is the standard deviation of errors between the measured strain ε_m and ε. In calculating ε_m, we assume that 1) the ε – Δλ curve at every $\theta_{min} \le \theta \le \theta_{max}$ is known, 2) Δλ is obtained once at an unknown θ within $\theta_{min} \le \theta \le \theta_{max}$, and 3) ε_m is calculated for a total of N trials, which is the ratio of Δλ to the slope of the ε – Δλ curve for a randomly chosen ε at the k-th trial $\Delta\lambda/|d\lambda/d\varepsilon|_k$ (Equation 3.4.2). When an array is more angle-independent, $\left|\frac{d\lambda}{d\varepsilon}\right|$ will be closer between randomly selected θ and result in a smaller $R(\varepsilon)$. With a more angle-dependent array, there will be more variations in $\left|\frac{d\lambda}{d\varepsilon}\right|$ and ε_m between randomly selected θ, which result in a larger $R(\varepsilon)$.

$$R(\varepsilon) = \sigma(\varepsilon_m - \varepsilon) = \sqrt{\frac{1}{N}\sum_{k=1}^{N}|\varepsilon_m(k) - \varepsilon|^2} = \sqrt{\frac{1}{N}\sum_{k=1}^{N}\left|\frac{\Delta\lambda}{\left|\frac{d\lambda}{d\varepsilon}\right|_k} - \varepsilon\right|^2} \qquad \text{Equation 3.4.2}$$

Illustrations for the effect of N on $R(\varepsilon)$ are shown in Figures 3.4.2a-c. Throughout chapters 3.4-3.5, we assume (1) $\Delta\lambda = \frac{1}{2} \times (\Delta\lambda(\theta_{min}) + \Delta\lambda(\theta_{max}))$, (2) $\left|\frac{d\lambda}{d\varepsilon}\right| \propto \theta$, and (3) randomly selected θ are evenly distributed within $\theta_{min} \le \theta \le \theta_{max}$, which results in evenly distributed ε_m, for simplicity of calculation. The green circles indicate $\varepsilon_m(k)$ and pink arrows indicate R(ε). As N increases, R(ε) decreases.

When N = 3, θ is selected to be θ_{min}, $(\theta_{min} + \theta_{max})/2$, and θ_{max}. Therefore, R(ε) can be derived as Equation 3.4.3. All R(ε) shown in the Chapters 3.4 and 3.5 are calculated using this equation.

$$R(\varepsilon) \cong \frac{1}{\sqrt{3}}\sqrt{\left|\frac{\frac{1}{2}\times(\Delta\lambda(\theta_{min})+\Delta\lambda(\theta_{\max}))}{\left|\frac{d\lambda}{d\varepsilon}\right|_{\theta_{min}}} - \varepsilon\right|^2 + \left|\frac{\frac{1}{2}\times(\Delta\lambda(\theta_{min})+\Delta\lambda(\theta_{\max}))}{\left|\frac{d\lambda}{d\varepsilon}\right|_{\theta_{max}}} - \varepsilon\right|^2} \quad (N = 3)$$

Equation 3.4.3

Most importantly, R(ε) is determined by ε-Δλ relations. Figures 3.4.2d-f illustrate exemplary cases 1-3, where Case 1 is perfectly angle independent, Case 2 is slightly angle dependent with a small range of Δλ within $\theta_{min} \le \theta \le \theta_{max}$, and Case 3 is heavily angle dependent with a large range of Δλ. R(ε) in each case for N=2,3,5 is shown in Figure 3.4.2g. In Case 1, R(ε) = 0 regardless of N since it is perfectly angle independent. A smaller Δλ range within $\theta_{min} \le \theta \le \theta_{max}$ as well as larger N improve R(ε), while Δλ plays a more significant role in determining R(ε) than N. Therefore, it is critical that we design an array that shows an angle-independent peak over a broader θ range in order to achieve a high resolution (small R(ε)).

In this experiment, we apply in-plane uniaxial strains along two perpendicular axes to the plasmonic RI gradient array at varied θ. By doing so, we experimentally demonstrate the transition from a normal-to-plane mode to an out-of-plane mode at $f \times (r + 0.1) \sim 0.34$ while calculating R(ε) of the array under each strain. Comparing R(ε) before and after the transition, we show that the normal-to-plane mode is critical for the angle- and polarization-independent performance. The dimensions of the plasmonic RI gradient array used in this experiment were set to a = 300 nm, f = 0.65, and r = 0.5, in which ε = 0.15 is expected to result in $f = \frac{d}{a\times(1+\varepsilon)} = 0.57$ and induce the transition from the normal-to-plane mode ($f \times (r + 0.1) \ge 0.34$) to the out-of-plane mode ($f \times (r + 0.1) < 0.34$).

The plasmonic RI gradient array was embedded in a circular piece of PDMS (4-mm in diameter) and uniaxial strain was applied from ε = 0 to 0.5 at steps of 0.125 along the *x*- and *y*-axes. Figures 3.4.3a, b illustrate the orientations of the TM polarized light source and the plasmonic RI gradient array under strains along the *x*- and *y*-axes (ε_x and ε_y). ε_x (or ε_y) results in the transition of the plasmonic RI gradient array from a hexagonal to a monoclinic lattice whose primitive vector $\boldsymbol{a_1}$ (or $\boldsymbol{a_2}$) is longer than $\boldsymbol{a_2}$ (or $\boldsymbol{a_1}$). Under TM polarization, f is only dependent on ε_x since E//*x* and E⊥*y* (Equation 3.4.4). Under TE polarization, f is heavily dependent on ε_y since E//*y* and E⊥*x*. We focus on TM polarization first and then briefly discuss TE polarization later in the chapter.

$$f_{TM} = \frac{d}{|\boldsymbol{a_1}|} = \frac{d}{a\times(1+\varepsilon_x)} \qquad \text{Equation 3.4.4}$$

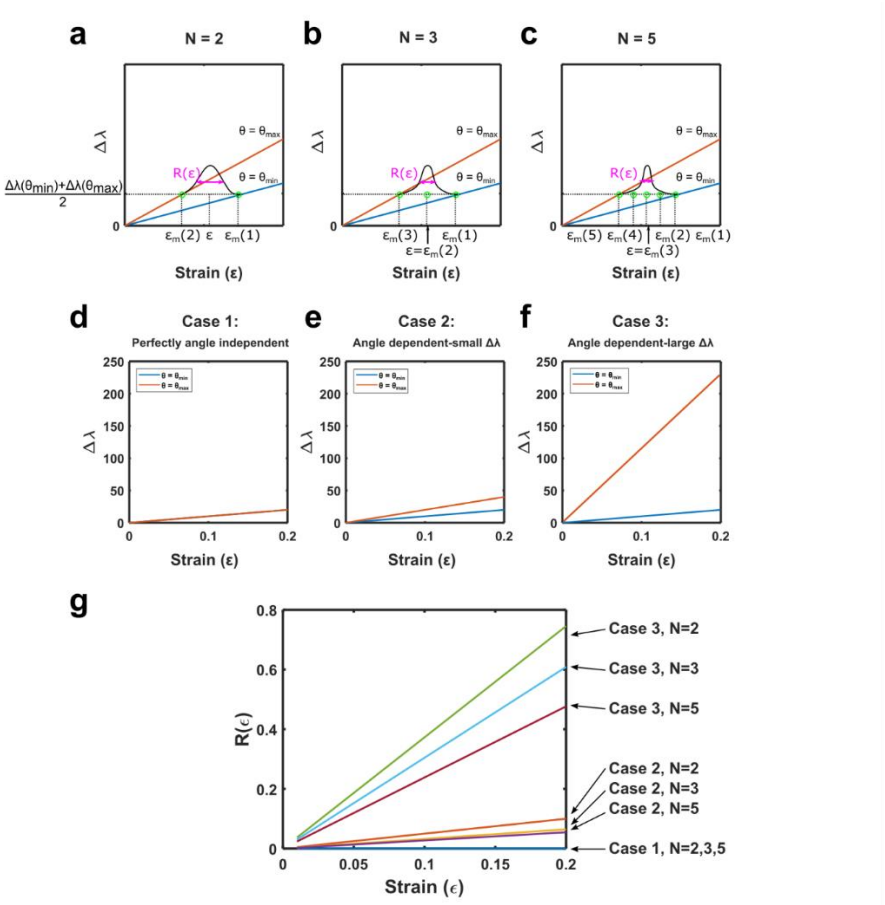

Figure 3.4.2 Illustrations of $R(\varepsilon)$ in a Δλ-ε diagram when (a) N=3, (b) N=4, (c) N=5. Illustrations where an array is (d) perfectly angle-independent, (e) slightly angle dependent with a small Δλ range, (f) heavily angle dependent with a large Δλ range. (g) Comparison of $R(\varepsilon)$ between cases 1-3 where N=2,3,5. A smaller Δλ range and larger N provide a smaller $R(\varepsilon)$.

The strain experiments were performed using the custom-built optical setup that allows reflection measurements at $\theta = 0^0$ and $\theta \geq 25^0$ (see 3.7.3 Optical measurements). Figures 3.4.3c, d show the results from the strain experiments at $\theta = 0^0$ (bottom), 30^0 (top) under ε_x and ε_y, respectively. The solid lines were obtained through polynomial fitting of experimental spectra and marker indicates the peak location of each spectra. The transition from the normal-to-plane mode to out-of-plane mode is observed at $0.125 < \varepsilon_x < 0.25$, which is in good agreement with our calculation based on Equation 3.4.1 that $\varepsilon_x = 0.15$ induces the transition. On the other hand, no transition is observed under ε_y since

f is independent of ε_y (Equation 3.4.4), and therefore the array is angle-independent throughout ε_y = 0 – 0.5. The Ez mode profiles calculated using FDTD confirm the transition; at ε_x = 0, the normal-to-plane mode is supported whereas it is no longer supported at ε_x = 0.5 (Figure 3.4.3e). Throughout ε_y = 0 – 0.5, the normal-to-plane mode is supported (Figure 3.4.3f). In Figure 3.4.3g, R(ε) was calculated based on Equation 3.4.3 using data from the FDTD analyses and experiments at θ = 0°, 30° under ε_x (yellow markers) and ε_y (purple markers). The results obtained from the experiments and the FDTD analyses are in good agreement along with a slight increase in experimental R(ε_x). Under ε_x, there exists an abrupt increase in R(ε) as the transition from the normal-to-plane mode to out-of-plane mode occurs at $0.1 < \varepsilon_x < 0.2$, which results in poor angle-independent performance (R > ε). On the other hand, the normal-to-plane mode is supported throughout ε_y = 0 – 0.5 and enables R(ε) ~ $\frac{1}{3}$ε, which is greater than 5-9x improvement from R(ε) of the out-of-plane mode within ε_x = 0.25 – 0.5 (grey shaded area in Figure 3.4.3g). The strain experiment results shown in Figure 3.4.3 are reproducible (Figure 3.4.4).

A similar trend with the dependence on ε_y is observed under TE polarization; the normal-to-plane mode is supported regardless of ε_x and transitions to the out-of-plane mode under ε_y. Under TM polarization, **E** and x-axis ($\frac{\boldsymbol{a_1}}{|\boldsymbol{a_1}|}$) are on the same plane (Figure 3.4.5a). This results in Equation 3.4.4, which shows a significant dependence of the normal-to-plane mode on ε_x in the effective RI of the normal-to-plane mode under ε_x (Figure 3.4.5a). Under TE polarization, **E** and y-axis ($\frac{\boldsymbol{a_2}-\boldsymbol{a_1}/2}{|\boldsymbol{a_2}-\boldsymbol{a_1}/2|}$) are on the same plane (Figure 3.4.5b). This results in Equation 3.4.5, which shows a significant dependence of the normal-to-plane mode on ε_y. Equation 3.4.4 and Equation 3.4.5 indicate that ε_x, $\varepsilon_y > 0.15$ fail to meet Equation 3.4.1, and therefore induce the transition from the normal-to-plane mode to out-of-plane mode.

$$f_{TE} = \frac{d}{|\boldsymbol{a_2}-\boldsymbol{a_1}/2|} = \frac{d}{a\times(1+\varepsilon_y)} \qquad \text{Equation 3.4.5}$$

In Figure 3.4.5c, d, $|\Delta\lambda| - \varepsilon$ curves under ε_x and ε_y at θ = 0°, 30° are obtained from FDTD analyses and plotted under TM and TE polarizations, respectively. Under TM polarization, there exists an abrupt increase in $|\Delta\lambda|$ at $0.125 < \varepsilon_x < 0.25$ (Figure 3.4.5c). Under TE polarization, there exists an abrupt increase at $0.1 < \varepsilon_y < 0.2$ (Figure 3.4.5d). These results confirm that the transitions from the

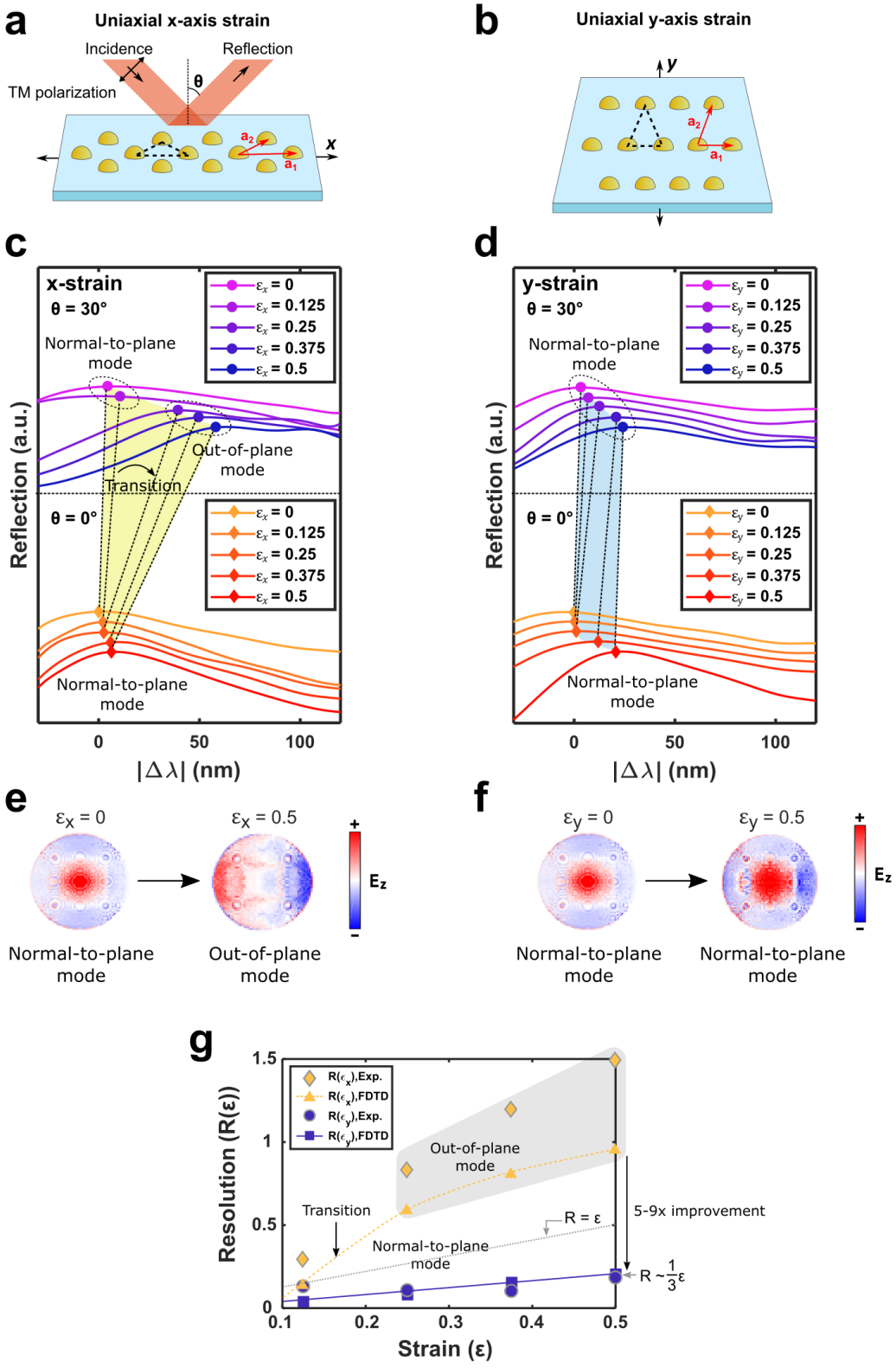
a
Uniaxial x-axis strain
Incidence
Reflection
θ
TM polarization
a2
a1
x
b
Uniaxial y-axis strain
y
a2
a1
c
x-strain
θ = 30°
Normal-to-plane mode
εx = 0
εx = 0.125
εx = 0.25
εx = 0.375
εx = 0.5
Out-of-plane mode
Transition
θ = 0°
Normal-to-plane mode
Reflection (a.u.)
0
50
100
|Δλ| (nm)
d
y-strain
θ = 30°
Normal-to-plane mode
εy = 0
εy = 0.125
εy = 0.25
εy = 0.375
εy = 0.5
θ = 0°
Normal-to-plane mode
Reflection (a.u.)
0
50
100
|Δλ| (nm)
e
εx = 0
εx = 0.5
Ez
+
-
Normal-to-plane mode
Out-of-plane mode
f
εy = 0
εy = 0.5
Ez
+
-
Normal-to-plane mode
Normal-to-plane mode
g
R(εx),Exp.
R(εx),FDTD
R(εy),Exp.
R(εy),FDTD
Out-of-plane mode
Transition
R = ε
5-9x improvement
Normal-to-plane mode
R ~ 1/3 ε
Resolution (R(ε))
1.5
1
0.5
0
0.1
0.2
0.3
0.4
0.5
Strain (ε)

Figure 3.4.3 Opto-mechanical properties of the plasmonic RI gradient array. Illustrations showing the orientations of the plasmonic RI gradient array and applied (a) *x*- and (b) *y*-axis strain. Incident light is TM polarized. (c) Reflection of the plasmonic RI gradient array under the *x*-axis strain (ε_x = 0 – 0.5) at θ = 0°, 30°. (d) Reflection of the plasmonic RI gradient array under the *y*-axis strain (ε_y = 0 – 0.5) at θ = 0°, 30°. (e) $E_{\tilde{z}}$ at ε_x = 0 (left) and ε_x = 0.5 (right), showing a transition from a normal-to-plane mode to an out-of-plane mode. (f) $E_{\tilde{z}}$ at ε_y = 0 (left) and ε_y = 0.5 (right), showing that a normal-to-plane mode is supported throughout ε_y = 0 – 0.5. (g) Resolution profiles of the plasmonic RI gradient array obtained from the FDTD analyses and experiments at θ = 0° – 30° under ε_x (blue markers) and ε_y (yellow markers).

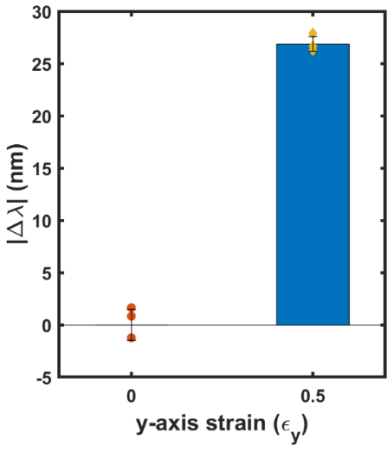

Figure 3.4.4 Comparison of $|\Delta\lambda|$ of the plasmonic RI gradient array under 4 consecutive loading cycles of *y*-axis strain (ε_y = 0 -> 0.5) at θ = 0° under TM polarization.

normal-to-plane mode to out-of-plane mode are happening according to Equation 3.4.1. These results indicate that, in order to achieve angle-and-polarization independent sensing, we should aim for designing a plasmonic RI gradient array with optimized f and r that supports the normal-to-plane mode throughout a targeted ε range based on Equation 3.4.1.

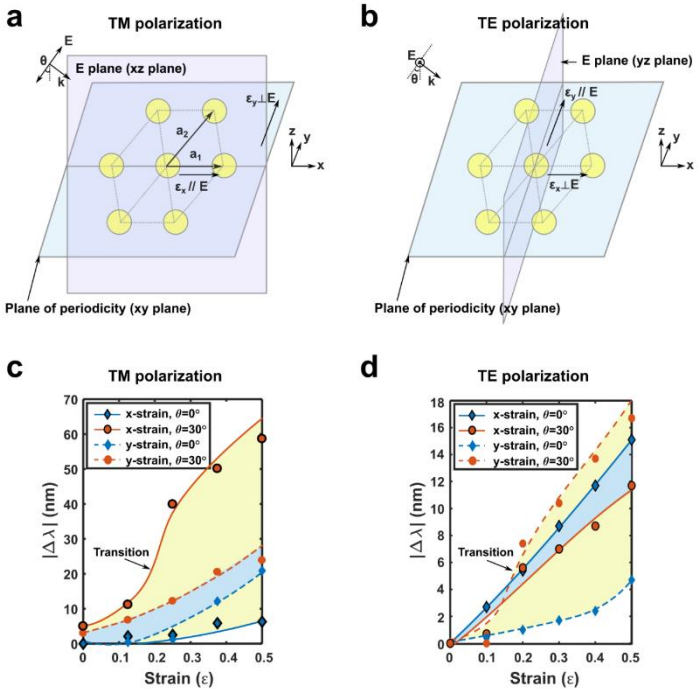

Figure 3.4.5 Illustrations of the orientations of **E**, ε_x, and ε_y under (a) TM and (b) TE polarizations. $|\Delta\lambda| - \varepsilon$ curves of the plasmonic RI gradient array obtained from FDTD analyses under the *x*- and *y*-axis strain ($\varepsilon = 0 - 0.5$) at $\theta = 0°$, 30° under (c) TM and (d) TE polarizations.

3.5 Application of normal-to-plane mode to angle-and-polarization independent strain/pressure sensing

In this chapter, angle-and-polarization independent pressure sensing is demonstrated by implementing the plasmonic RI gradient array on a flexible silicone cavity. The plasmonic RI gradient array was embedded into an 11-μm-thick circular polydimethylsiloxane (PDMS) membrane (diameter = 1.5 mm) and the membrane was assembled to form a hermetically sealed cylindrical cavity (Figures 3.5.1a, b). For the following experiments performed throughout chapter 3.5, we used unpolarized light in order to demonstrate angle-and-polarization independent pressure sensing. Since the membrane experiences radial strain (ε_r) in this cylindrical-shaped mechanical system and the

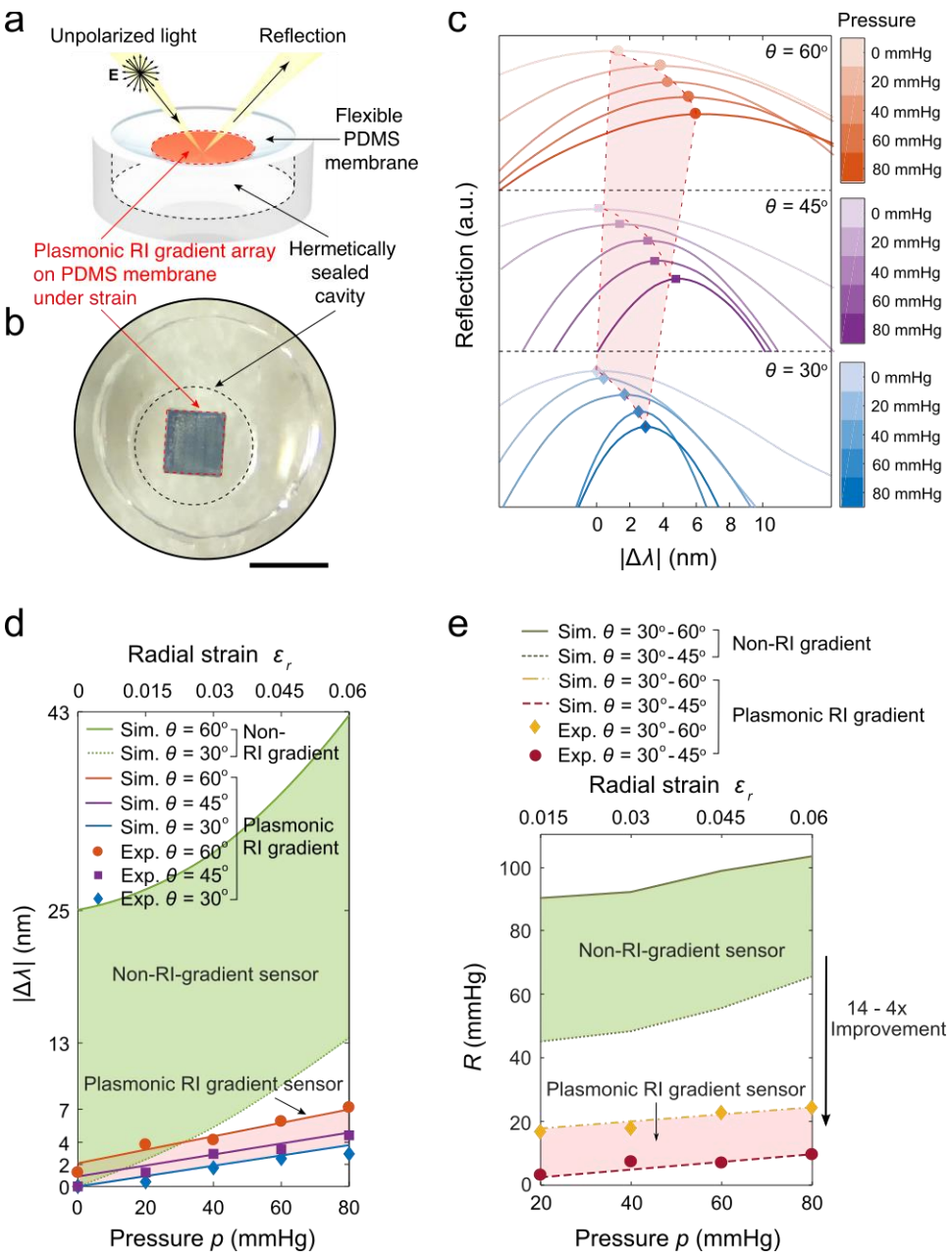

Figure 3.5.1 Application of the plasmonic RI gradient to angle-and-polarization independent pressure sensing. (a) Illustration and (b) photograph of the hermetically sealed silicone cavity with a plasmonic RI gradient array embedded in its membrane. Scale bar 1mm. (c) Far-field spectra of the plasmonic RI gradient sensor under $p = 0 - 80$ mmHg at $\theta = 30°, 45°, 60°$. (d) Comparison between experimental (markers), computational (solid and dashed lines) $|\Delta\lambda|$ of the plasmonic RI gradient sensor at $\theta =$ 30°, 45°, 60° and the non-index-gradient array. Comparison between experimental (markers) and

computational (solid lines) (e) resolution and (f) accuracy of the plasmonic RI gradient sensor at ranges $30° \leq \theta \leq 45°$, $45° \leq \theta \leq 60°$, and $30° \leq \theta \leq 60°$ and non-index-gradient sensor at $30° \leq \theta \leq 60°$.

incident light is unpolarized, where the incident electric field is oriented in all radial directions, the plasmonic RI gradient array follows Equation 3.5.1.

$$f_{unpolarized} = \frac{d}{|\boldsymbol{a_1}|} = \frac{d}{|\boldsymbol{a_2}|} = \frac{d}{a\times(1+\varepsilon_r)} \qquad \text{Equation 3.5.1}$$

In order to achieve the best angle-independent performance by avoiding the transition of the normal-to-plane mode to an out-of-plane, $f_{unpolarized}$ is required to meet Equation 3.4.1. In addition, a larger f exhibits a smaller R Figure 3.5.2. The maximum f that can be achieved in the fabrication process (see 3.7 Methods and materials) is 0.8 due to increasing structural instability of the developed e-beam resist at a greater aspect ratio. Therefore, we set the dimensions of the plasmonic RI gradient array to a = 300 nm, f = 0.8 and r = 0.4, which support a normal-to-plane mode at θ = 30°– 60° (Figure 3.4.1) at 0 mmHg. Based on the finite-element method (FEM) analysis, the thickness of the membrane was optimized to provide a displacement range of 0 – 160 um and a radial strain range of ε_r = 0 – 0.06, which allows $f_{unpolarized}$ satisfy Equation 3.4.1 throughout the pressure (p) range of 0 – 80 mmHg (Figure 3.5.3) and therefore safe operation in the normal-to-plane sensing mode.

Figure 3.5.1c shows the polynomial-fitted experimental reflection spectra (solid lines) and peak locations (markers) obtained from the plasmonic RI gradient sensor operating in the normal-to-plane sensing mode within p = 0 – 80 mmHg at θ = 30°– 60°. In Figure 3.5.1d, the experimental peak locations obtained from Figure 3.5.1c show good agreement with the simulation results (solid lines). Compared to the non-RI gradient sensor (green shaded area), the plasmonic RI gradient sensor (red shaded area) shows a 7.5-12.5x smaller range of $|\Delta\lambda|$ over $30° \leq \theta \leq 60°$. This results in a 4 -14x improvement in R of the plasmonic RI gradient sensor from the non-RI gradient sensor within p = 20 – 80 mmHg (Figure 3.5.1e). R(p) was calculated based on the following equation by replacing the terms involving ε with the corresponding terms expressed in p. In Equation 3.5.2, p_m is the measured pressure, p is the applied pressure, $|d\lambda/dp|$ is the slope of a $p - \Delta\lambda$ curve.

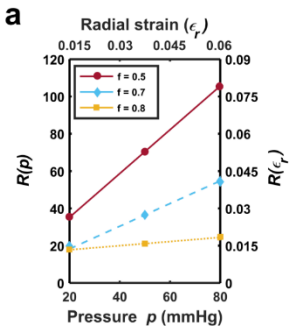

Figure 3.5.2 Relationship between resolution and f. (a) $R(p)$ and $R(\varepsilon_r)$ plotted as a function of p or ε_r for $f = 0.5$ (red solid line), $f = 0.7$ (blue dashed line), $f = 0.8$ (yellow dashed line). A larger f results in smaller ranges of $|\Delta\lambda|$ and $|d\lambda/d\varepsilon|$ and therefore a smaller R as discussed in Chapter 3.4.

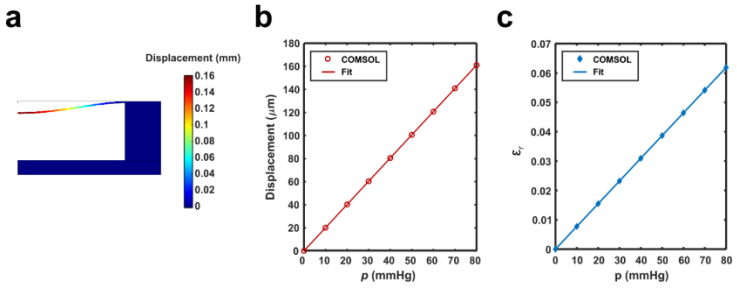

Figure 3.5.3 FEM simulation of PDMS membrane deflection. (a) Simulated displacement of a 11-μm thick, 1.5-mm diameter circular PDMS membrane at 80 mmHg using COMSOL. Calculated (b) displacement – ε_r and (c) p – ε_r curves for a 11-μm thick, 1.5-mm diameter circular PDMS membrane using COMSOL.

$$R(p) = \sigma(p_{\mathrm{m}} - p) = \sqrt{\frac{1}{N}\sum_{k=1}^{N}|p_m(k) - p|^2} = \sqrt{\frac{1}{N}\sum_{k=1}^{N}\left|\frac{\Delta\lambda}{\left|\frac{d\lambda}{dp}\right|_k} - p\right|^2}$$

Equation 3.5.2

$R(p)$ shown in Figure 3.5.1e and Figure 3.5.2 were calculated for N=3, which results in the following Equation 3.5.3.

$$R(p) \cong \frac{1}{\sqrt{3}} \sqrt{\left| \frac{\frac{1}{2} \times \left(\Delta\lambda(\theta_{min}) + \Delta\lambda(\theta_{max}) \right)}{\left| \frac{d\lambda}{dp} \right|_{\theta_{min}}} - p \right|^2 + \left| \frac{\frac{1}{2} \times \left(\Delta\lambda(\theta_{min}) + \Delta\lambda(\theta_{max}) \right)}{\left| \frac{d\lambda}{dp} \right|_{\theta_{max}}} - p \right|^2}$$

$$(N = 3)$$

Equation 3.5.3

The greatest improvement of 14x was achieved when the plasmonic RI gradient sensor showed R = 3 mmHg at p = 20 mmHg for θ = 30°– 45°. R can be further improved by achieving smaller |Δλ| ranges closer to 0 nm over a wider angle of incidence by developing a more optimized fabrication process that creates an ideal plasmonic RI gradient profile and using a high-resolution spectrometer.

3.6 Conclusion

In Chapter 3, the principle of the plasmonic RI gradient on a periodic array was proposed and shown to enable the angle-and-polarization independent 'normal-to-plane' SP mode. The principle and geometry of the plasmonic RI gradient were inspired by the subwavelength protuberances found on the corneas of moths and butterflies. An optimized plasmonic RI gradient allows the normal-to-plane mode whose dipole moment is aligned perpendicular to the plane of periodicity independently of the incident angle and polarization of light. We assessed the angle-independent performance of the plasmonic RI gradient array under in-plane deformation by applying strains along two in-plane perpendicular axes and provided design criteria for the best performance within a targeted range of strain. Based on the criteria, we optimized the plasmonic RI gradient array and embedded it in a hermetically sealed PDMS cavity to enable an angle-independent pressure sensing. As a result, greater than an order of magnitude superior resolution than that of the non-RI gradient array (plasmonic RI gradient R = 3 mmHg, non-RI gradient R = 45 mmHg) was achieved at p = 20 mmHg over θ = 30°– 45°. Pressure sensing performance of such device can be further improved by embedding the array in a mechanical system that exhibits a uniaxial strain or optimization of fabrication processes to create a close to ideal curvature of Au nanoparticles. The proposed principle is not limited to the particular structure studied in this work but can also be applied to many plasmonic systems with diverse geometries working at different wavelengths. With its solid angle-

and-polarization independent performance, we expect that the plasmonic RI gradient approach in optical applications that require high resolution under optical alignment-free operation, such as medical implants, wearables, and free-space optical communication, will proliferate.

3.7 Methods and materials

3.7.1 Sample fabrication

A silicon wafer was rinsed with acetone and isopropyl alcohol (IPA), consecutively. Then a layer of 1-μm thick photoresist (SU 8 2000.5, Microchemicals, Inc.) was spin-coated and baked on a hot plate at 110 ℃ for 120 s. After the wafer was diced into 2 cm x 2 cm chips, acetone edge-biding was performed. Then a 300-nm thick layer of Ni was evaporated using the electron beam evaporator (Mark 40, CHA Industries, Inc.). A 2-um thick PMMA (950PMMA A11, Microchemicals Inc.) was spin-coated on top of the Ni layer and soft-baked on a hot plate at 180 ℃ for 120 s. Then EBL (EBPG 5000+, Raith Inc.) was performed using a 10-nA beam to provide a dose of 1450 $uCcm^{-2}$. The pattern was developed in the methyl isobutyl ketone (MIBK):IPA = 1:1 solution for 60 s and 2-nm thick Cr and 100-nm thick Au were evaporated. Lift-off was performed for 24 hrs in the remover PG bath at room temperature. FIB (Nova 600, Fischer Scientific Inc.) was performed on to the pattern using a 0.5-nA beam for 0.1-ms dwell time to form a parabolic shape. For integration into silicone membranes, the plasmonic RI gradient was coated with a monolayer of Mecapropyl-silane (MPTMS) (Fischer scientific Inc.) in a vacuum chamber for 24 hrs at room temperature. The sample was rinsed with methanol for 30 min – 1 hr to remove excess MPTMS on the Au surfaces. A 10:1 mixture of Sylgard 184 (Dow corning Inc.) was casted onto the pattern, degassed for 30 min, and spin-coated at 7000 rpm, which resulted in a 12-um thick membrane. The sides of the chip were cut to expose the photoresist and Ni layers, which were removed in the acetone and HCl baths [50], respectively. Then the plasmonic RI gradient membrane was assembled with a ring-shaped bottom part made of Sylgard 184 using the uncured PDMS as a curing agent [51]. The assembled cavity was cured for 72 hrs at room temperature. The non-index-gradient (disk) arrays were fabricated using the bi-layer EBL process on the cleaned Si wafer following the same protocol. A 200-nm thick PMMA (495PMMA A4, Microchemicals Inc.) was spin-coated and soft-baked at 180 ℃ for 60 s. Then a 50-nm thick PMMA (950PMMA A2, Microchemicals Inc.) was spin-coated on top of the first layer

and soft-baked at 180 °C for 60 s. EBL was performed using a 300-pA beam to provide a dose of 650 uCcm^{-2}. The pattern was developed in the MIBK:IPA = 1:1 solution for 60 s and 2-nm thick Cr and 100-nm thick Au were evaporated. Lift-off was performed for 24 hrs in the remover PG bath at room temperature.

3.7.2 Computational analysis

A commercial software (FDTD Solutions, Lumerical Inc.) was used for all optical FDTD analyses. A uniform mesh size of 1.5-nm was used throughout the structures and optical constants of Au from Johnson and Christy [52] were used. The different geometries were additionally modeled with analytical TMM (Fig. S2) [53]. For strain analyses, a commercial software for FEM (COMSOL Multiphysics, COMSOL Inc.) was used.

3.7.3 Optical measurements

We customized a setup for angle-variable specular reflection measurements by integrating a commercial spectrometer with a 0.4-nm resolution (Flame, Ocean optics Inc.), a broad-band tungsten light source (SLS201L, Thorlabs Inc.), a 0.014-NA objective (2X Plan Apo Infinity Corrected Long WD, Mitutoyo), and two rotation stages for the sample (CR1, Thorlabs Inc.) and fiber-optic cable of the spectrometer (7R170E-190, Standa Ltd.). The objective aperture size was controlled using an iris (SM05D5, Thorlabs Inc.) to enable a 0.5° resolution. The 500-um diameter focal spot of the incident light was formed onto the 1 mm x 1 mm active area of the sample and the specular reflection was measured while the incident angle varied from 0°, 25° to 60°. The polycarbonate custom-built pressure chamber had a 12.7 mm x 12.7 mm soda lime glass window for optical measurements and was connected to a programmable syringe pump (NE-1000-US, New Era Pump Systems, Inc.) and a low-pressure gauge with a 0.05-mmHg resolution (McMaster-Carr).

3.8 Bibliography

[1] S. A. Maier, Plasmonics: Fundamentals and Applications; Springer Science & Business Media, 2007. DOI: 10.1007/0-387-37825-1

[2] K. A. Willets, et al., Annu. Rev. Phys. Chem. 2007, 58, 267-297.

[3] A. Otto, Z. Phys. A: Hadrons Nucl.1968, 216, 398−410.

[4] R. Ritchie et al., Phys. Rev. Lett. 1968, 21, 1530−1533.

[5] T. W. Ebbesen et al., Nature 1998, 391, 667-669.

[6] J. Aizpurua, P. Hanarp, D. S. Sutherland, M. Käll, G. W. Bryant, F. J. García de Abajo, Phys. Rev. Lett. 2003, 90, 4.

[7] N. Verellen, Y. Sonnefraud, H. Sobhani, F. Hao, Nano Lett. 2009.

[8] W. Wang et al., Mat. Today 2018, 21, 303-314.

[9] K. Forberich, G. Dennler, M. C. Scharber, K. Hingerl, T. Fromherz, C. J. Brabec, Thin Solid Films 2008, 516, 7167.

[10] K. S. Han, H. Lee, D. Kim, H. Lee, Sol. Energy Mater. Sol. Cells 2009, 93, 1214.

[11] D. N. Futaba, Y. Hayamizu, K. Hata, Y. Yamamoto, T. Yamada, A. Izadi-Najafabadi, Y. Yomogida, Nat. Nanotechnol. 2011, 6, 296.

[12] J. Prikulis, P. Hanarp, L. Olofsson, D. Sutherland, M. Käll, Nano Lett. 2004, 4, 1003.

[13] L. J. Sherry, R. Jin, C. A. Mirkin, G. C. Schatz, R. P. Van Duyne, Nano Lett. 2006, 6, 2060.

[14] J. O. Lee, O. Chen, D. Sretavan, J. Du, A. Balakrishna, H. Choo, H. Park, Microsystems Nanoeng. 2017, 3, 17057.

[15] S. J. Han, H. Park, J. O. Lee, H. Choo, J. Biomed. Opt. 2018, 23, DOI 10.1117/1.JBO.23.4.047002.

[16] V. Narasimhan, R. H. Siddique, J. O. Lee, S. Kumar, B. Ndjamen, J. Du, N. Hong, D. Sretavan, H. Choo, Nat. Nanotechnol. 2018, 13, 512.

[17] J. R. Mejía-Salazar, N.O. Osvaldo, Chem. Rev. 2018, 118, 10617-10625.

[18] J. D. Joannopoulos et al., Photonic crystals. Princeton University Press, 2001.

[19] V. G. Kravets, A. V. Kabashin, W. L. Barnes, A. N. Grigorenko, Chem. Rev. 2018, 118, 5912.

[20] J. Homola, S. S. Yee, G. Gauglitz, Sensors Actuators B. Chem. 1999, 54, 3.

[21] K. Matsubara, S. Kawata, S. Minami, Appl. Opt. 1988, 27, 1160.

[22] W. Zhou, T. W. Odom, Nat. Nanotechnol. 2011, 6, 423.

[23] T. V. Teperik, F. J. García De Abajo, A. G. Borisov, M. Abdelsalam, P. N. Bartlett, Y. Sugawara, J. J. Baumberg, Nat. Photonics 2008, 2, 299.

[24] N. Liu, M. Mesch, T. Weiss, M. Hentschel, H. Giessen, Nano Lett. 2010, 10, 2342.

[25] C. D. Chen, S. F. Cheng, L. K. Chau, C. R. C. Wang, Biosens. Bioelectron. 2007, 22, 926.

[26] C.-W. Cheng, M. N. Abbas, C.-W. Chiu, K.-T. Lai, M.-H. Shih, Y.-C. Chang, Opt. Express 2012, 20, 10376.

[27] X. Zhu, S. Xiao, L. Shi, X. Liu, J. Zi, O. Hansen, N. A. Mortensen, Opt. Express 2012, 20, 5237.

[28] K. Aydin, V. E. Ferry, R. M. Briggs, H. A. Atwater, Nat. Commun. 2011, 2, 517.

[29] L. Li, Y. Yang, C. Liang, J. Appl. Phys. 2011, 110, 1.

[30] C. Goßler, C. Bierbrauer, R. Moser, M. Kunzer, K. Holc, W. Pletschen, K. Köhler, J. Wagner, M. Schwaerzle, P. Ruther, O. Paul, J. Neef, D. Keppeler, G. Hoch, T. Moser, U. T. Schwarz, J. Phys. D. Appl. Phys. 2014, 47, DOI 10.1088/0022-3727/47/20/205401.

[31] M. Choi, J. W. Choi, S. Kim, S. Nizamoglu, S. K. Hahn, S. H. Yun, Nat. Photonics 2013, 7, 987.

[32] M. Wolf, D. Haensse, M. Rothmaier, S. Spichtig, B. Selm, Opt. Express 2008, 16, 12973.

[33] J. Guo, M. Niu, C. Yang, Optica 2017, 4, 1285.

[34] H. H. Chou, A. Nguyen, A. Chortos, J. W. F. To, C. Lu, J. Mei, T. Kurosawa, W. G. Bae, J. B. H. Tok, Z. Bao, Nat. Commun. 2015, 6, 1.

[35] W. H. Bernhard, C. G; Miller, Acta Physiol. Scand. 1962, 56, 385.

[36] J. L. Miller, W. H.;Bernard, G. D.;Allen, Science 1968, 162, 760.

[37] D. G. Stavenga, S. Foletti, G. Palasantzas, K. Arikawa, Proc. R. Soc. B Biol. Sci. 2006, 273, 661.

[38] P. B. Clapham, M. C. Hutley, Nature 1973, 244, 47.

[39] K. Forberich, G. Dennler, M. C. Scharber, K. Hingerl, T. Fromherz, C. J. Brabec, Thin Solid Films 2008, 516, 7167.

[40] K. S. Han, H. Lee, D. Kim, H. Lee, Sol. Energy Mater. Sol. Cells 2009, 93, 1214.

[41] D. N. Futaba, Y. Hayamizu, K. Hata, Y. Yamamoto, T. Yamada, A. Izadi-Najafabadi, Y. Yomogida, Nat. Nanotechnol. 2011, 6, 296.

[42] Y. M. Song, Y. Xie, V. Malyarchuk, J. Xiao, I. Jung, K. J. Choi, Z. Liu, H. Park, C. Lu, R. H. Kim, R. Li, K. B. Crozier, Y. Huang, J. A. Rogers, Nature 2013, 497, 95.

[43] R. H. Siddique, S. Vignolini, C. Bartels, I. Wacker, H. Hölscher, Sci. Rep. 2016, 6, 1.

[44] C. G. Bernhard, G. Gemne, J. Sällström, Z. Vgl. Physiol. 1970, 67, 1.

[45] J. A. Fan, K. Bao, C. Wu, J. Bao, R. Bardhan, N. J. Halas, V. N. Manoharan, G. Shvets, P. Nordlander, F. Capasso, Nano Lett. 2010, 10, 4680.

[46] M. Hentschel, M. Saliba, R. Vogelgesang, H. Giessen, A. P. Alivisatos, N. Liu, Nano Lett. 2010, 10, 2721.

[47] B. Luk'Yanchuk, N. I. Zheludev, S. A. Maier, N. J. Halas, P. Nordlander, H. Giessen, C. T. Chong, Nat. Mater. 2010, 9, 707.

[48] J. Zuloaga, P. Nordlander, Nano Lett. 2011, 11, 1280.

[49] D. Wang, M. R. Bourgeois, W. K. Lee, R. Li, D. Trivedi, M. P. Knudson, W. Wang, G. C. Schatz, T. W. Odom, Nano Lett. 2018, 18, 4549.

[50] X. Wen, G. Li, J. Zhang, Q. Zhang, B. Peng, L. M. Wong, S. Wang, Q. Xiong, Nanoscale 2014, 6, 132.

[51] B. Samel, M. K. Chowdhury, G. Stemme, J. Micromech. Microeng. 2007, 17, 1710.

[52] P. B. Johnson, R. W. Christy, Phys. Rev. B 1972, 6, 4370.

[53] R. H. Siddique, G. Gomard, H. Hölscher, Nat. Commun. 2015, 6, 1.